UNIVERSIDAD POLITÉCNICA DE MADRID

ESCUELA TÉCNICA SUPERIOR DE INGENIEROS
DE TELECOMUNICACIÓN

SHORT PULSE GENERATION FROM SEMICONDUCTOR LASERS: CHARACTERIZATION, MODELING AND APPLICATIONS

Tesis Doctoral

ANTONIO CONSOLI BARONE

Ingeniero en Electrónica

Madrid 2011

DEPARTAMENTO DE TECNOLOGÍA FOTÓNICA

ESCUELA TÉCNICA SUPERIOR DE INGENIEROS DE TELECOMUNICACIÓN

Short pulse generation from semiconductor lasers: characterization, modeling and applications

Autor

Antonio Consoli Barone

Ingeniero en Electrónica

Director

Ignacio Esquivias Moscardó

Doctor Ingeniero de Telecomunicación

Co-Director

Francisco José López-Hernández

Doctor Ingeniero de Telecomunicación

Madrid 2011

Tribunal

Nombrado por el Mgfco. y Excmo. Sr. Rector de la Universidad Politécnica de Madrid

Presidente

.....

Vocales

.....

.....

.....

Secretario

.....

Realizado el acto de defensa y lectura de la Tesis el día ..... de .....

de 2011, acuerda otorgar la calificación de .....

Resumen

Esta Tesis describe el trabajo de investigación realizado sobre pulsos ópticos generados por láseres de semiconductor con duración de decenas de picosegundos. El trabajo se ha enfocado sobre diodos láser de cavidad vertical a 1550 nm, transmisores ópticos muy prometedores por sus ventajosas características en el entorno de las comunicaciones ópticas en fibra con modulación directa. El elevado ancho de banda previsto para las futuras redes ópticas requiere el conocimiento detallado de las propiedades eléctricas de los transmisores, así como de las propiedades de los pulsos generados por éstos que transportan la información binaria. En la presente Tesis, se describen los diferentes logros alcanzados en la caracterización de dicho tipo de láseres y de los pulsos generados por ellos, así como sus aplicaciones en un entorno de comunicaciones ópticas. Se han caracterizado láseres de cavidad vertical con emisión a 1550 nm, basados en pozos cuánticos y unión túnel, a través de medidas estáticas y dinámicas de la impedancia eléctrica y de la respuesta en modulación entre 0 y 10 GHz. Se han modelado los parásitos eléctricos y el circuito eléctrico equivalente de la estructura del dispositivo teniendo en cuanta los efectos de captura y escape de los portadores en los pozos cuánticos. Se han calculado los parámetros intrínsecos de los dispositivos a partir de las medidas realizadas. Se han empleado los dispositivos así caracterizados para la generación de pulsos con duraciones tan pequeñas como 55 ps a diferentes frecuencias de repetición, utilizando la técnica de conmutación de ganancia. Se ha medido la duración, la amplitud del pico, el "jitter" y el ancho espectral de los pulsos en función de los parámetros de conmutación de ganancia. Se ha investigado el efecto de la inyección óptica sobre los pulsos generados con dichos láseres de cavidad vertical conmutados en ganancia, obteniéndose una reducción del "jitter" en un amplio rango de los parámetros de inyección. Se ha diseñado e implementado un codificador de acceso múltiple por división de códigos ópticos (OCDMA) basado en líneas ópticas de retardo que emplea los pulsos generados por los dispositivos conmutados en ganancia. Finalmente, se ha propuesto y demostrado una novedosa implementación de la técnica de reconstrucción de fase por medio de la diferenciación óptica ultra rápida (PROUD), para la caracterización en

amplitud y fase de pulsos ópticos. El diferenciador óptico necesario para la técnica ha sido realizado con un interferómetro birrefringente basado en fibra mantenedora de la polarización. Se ha medido la variación instantánea de la frecuencia ("time resolved chirp") de pulsos de diferente duración y forma, obtenidos con un laser conmutado en ganancia, y el factor de ensanchamiento de linea del laser utilizaso.

Abstract

This Thesis describes the research work that has been carried out on the generation of optical pulses, with duration of tens of picoseconds, from semiconductor lasers. The work is focused on 1550 nm Vertical Cavity Surface Emitting Lasers (VCSEL), which are promising optical transmitters due to their advantageous characteristics in the context of fiber optical communications with directly modulated sources. The high bandwidth expected for future optical networks requires the accurate knowledge of the transmitter electrical properties and of the laser generated optical pulses which carry the binary information. This Thesis describes the various achievements obtained in the characterization of these devices and the generated pulses, as well as their applications to an optical communications environment. VCSELs emitting at 1550 nm, based on quantum wells and tunnel junction, have been characterized by static and dynamic impedance measurements and modulation response between 0 and 10 GHz. The electrical parasitics and the equivalent circuit of the device have been modeled, taking into account the effects of capture and escape of carriers in quantum wells, and the laser intrinsic parameters have been calculated from the measurements. The VCSELs have been used for pulse generation using the gain switching technique, obtaining the shortest duration of 55 ps at different repetition frequencies. The duration, peak amplitude, jitter and spectral width of the pulses have been measured as a function of the gain switching conditions. The effect of optical injection on the pulses generated by gain switched VCSELs has been investigated, obtaining a jitter reduction over a wide range of injection parameters. An Optical Code Division Multiple Access (OCDMA) encoder based on optical delay lines has been designed and implemented, using the optical pulses generated by the gain switched devices. Finally, a novel implementation of the Phase Reconstruction using Optical Ultrafast Differentiation (PROUD) technique has been proposed and demonstrated for optical pulse characterization in amplitude and phase. The optical differentiator required in the PROUD technique has been realized with an interferometer based on birefringent polarization maintaining fiber. The instantaneous frequency, i.e. the time resolved chirp, of pulses with different durations and

shapes obtained from a gain-switched laser, and the laser linewidth enhancement factor have been measured.

Contents

Chapter 1

Introduction

The development of semiconductor lasers, optical fibers and receivers in the last three decades has increased the speed and capacity of fiber based telecommunication systems all over the world and great research effort has been dedicated to the improvement of optical communication techniques towards the next generation optical networks. The semiconductor laser plays a crucial role in this scenario, as the modulation speed of the whole channel is limited by the modulation speed of the light transmitter. Externally modulated sources, where the laser is always on and a fast shutter modulates the laser output with the information bit sequences, allow to reach high modulation speeds over long distances, paying the price of employing the external modulator as an additional optical component. Directly modulated light sources, where the diode laser is directly driven by an electrical signal, are the preferred choice with respect to externally modulated lasers in medium and short distances communication channels, due to the direct integration on electrical circuits and the reduced costs. Thus, academic and industrial research groups have focused their attention on the development of semiconductor lasers with high frequency modulation response and optical output characteristics optimized for the fiber optic channel.

The advent of Distributed Feedback (DFB) lasers and Multi Quantum Well (MQW) active regions represented a big step towards better performances, as these devices offer single longitudinal mode emission and higher modulation speed with respect to the Fabry Perot bulk volume diode lasers. A strong competitor to MQW's DFB lasers, specially in short distance applications, is the Vertical Cavity Surface Emitting Laser (VCSEL), due to its intrinsic single mode operation, very high modulation speeds recently reported, low threshold and low power consumption together with wafer level testability and consequently reduced manufacturing cost.

High speed diode lasers are interesting light sources for optical pulse genera-

tion with duration of picoseconds and less, which find applications in many different fields, such as fundamental physics research [Gibb 96], material processing [Momm 96], optical ranging [Besl 88] and biomedical instrumentation [Ster 89]. The namely most used techniques for laser pulse generation are mode locking, Q switching and gain switching [Vasi 00]. The advantage of a gain switched (GS) laser, with respect to the other two techniques, is its simple implementation and the flexibility of pulse duration and repetition rates that can be obtained. In GS semiconductor lasers, only an external DC and AC electrical sources are needed, as the pulse generation is obtained with direct electrical modulation, by proper choice of the modulation parameters. On the other hand, GS lasers generate highly *chirped* pulses, as the instantaneous frequency of the pulse is affected by strong temporal variations due to the intrinsic nature of a GS laser diode. This phenomenon is specially relevant in communications environment, where an accurate characterization of the pulse chirp is often required in order to properly model the pulse propagation in fiber. More generally, the knowledge of the instantaneous frequency of an optical pulse is an interesting and attractive field of research, as it is often required for a more accurate insight on the optical signal.

GS VCSELs emitting around 850 nm have been investigated extensively by many research groups. Anyway, Long Wavelength (LW) VCSELs, operating around 1310 nm and 1550 nm, have been produced only in recent years, due the technological challenge imposed by the fabrication of reliable and efficient devices, and consequently, the analysis and the exploitation of LW VCSEL characteristics have raised a growing interest in the research community only in recent times.

The work of this Thesis is organized as follows:

- In Chapter 2, the VCSEL structure and properties are described. An overview of the VCSEL evolution and progress is given, presenting the technical characteristics of the device, as the short cavity length and vertical structure. Attention is given to the VCSEL structures for optical and current confinement, the high reflectivity mirrors for low threshold current operation, and the recent introduction of the Tunnel Junction (TJ), which allowed the realization of efficient LW VCSELs. The peculiar characteristics of VCSEL with respect to edge emitting lasers, such as multi transversal mode operation and orthogonal polarization mode emission are described. Finally, a comparison with EE laser is given.

- In Chapter 3, the dynamic behavior of semiconductor lasers is reviewed and carriers/photons interactions are described using a simple model based on particle rate equations. The steady state solution and small signal analysis

are presented. The electrical properties of a laser diode are introduced, in static and dynamic regime, with the analysis of the impedance below and above threshold. A simple model, based on carrier capture and escape, for MQW's device is illustrated. Gain switching and optical injection techniques are presented.

- In Chapter 4, the work performed on the electrical characterization of a LW VCSEL based on TJ [Cons 11a] is presented. Static and frequency dependent measurements of the device impedance are presented and discussed. The dynamic model presented in Chapter 3 is used for the interpretation of the results and fitting to model equations for parameters extraction. Modulation response measurements are presented and electrical parasitics removal with a transfer matrix approach is illustrated. The Chapter ends with a complete list of the device parameters obtained from fitting measurements to our model.

- In Chapter 5, the generation of short optical pulses from a GS 1550 nm VCSEL [Cons 10a, Cons 08] is reported. The pulse properties, i e. peak amplitude, duration, jitter and spectral width, are investigated as a function of the gain switching conditions. Single pulse per period and multiple peaked pulses are observed and the modulation parameters are optimized for the shortest pulse generation at the highest frequency.

- In Chapter 6, the experimental results obtained with an optically injected GS 1550 nm VCSEL are presented [Cons 09c, Cons 09b, Cons 10b]. The timing jitter and the pulse duration of the optical pulse train at the VCSEL output have been characterized as a function of the frequency detuning between the injection and injected lasers. Jitter reduction and pulse temporal broadening are observed in the frequency locking region. Experimental results are compared with theoretical prediction, showing good agreement.

- In Chapter 7, an OCDMA encoder based on a GS 1550 nm VCSEL [Cons 09a] is presented. A driving circuit has been designed for the generation of an optical pulse train with short pulse duration and very low duty cycle, using the GS VCSEL as optical source. Optical delay lines are used to generate the optical code for a single user. The proposed system is an efficient and simple solution for application in low bit rate channel with multiple users.

- In Chapter 8, a novel implementation of the *Phase Reconstruction using Ultrafast Optical Differentiation* (PROUD) method [Cons 11b, Cons 11c] is presented. PROUD measures the instantaneous frequency of an optical signal

and we have implemented it in a novel configuration, which presents several advantages with respect to previously reported realizations. The validity of the results obtained with a GS DFB laser is demonstrated by comparison with the independently measured pulse spectra.

- In Chapter **??**, the main conclusions of this Thesis are summarized and the possible directions for future work are drawn.

Chapter 2

Vertical Cavity Surface Emitting Lasers

In this Chapter, Vertical Cavity Surface Emitting Lasers (VCSELs) are introduced. VCSELs are complex devices with very different characteristics from edge emitting (EE) lasers. Single longitudinal mode operation, low threshold current and circular beam profile together with wafer level testability and cost-effective array fabrication are some of the advantage of VCSELs over EE devices. On the other hand, transverse mode propagation, lower power output and heat dissipation among others are some VCSELs' disadvantages that demands for further research effort. In this Chapter, VCSELs structure and performances are described and compared to EE devices.

2.1 VCSEL structure

2.1.1 Early VCSELs

The first operation of a vertical cavity laser was reported in 1965 by Melngailis [Meln 65]: the device had an indium antimonide (InSb) active region and emitted at 5.2 µm with pulsed operation at 10 K. Near infrared wavelengths, interesting for fiber based optical communication channels, were available after the work of Iga and colleagues in the late 1970s [Soda 79].

The VCSEL basic structure is depicted in Fig. 2.1, where the active region is stacked between the bottom and top mirrors. Light propagates in the vertical direction, orthogonally to the active region plane and the current is injected from the mirrors. The vertical epitaxial growth of the structure allows micro cavity dimensions, with typical effective cavity lengths of some micrometers, two orders of magnitude smaller than typical EE lasers [Agra 02].

The short cavity length of VCSELs corresponds to a large spacing between adjacent longitudinal modes of the resonator, thus only one longitudinal mode is within the optical gain spectrum of the active medium and VCSELs are consequently single mode lasers.

The reduced thickness of the active region however limits the gain experienced by photons traveling in the cavity and mirrors with high reflectivities are needed to satisfy the threshold condition. The first VCSELs were made with metallic mirrors (Au coated mirror and Au/Zn mirror, electrode) [Mote 82, Soda 83], with limited reflectivity (about 95%), resulting in a threshold current of 160 mA under pulsed operation at 77 K.

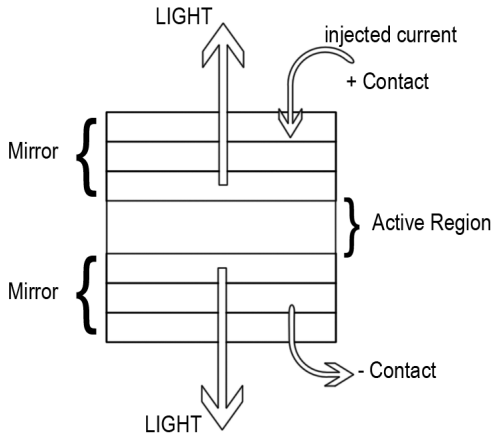

Figure 2.1: Schematic structure of a VCSEL.

Continuous wave (CW) operation at room temperature [Lee 89] was demonstrated for the first time in 1989 thanks to the introduction of a Quantum Well (QW) based active region and the use of Distributed Bragg Reflector (DBR) mirrors, with reflectivities of 99.87 % and 99.96 %, instead of the metallic mirrors previously employed.

The device fabricated by Lee et al. had a threshold current of 1.5 mA under CW operation and emitted at 980 nm. The low value of the threshold current with respect to EE lasers is due to the increased current density in the small active region, values in the mA and sub-mA ranges are typical in VCSELs [Geel 90, Sun 03].

2.1.2 Long wavelength VCSELs

The importance of high reflectivity mirrors in the wavelength region of emission is relevant for producing VCSELs in the second and third window of optical fiber communications. In short wavelength VCSELs, with emission around 850 nm, the DBR mirrors are made of AlAs and AlGaAs layers and, due to the relatively high difference between the refractive indexes of the two materials, only 12-15 pairs of GaAs/AlAs layers are required for achieving a reflectivity higher than 99 %.

Laser active materials for the emission in the 1.1 µm to 1.6 µm are usually based on the quaternary alloy InGaAsP grown on a InP substrate, DBR mirrors based on the pair InP - InGaAsP have small difference in the refractive index of the two materials and more than 40 pairs must be grown for high reflectivity (>99%).

The fabrication of DBR mirrors with more than 40 layers is a challenging task and p-doped InP based DBR mirrors introduce a high series resistance and optical losses. In consequence the fabrication of CW operating VCSELs at long wavelengths has taken more than one decade from the first VCSELs reported by Iga and colleagues.

In 1999 Boucart et al. reported the room temperature CW emission of a 1.55 µm VCSEL [Bouc 99]. The top DBR consisted of 26.5 n-doped GaAs-AlAs pairs which were grown directly on an n-InP substrate (metamorphic mirrors). The bottom mirror consisted of 50 pairs of n-doped InGaAsP-InP layers having a reflectivity of 99.7%.

2.1.3 The Tunnel Junction

The work of Boucart [Bouc 99] introduced an important novelty in the fabrication of LW VCSELs: the insertion of a tunnel junction (TJ) between the active region and one of the two mirrors. The TJ was firstly discovered by Leo Esaki in 1974 [Esak 74] and it consists of a highly doped p-n junction with a peculiar current-

voltage characteristic in which a negative resistance is observed in part of the forward bias curve.

In LW VCSEL the TJ is reverse biased and brings two considerable advantages: it allows the fabrication of two n-doped DBR mirrors and provides good current confinement. Mirrors with n-doping show less absorption and reduced resistivity with respect to p-doped mirrors, resulting in improved mirror efficiency and better thermal behavior.

2.1.4 Optical and electrical confinement

In both short and long wavelength devices, the circular shape and the vertical structure of VCSELs, which allow wafer level testability and efficient coupling to optical fiber, produce quite different characteristics of emission than EE lasers.

Due to the non-uniform current distribution inside the active region, multiple transverse modes can be excited apart from the fundamental one and the rotational 4-fold symmetry of VCSEL structure (both square and circular) causes the existence of different polarization modes [Chan 91]. Multi-transverse mode behavior is employed in high power devices [Grab 98] and polarization instability have found recent application in optical signal processing [Kawa 06].

Single transverse mode operation and stable polarization emission are obtained by efficient current and optical confinement. Gain guiding and index guiding structures have been proposed to this purpose. In Fig. 2.2 (left) a gain-guided structure is shown: a ion-implanted region in the top DBR mirror is defined selectively to control the flow of injected current into the active layer [Yu 03].

Index guided VCSELs commonly have better transverse optical confinement than

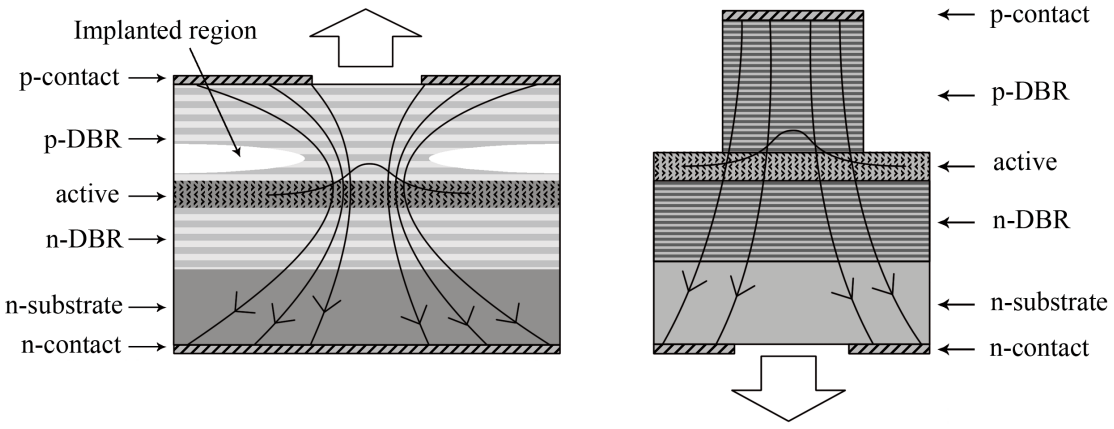

Figure 2.2: Gain-guided, top emitting VCSEL with ion implantation (left) and index guided, air posted bottom emitting VCSEL (right). Adapted from [Yu 03].

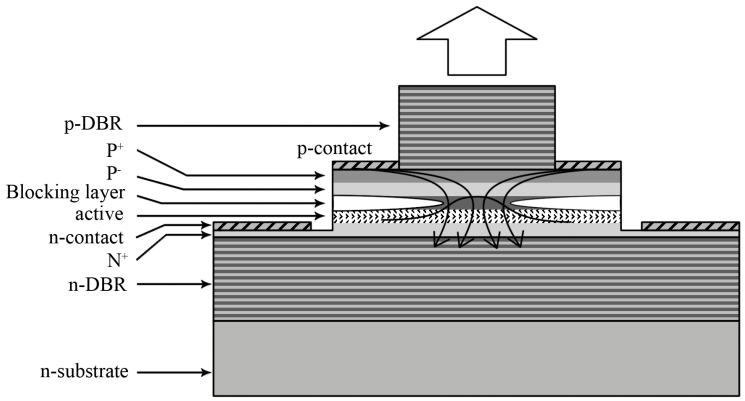

Figure 2.3: VCSEL structure with intracavity contacts, adapted from [Scot 94].

gain guided devices. Several types of index guided VCSELs can be found in literature such as air-posted, etched mesa, regrowth buried hetero-structure with different fabrication procedure complexity. Figure 2.2 (right) shows the air posted index guided structure [Yu 03]. The large difference in refractive index between the semiconductor and the air provides strong transverse confinement of the optical field. However, single transverse mode operation is not stable in VCSELs with oxide confinement, especially at high injection level.

An intracavity structure can be introduced to avoid the current flow through the top mirror and avoid the heating from the mirrors. Scott and co workers [Scot 94] proposed an intracavity structure where additional layers are inserted between the p and n DBRs on either surface of the active region to provide an electrical path to the current to reach the active region, see Fig. 2.3. A current constriction is also realized on the top of the active region to force the current to flow in the optical mode. This current constriction can be made with ion implantation or oxidation, for example. Current crowding may occur near the periphery of the device where the optical mode is weak so that the influence of spatial hole burning of carrier concentration can be enhanced. A resistive layer between the conductive layer on the top of the forcing current layer and the active region can be introduced, such as a buried TJ, to minimize the influence of current crowding.

2.2 VCSEL characteristics

2.2.1 Power-Current-Voltage curve

The small size of the active volume and the high reflectivity of the DBRs mirrors in VCSELs gives rise to a low value of the threshold current. Typical values of

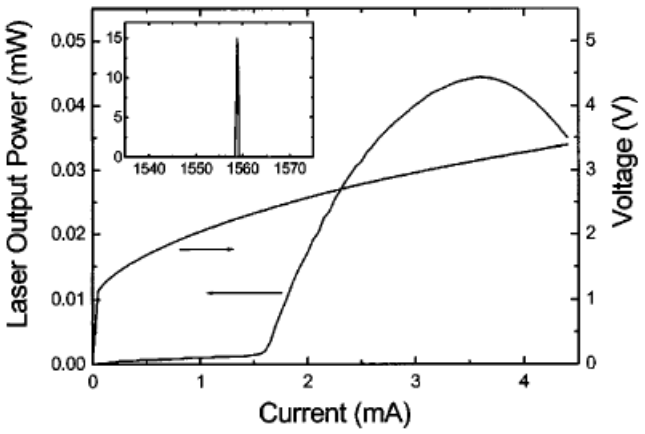

Figure 2.4: Power-Current-Voltage curve for a 1560 nm emitting VCSEL. The inset shows the spectrum just above threshold [Shin 02].

the threshold current are of few milliamperes and devices with sub-milliamperes threshold current have been reported [Sun 03]. In Fig. 2.4 the Power-Current-Voltage (P-I-V) curve of a 1560 nm emitting VCSEL is shown [Shin 02].

The device is an oxide aperture VCSEL. From the inset in Fig. 2.4, the single longitudinal and transverse mode operation is observed. The threshold current is 1.6 mA and the maximum output power is 450 µW. The decrease in output power at higher injection current is due to the current heating of the device. The current flow generates heat through the Joule effect. As temperature increases, gain red-shifts and decreases too, so that losses are increased and the emitted power is reduced (thermal roll over). From the plot of voltage versus current, a value of 285 Ohm is deduced for the series resistance of the device above threshold. The main contribution to the high value of series resistance is attributed to the mirror resistivity, typically high in DBRs.

2.2.2 Thermal behavior

Temperature affects the threshold current (I_{TH}) of VCSELs in a different way with respect to multi longitudinal modes EE lasers. In a semiconductor material with optical gain, as temperature increases, the optical gain peak decreases and red-shifts towards longer wavelengths. In Fabry-Perot (FP) lasers, this means that losses increase and the set of longitudinal modes that compose the emission spectrum also red shifts, with the hopping of the dominant longitudinal mode to the adjacent one, so that the central mode follows the gain peak.

In VCSELs, cavity is short and longitudinal mode spacing is consequently large, so that only one longitudinal mode is contained in the gain spectrum. Dur to their

temperature dependent nature, the cavity resonance and the gain move at different rates so that the cavity mode can match or not the gain maximum, depending on its position. The cavity mode changes with the temperature T, due to the dependence of the refractive index on T and, for a typical value of $^{dn}/_{dT}$ $3{\cdot}10^{-4}$, this yields a change of $^{d\lambda}/_{dT} = 0.15\ ^{nm}/_{K}$. The temperature drift of the gain peak is typically $\approx\ ^{d\lambda}/_{dT} = 0.3\ ^{nm}/_{K}$ and the spectral region of maximum reflection of the DBR mirrors is almost temperature independent, as the relative difference of refractive index between the DBR layers is almost constant with T. As a consequence, there is in VCSEL a minimum value of I_{TH}, as a function of T, corresponding to the matching of the cavity mode with the gain peak. A typical plot of I_{TH} as a function of the temperature is shown in Fig. 2.5 (left), where the laser is operating in CW and T is increased. Threshold current convexes downward and reaches its minimum value at $T_{HS} = 50^{\circ}$ for the device described in [Yue 04].

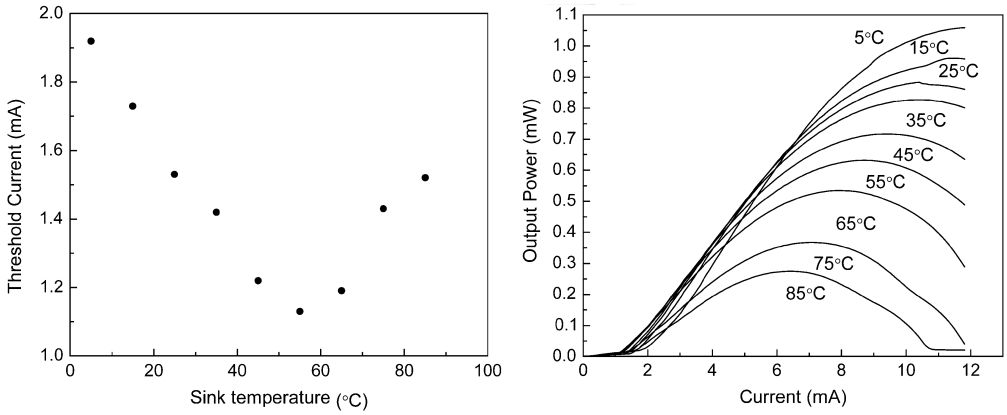

Figure 2.5: Threshold current versus temperature (left) and P-I curves at different temperatures (right) for a 1.3 µm GaAs VCSEL [Yue 04].

Usually VCSELs are designed to have minimum I_{TH} at room temperature. When I_{TH} is minimal, the cavity resonance matches the optical gain peak. For lower and higher value of temperature, cavity resonance sees lower value of the gain and so losses are higher and I_{TH} increases.

The power-current (P-I) curves for different values of the temperature at the heat sink are shown in Fig. 2.5 (right), for the same lasers of [Yue 04]. At higher temperatures the effect of thermal roll over is stronger because of the current heating process.

2.2.3 Transverse linearly polarized modes in VCSELs

In this paragraph, a qualitative discussion about transverse modes in VCSELs is provided. An exact solution of the Maxwell's equations is needed for the calcula-

tion of all allowed transverse optical modes in a cylindrical waveguide, . Higher order transverse modes can be supported in VCSEL with large transverse area size. Furthermore, the influence of injection current, stimulated emission and thermal lensing can modify the gain transverse distribution and refractive index and hence can deteriorate the single mode operation of VCSELs.

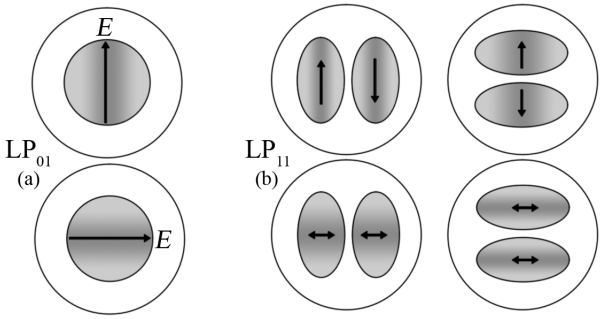

Figure 2.6: Field distribution of the LP_{01} (a) and LP_{11} (b) modes [Yu 03].

Transverse modes in VCSELs can be treated with the cylindrical waveguide theory, very well known in optical fibers. Transverse modes characteristics need a full set of optical modes to be treated, including transverse magnetic (TM), transverse electric (TE) and their hybrid modes (HE and EH modes) obtained form a cylindrical dielectric waveguide. If a weakly guiding cylindrical waveguide is considered, linearly polarization (LP) modes can be proposed to substitute the full set of TM, TE and hybrid modes, which considerably simplifies the study of transverse modes in cylindrical waveguides. From a complete treatment of the propagation of optical waves in a cylindrical waveguide, assuming the weakly guided wave approximation [Agra 02], LP_{mn} modes are obtained, where the index m stands for the azimuth direction and the index n for the radial direction. Figure 2.6 shows the field distribution of LP_{01} and LP_{11} modes [Yu 03]. As it will be shown later, the spectrum of a VCSEL is directly affected from multimode propagation and different polarizations components.

2.2.4 Transverse current profile and Spatial Hole Burning

The transverse distribution of stimulated recombination in the active region depends on the distribution of the optical modes and the current flow: when the photon density is not uniform, the stimulated recombination in those region with high photon density depletes the carrier concentration and therefore the modal gain. This phenomenon is called Spatial Hole Burning (SHB). When operating at high levels of injected current, the competition of high transverse modes versus the fundamental

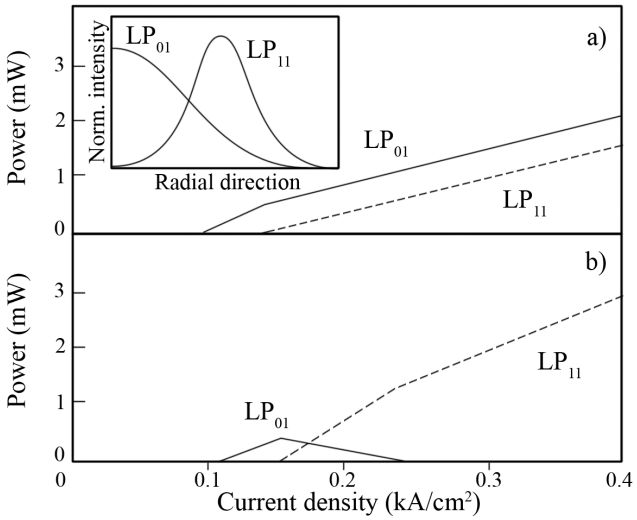

Figure 2.7: Mode competition in VCSEL: P-I curves for different injection current transverse profiles, with circular disk contact (a) and circular ring contact (b) [Vall 95].

mode can be enhanced through SHB. SHB is excited by stimulated recombination of carrier concentration inside the active layer, and the shape of SHB follows the transverse profile of optical intensity. For VCSEL operating at high current injection levels, SHB reduces the modal gain of the fundamental mode and higher transverse modes can be excited. This is due to the reduction of overlap between the transverse distribution of optical gain and transverse mode distribution. The self focusing effect is also observed in VCSELs, due to the refractive index change induced by carrier concentration, so that the beam width of the fundamental mode is reduced and the stability of single mode operation is also reduced.

The distribution of carriers inside the active region is described by the current spreading and current crowding phenomena. Current spreading reduces the slope efficiency and increase the threshold current, so that devices with good electrical confinement are desired. On the other hand, current crowding is the accumulation of carriers along the border of the electrical confinement structure. In ion implanted devices, for example, current crowding occurs along the border of oxide aperture [Stri 00]. The performance of VCSELs can deteriorate due to the excitation of SHB from current crowding as well as the thermal lensing, due to excessive heat sources. Current crowding normally occurs in devices with strong confinement structure and usually leads to the accumulation of carriers in the periphery of the core region. The confinement structure and the geometry of metallic contacts play an important role in the current distribution inside the active layer [Vall 95]. If a weakly guided VCSEL is considered, such as one with gain-guided structure, a different behavior in the

transverse mode competition is expected for devices with circular-ring or circular-disk contact. In Fig. 2.7 is shown the competition of LP_{01} and LP_{11} modes at various bias, adapted from [Vall 95]. It is noted that for weakly guided VCSELs with circular-disk contact, LP_{01} is the dominant mode but for the device with circular-ring contact, LP_{01} can completely be suppressed. Hence, it has been shown that for VCSELs with weakly-guided structure, stable fundamental mode operation can be maintained at high power if the current distribution is concentrated at the center of the active region.

2.3 Comparison with Edge Emitting lasers

The structure and characteristics of VCSELs have been described in the previous paragraphs and the differences with the structure and characteristics of EE lasers have been briefly discussed. In Tab. 2.1, the performances of VCSELs and two types of EE lasers, i.e. Fabry-Perot and Distribute Feedback (DFB) lasers, are directly compared.

The devices described in Tab. 2.1 are a FP laser (Mitsubishi ML9xx45 Series), a DFB laser (Mitsubishi ML9xx11 Series) and a VCSEL (Vertilas VL-1550-10G). Some important differences can be seen from Tab. 2.1. Due to the structure of VCSELs and DFBs, the emission spectra of these two types of laser are inherently single mode with extremely narrow spectral widths. On the other hand, the emission spectrum of FP lasers is composed of multiple longitudinal modes and its spectral linewidth is considerably greater than VCSELs and DFBs.

The transverse beam section for FP and DFB lasers is elliptical due to the rectangular aperture from which light is emitted. As a result, different values for the parallel and perpendicular direction of the beam divergence angle are expected. In VCSELs, the circular aperture produces a circular beam profile, instead of elliptical, with a smaller divergence angle with respect to FPs and DFBs. VCSELs present a smaller value of maximum output power with respect to FPs and DFBs. The difficulty to produce VCSELs for telecommunication applications with high output power comes from the considerations made in the previous paragraphs about modes competition, active area size, current confinement and heat dissipation.

The threshold current and operating electrical power are lower in VCSELs than in FPs and DFBs. This is an advantage when low power operations are needed. The considerations made in this paragraph on the three devices proposed for comparison have to be taken with attention. For example, better performance of data rate for DFB lasers can be found in literature.

In general, it can be said that VCSEL are superior to FP lasers for the single mode emission, beam quality and low power consumption, while they are competitive with DFB lasers for beam quality and power consumption. However VCSELs are also especially promising in terms of modulation speed. Recently, the record speed of direct modulation at 40 Gb/s has been reported in a 1550 nm VCSEL [Hofm 11] and a modulation bandwidth in excess of 60 GHz has been obtained with a injection locking scheme [Zhao 07].

The production cost of VCSELs is competitive with both FPs and DFBs, because of their testability at wafer stage production, even if nowadays are few the manufacturers of VCSELs emitting at 1550 nm. VCSELs can be produced in one-dimensional and two-dimensional arrays on the same chip, allowing for higher output powers and multi-wavelength operation. Tunable VCSELs have also been proposed [Chan 00], through the use of micro mechanical structure (MEMS) to change the

Parameter	Fabry-Perot	DFB	VCSEL
Longitudinal modes	MM	SM	SM
Central wavelength [nm]	1550	1550	1550
Linewidth [nm]	1.5	<0.1	2.4e-4
Side Mode Suppression Ratio [dB]	-	40	40
Beam divergence (horizontal) [deg]	25	25	12
Beam divergence (vertical) [deg]	30	35	12
Max output power [mW]	6	10	4
Slope efficiency [mW/mA]	0.25	0.28	0.2
Threshold current [mA]	10	8	1.5
Operating current [mA]	30	25	10
Operating voltage [V]	1.1	1.1	2
Rise time [ns]	0.3	0.1	0.1
Data rate [Gbps]	0.155	1.25	10

Table 2.1: Comparison between commercially available laser diodes of three types: Fabry-Perot, VCSELs and Distributed Feed Back laser emitting at 1550 nm. See text for details.

emission wavelength.

Chapter 3

Basic dynamic properties of semiconductor lasers

In this Chapter, the static and dynamic characteristics of semiconductor lasers are presented through a simple model based on the rate equations approach. It's first considered the general case of a bulk single mode laser, then the rate equation model is presented for a device with Quantum Well active region. For both kind of lasers, the steady state solutions and small signal analysis for carrier and photon densities are presented. The static and dynamic impedance, below and above threshold, is described for bulk and Quantum Well devices. The large signal modulation is considered, introducing the pulse generation technique of gain-switching. Finally, the optical injection technique is described, by modifying the previously presented rate equations.

3.1 Rate equations in semiconductor lasers

The light-matter interactions occurring in a semiconductor laser can be modeled in a simple way using the well known Rate Equations (RE) approach [Agra 02, Cold 95]. This model gives a clear formulation of the most relevant static and dynamic characteristics of semiconductor lasers.

Charge carriers and optical field are considered for the contribution to population inversion and optical amplification and losses in the laser cavity. The RE model consists of the charge and the optical field conservation equations. The number of electron and holes is assumed to be the same, thus only one equation for electrons is considered in the model. The optical field conservation equation can be represented both with complex numbers, expressing the real and imaginary parts of the field, or via its intensity and phase. In this Chapter, the RE model is presented with the number of photons, thus optical intensity, and the optical phase. Specifically, the carrier density N (the number of charge carriers per unit volume in the active region) and the photon density S (the number of photons per unit volume in the optical cavity) are considered. The optical phase $\phi(t)$ carries the information about the instantaneous frequency $\nu(t)$ of the optical signal, being $\nu(t)$ as the time derivative of the phase, $\nu(t) = \frac{1}{2\pi}\frac{d\phi(t)}{dt}$.

Carriers and photons are assumed to be uniformly distributed in the longitudinal and transversal directions, thus neglecting carrier diffusion and SHB effect. The RE system is presented for a single mode laser and the analysis can be extended to multi mode lasers, considering an equivalent set of equations for each optical mode.

Following the previous considerations, the RE model is expressed through the following differential equations:

$$\frac{dN}{dt} = \frac{I}{qV_{act}} - \frac{N}{\tau_N} - G(N,S)S \tag{3.1}$$

$$\frac{dS}{dt} = \Gamma G(N,S)S - \frac{S}{\tau_P} + \frac{\beta\Gamma N}{\tau_N} \tag{3.2}$$

$$\frac{d\phi}{dt} = \frac{1}{2}\alpha\left(\Gamma G(N,S) - \frac{1}{\tau_P}\right) \tag{3.3}$$

where Eq. 3.1 is the charge conservation equation and Eqs. 3.2, 3.3 are the optical field equations, for the photon density and the optical phase, respectively. The three terms on the right side of Eq. 3.1 account for the generation and depletion rate of charge carriers originated by: injected current *I,* $\left(\frac{I}{qV_{act}}\right)$, non-stimulated, $\left(\frac{N}{\tau_N}\right)$, and stimulated recombination, *(G(N,S)S)*, being q the electron charge, V_{act} the volume of the active region, τ_N the carrier lifetime and *G(N,S)* the optical gain.

The carrier lifetime τ_N is the time constant of the carrier decay due to non-stimulated recombination, such as non-radiative transitions and spontaneous emission. Carrier lifetime depends on N (see further in this Chapter, Eq. 3.16), but a constant value is enough for a qualitative description. The optical gain *G(N,S)* express the active material gain in terms of stimulated recombination processes and its dependence on N and S will be explained further in this Chapter.

In Eq. 3.2, the three terms on the right side of the equation express the stimulated recombination contribution, $\Gamma G(N,S)S$, the photon losses, $\frac{S}{\tau_P}$, and the spontaneous emission contribution, $\frac{\beta\Gamma N}{\tau_N}$, respectively. The confinement factor Γ appears in the stimulated emission term, accounting for the optical mode coupling to the active region. In a similar way, the spontaneous emission coefficient β refers to the portion of spontaneously emitted photons that couples into the lasing mode. The photon lifetime, τ_P, is the time constant of the photon decay in the cavity, due to photons exiting through the mirrors or being absorbed and scattered inside the cavity. Photon lifetime can be expressed as $\tau_P = (v_g(\alpha_{mir} + \alpha_{cav}))^{-1}$, where v_g is the group velocity and α_{mir} and α_{cav} are mirrors and cavity losses, respectively, with $\alpha_{mir} = \frac{1}{L} ln\left(\frac{1}{R_1 R_2}\right)$, where L is the cavity length and R_1, R_2 are the mirrors reflectivities.

Equation 3.3 describes the dependence of the optical phase on gain modulation or, equivalently, the well known phenomenon of carrier induced frequency modulation. In fact, the active material gain depends on the carrier density and carrier density affects the refractive index of the cavity, which in turn changes the emission wavelength of the laser. As it can be seen from the term difference in the right side of Eq. 3.3, when gain overcomes losses the instantaneous frequency increases and in the opposite case, the instantaneous frequency decreases. Thus an increase/decrease of carriers corresponds to an increase/decrease of the instantaneous frequency, resulting in an amplitude-phase coupling in directly modulated sources. During the steady state laser operation, the gain equals losses and carriers are ideally clamped to a stationary value, consequently the instantaneous frequency is ideally constant. The amplitude-phase coupling strength is expressed in Eq.3.3 by the line width enhancement factor, or Henry factor *a,* defined as $\Delta n'/\Delta n''$, where $\Delta n'$ and $\Delta n''$ are respectively the real and imaginary part of the refractive index [Henr 82].

The gain spectrum of a Single Quantum Well (SQW) 1.55 µm device with typical parameters is shown in Fig. 3.1 (left) as a function of the photon energy for different values of the carrier density. The gain peak increases and the gain spectrum broadens as the separation of quasi Fermi levels increases with the injected current. The gain peak as a function of the carrier density is shown in Fig. 3.1 (right). The differential

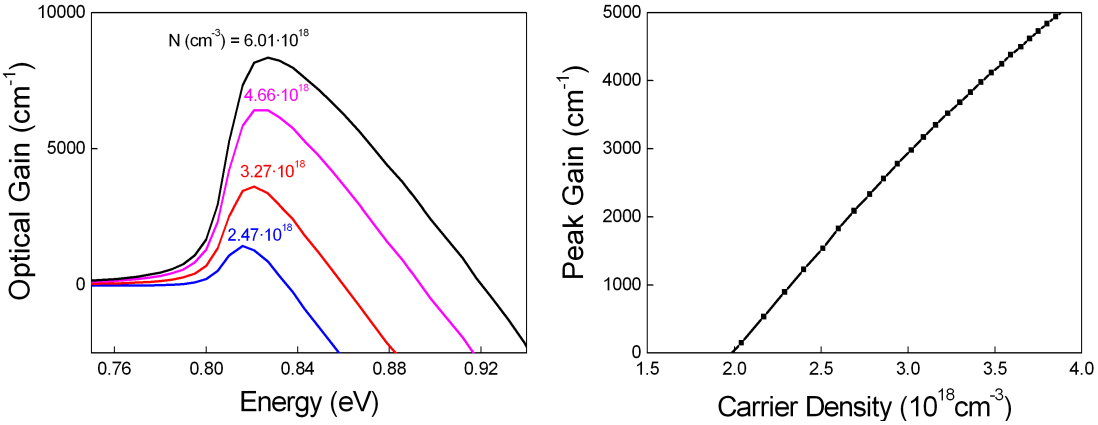

Figure 3.1: Calculated optical gain spectrum at different carrier density as a function of photon energy (left) and gain peak versus carrier density (right). Typical values of a SQW 1.55 µm laser have been used and the calculations have been performed with HAROLD 3.0 software [HARO].

gain $^{dG}/_{dN}$ is given by the slope of the graph and the transparency value N_{TR} by the intersection with the horizontal axis.

The optical gain *G(N,S)* is defined as the gain peak and its dependence on carrier and photon density is approximated with the following relation, assuming a linear dependence on N:

$$G(N,S) = \frac{v_g \frac{dG}{dN}(N - N_{TR})}{1 + \varepsilon S} \tag{3.4}$$

where ϵ is the gain compression factor, which accounts for the gain saturation occurring at high photon densities. At higher carrier densities the linear gain in QW devices saturates and a logarithmic function is necessary for modeling purposes [Cold 95].

3.1.1 Steady state solution

The stationary solutions of Eqs. 3.1, 3.2 and 3.4 are found by setting derivatives to zero and considering the threshold condition on gain. From Eq. 3.2, neglecting the spontaneous emission term, gain equals losses when:

$$G_{TH}(N,S) = \frac{1}{\Gamma \tau_P} \tag{3.5}$$

where $G_{TH}(N,S)$ is the gain at threshold. Using Eqs. 3.4 and 3.5, the threshold

condition on the carrier density is obtained:

$$N_{TH} = N_{TR} + \frac{1}{v_g \frac{dG}{dN} \Gamma \tau_P} \tag{3.6}$$

When carriers reach the threshold value, gain compensates losses and $G(N,S)$ and N are clamped to G_{TH} and N_{TH}, respectively. Current and carrier density are connected through Eq. 3.1: in the steady regime, for $\frac{dN}{dt} = 0$ and $I < I_{TH}$, $S = 0$ and Eq. 3.1 gives $N = \frac{\tau_N}{qV_{act}} I$, resulting in the following expression of the threshold current I_{TH}:

$$I_{TH} = \frac{qV_{act}}{\tau_N} N_{TH} \tag{3.7}$$

Solving Eq. 3.1, in the steady state above threshold and using Eqs. 3.5 and 3.7, the expression for photon density above threshold is obtained:

$$S = \Gamma \tau_P \left(\frac{I - I_{TH}}{qV_{act}} \right) \tag{3.8}$$

and the power output P can be calculated, considering that $P = SV_{opt} h\nu v_g \alpha_{mir}$, where V_{opt} is the optical cavity volume, $h\nu$ is the photon energy and $v_g \alpha_{mir}$ is the rate at which photons exit the mirrors. This yields the standard optical power vs. current (P-I) characteristic:

$$P = \eta_{slope}(I - I_{TH}) \tag{3.9}$$

with $\eta_{slope} = \frac{\alpha_{mir}}{\alpha_{mir} + \alpha_{cav}} \frac{h\nu}{q}$.

3.1.2 Small signal frequency response

Additional information about the laser operation can be obtained from the small signal analysis, equivalent to a first order expansion of the RE set. Let's consider that the laser is operating above threshold and assume that current, carriers and photons are described by the following :

$$I(t) = I_0 + i(\omega) e^{j\omega t} \tag{3.10}$$

$$N(t) = N_0 + n(\omega) e^{j\omega t} \tag{3.11}$$

$$S(t) = S_0 + s(\omega) e^{j\omega t} \tag{3.12}$$

where $I_0 \gg i(\omega)$, $N_0 \gg n(\omega)$ and $S_0 \gg s(\omega)$.

With the small signal approximation, the gain defined in Eq. 3.4 becomes:

$$G(N,S) = G_{TH} + v_g \frac{dG}{dN} n(\omega) e^{j\omega t} - \varepsilon G_{TH} s(\omega) e^{j\omega t} \tag{3.13}$$

By the substitution of Eqs. 3.10-3.13 into Eqs. 3.1 and 3.2, the RE in the small signal approximation for carrier and photon density are obtained:

$$j\omega n(\omega) = \frac{i(\omega)}{qV_{act}} - \frac{n(\omega)}{\tau_{\delta n}} - S_0 v_g \frac{dG}{dN} n(\omega) - \frac{1}{\Gamma \tau_P}(1 - \varepsilon S_0) s(\omega) \tag{3.14}$$

$$j\omega s(\omega) = \Gamma S_0 v_g \frac{dG}{dN} n(\omega) - \frac{1}{\tau_P} \varepsilon S_0 s(\omega) \tag{3.15}$$

where $\tau_{\delta n}$ is the differential carrier lifetime. To obtain an expression for $\tau_{\delta n}$, the recombination rate, *R(N)*, expressed in Eq. 3.1 via the carrier lifetime should be expressed through the recombination coefficients A, B and C, corresponding to non-radiative, spontaneous and Auger recombination, respectively [Cold 95]:

$$R(N) = \frac{N}{\tau_N} = AN + BN^2 + CN^3 \tag{3.16}$$

By definition, $\tau_{\delta \mathrm{n}}$ is the derivative of the carrier recombination rate with respect to N:

$$\frac{1}{\tau_{\delta n}} = \frac{d}{dN} R(N) = A + 2BN + 3CN^2 \tag{3.17}$$

Equations 3.14 and 3.15 can be arranged in the following matrix form:

$$\begin{pmatrix} \frac{i(\omega)}{qV_{act}} \\ 0 \end{pmatrix} = \begin{pmatrix} \left(j\omega + \frac{1}{\tau_{\delta n}} + v_g \frac{dG}{dN} S_0\right) & \frac{1}{\Gamma \tau_P}(1 - \varepsilon S_0) \\ \Gamma S_0 v_g \frac{dG}{dN} & -\left(j\omega + \frac{1}{\tau_P} \epsilon S_0\right) \end{pmatrix} \begin{pmatrix} n(\omega) \\ s(\omega) \end{pmatrix} \tag{3.18}$$

and the Cramer's rule can be applied to the linear system of Eq. 3.18 to obtain $n(\omega)$ and $s(\omega)$ as a function of $i(\omega)$. Thus, the normalized modulation response (MR), defined as $H(\omega) = \frac{s(\omega)}{i(\omega)} / \frac{s(0)}{i(0)}$, is easily obtained:

$$H(\omega) = \frac{\omega_r^2}{-\omega^2 + j\omega\gamma + \omega_r^2} \tag{3.19}$$

where:

$$\omega_r^2 = \frac{v_g \frac{dG}{dN} S_0}{\tau_P} + \frac{\varepsilon S_0}{\tau_{\delta n} \tau_P} \tag{3.20}$$

$$\gamma = \frac{1}{\tau_{\delta n}} + v_g \frac{dG}{dN} S_0 + \frac{\varepsilon S_0}{\tau_P} \tag{3.21}$$

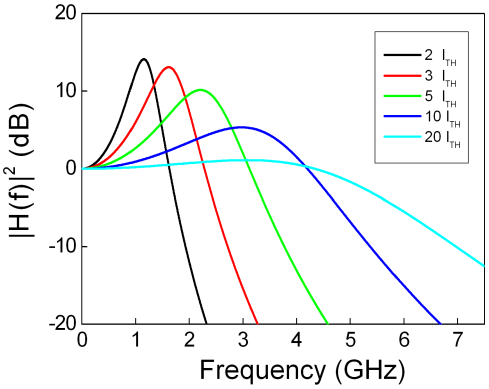

Figure 3.2: Amplitude modulation response versus frequency for different values of applied current in a bulk semiconductor laser.

Equation 3.19 describes the frequency response of a damped oscillator where ω_r is the relaxation oscillation pulsation and γ is the damping rate. Above threshold, the laser responds to an external stimulus, a variation of I, with a variation in the output power, oscillating at the relaxation oscillation frequency, $f_r = {}^{\omega_r}/_{2\pi}$ and decaying exponentially to its new value with time constant γ.

In most of the cases, the last term on the right hand side of Eq. 3.20 can be neglected [Cold 95] and ω_r and γ can be rewritten in the form:

$$\omega_r^2 = \frac{v_g \frac{dG}{dN} S_0}{\tau_P} \tag{3.22}$$

$$\gamma = \frac{1}{\tau_{\delta n}} + \frac{\omega_r^2}{4\pi^2} K \tag{3.23}$$

where the K-factor, which expresses the intrinsic speed of the laser, is defined as:

$$K = 4\pi^2 \left(\tau_P + \frac{\varepsilon}{v_g \frac{dG}{dN}} \right) \tag{3.24}$$

If S_0 is given as a function of I, using Eq. 3.8, ω_r is easily related to injected current I:

$$\omega_r^2 = \frac{v_g \frac{dG}{dN} \Gamma}{q V_{act}} (I - I_{TH}) \tag{3.25}$$

The squared modulus of the transfer function $H(\omega)$ is plotted in Fig. 3.2 for different bias currents. For each current, at low frequency, $H(\omega) = 1$, then a resonance peak occurs when approaching ω_r and at higher frequency $H(\omega)$ decreases. When the injected current increases, the resonance frequency moves towards higher values and the damping also increases, as expected from Eq. 3.25.

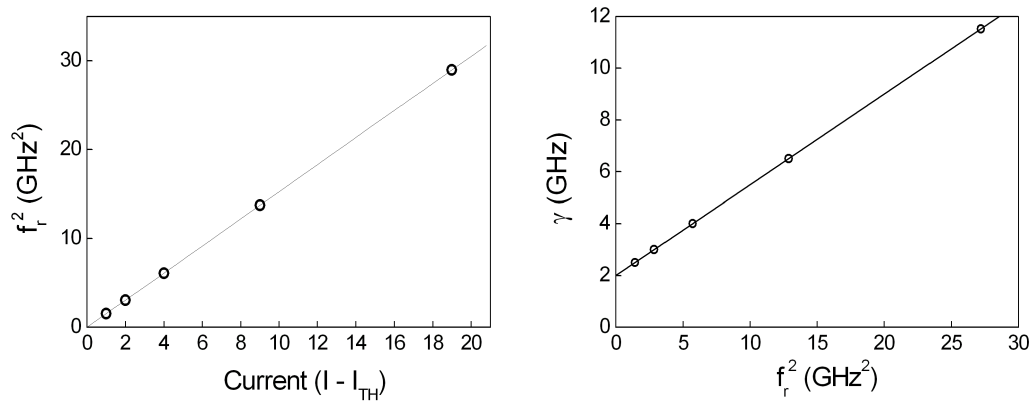

Figure 3.3: Square relaxation oscillation frequency versus injected current (left) and damping rate as a function of square relaxation oscillation frequency (right).

The definitions of relaxation oscillation frequency and damping, expressed in Eqs. 3.22 and 3.23, can be used for fitting the laser parameters to the laser MR measured at different bias levels. In Fig. 3.3 (right), the square relaxation oscillation frequency f_r^2, defined as $f_r^2 = \frac{\omega_r^2}{4\pi^2}$, is plotted as a function of $I - I_{TH}$. The curve intersects the horizontal axis in the origin, i.e. for $I = I_{TH}$, and the product $\frac{v_g \frac{dG}{dN} \Gamma}{qV_{act}}$ can be obtained from the slope of the graph. In Fig. 3.3 (right), γ is plotted as a function of f_r^2: the slope of the graph gives the K-factor and the intersection with the vertical axis, the inverse of the differential carrier lifetime at threshold, $\frac{1}{\tau_{\delta n}}$. This well known method for the extraction of some relevant internal laser parameters is used in Chapter 4, for the modulation response measurements of a long wavelength VCSEL.

From Eq. 3.19, the peak frequency, ω_P, and the 3 dB cut-off frequency ω_{-3dB}, are easily obtained by setting to zero the first derivative of Eq. 3.19 and setting Eq. 3.19 equal to 0.5, it follows:

$$\omega_P^2 = \omega_r^2 \left(1 - \frac{1}{2}\frac{\gamma^2}{\omega_r^2}\right) \tag{3.26}$$

$$\omega_{-3dB}^2 = \omega_r^2 + \sqrt{\omega_P^2 + \omega_r^2} \tag{3.27}$$

Because the damping increases proportionally with ω_r (Eq. 3.23) any attempt to drive the laser at higher currents for increasing ω_r will also flattens the modulation response, as shown in Fig. 3.2. Consequently, there is a maximum bandwidth that can be achieved and the optimum damping and maximum bandwidth occur when $\omega_P = 0$ and $\omega_{-3dB} = \omega_r$. This point is determined by the K-factor, which defines the maximum intrinsic modulation bandwidth of the laser:

$$f_{-3dB}|_{max} = \sqrt{2}\frac{2\pi}{K} \tag{3.28}$$

3.2 Electrical modeling of semiconductor lasers

The frequency dependence of the laser impedance below and above threshold can be obtained from the small signal RE set (Eqs. 3.14 and 3.15) introducing the relation between carrier density and applied voltage. Carrier density in the active region depends on Fermi levels energies and conduction and valence energy levels through the following formulas [Sze 81]:

$$N = N_{DC} \exp\left(\frac{q\phi_n - E_C}{K_B T}\right) \tag{3.29}$$

$$P = N_{DV} \exp\left(-\frac{q\phi_p - E_C}{K_B T}\right) \tag{3.30}$$

where N and P are the electron and holes densities, N_{DC} and N_{DV} are the reduced densities states in the conduction and valence band respectively, ϕ_n and ϕ_p are the quasi Fermi levels for electrons and holes, E_C and E_V are the bottom and the top energies of the conduction and valence bands respectively, K_B is the Boltzmann constant and T the temperature in Kelvin degrees.

By considering the quasi Fermi levels separation equals to the applied voltage, i.e. $V = \phi_n - \phi_p$, the product of electron and hole densities can be written as:

$$N \cdot P = N_{DC} N_{DV} \exp\left(\frac{qV - E_G}{K_B T}\right) = N_{DC} N_{DV} \exp\left(-\frac{E_G}{K_B T}\right) \exp\left(\frac{qV}{K_B T}\right) \tag{3.31}$$

From Eq. 3.31, two cases can be treated depending on the relation between n and p.

Case 1) $n = p$. Intrinsic and highly injected semiconductor, Eq. 3.31 becomes:

$$\begin{aligned} N \cdot P = N^2 &= N_{DC} N_{DV} exp\left(-\frac{E_G}{K_B T}\right) exp\left(\frac{qV}{K_B T}\right) \\ &\Rightarrow \sqrt{N_{DC} N_{DV}} exp\left(-\frac{E_G}{2K_B T}\right) exp\left(\frac{qV}{2K_B T}\right) = N_i^2 exp\left(\frac{qV}{2K_B T}\right) \end{aligned} \tag{3.32}$$

Case 2) $p = n + N_A \approx N_A$, with N_A the acceptors concentration. Highly p-doped semiconductor (same result is obtained for n-doped semiconductor), Eq. 3.31 becomes:

$$\begin{aligned} N \cdot N_A &= N_{DC} N_{DV} exp\left(-\frac{E_G}{K_B T}\right) exp\left(\frac{qV}{K_B T}\right) \\ &\Rightarrow N = \frac{N_{DC} N_{DV}}{N_A} exp\left(-\frac{E_G}{K_B T}\right) exp\left(\frac{qV}{K_B T}\right) = N_i exp\left(\frac{qV}{K_B T}\right) \end{aligned} \tag{3.33}$$

In general, the relation between carrier density N and applied voltage V can be

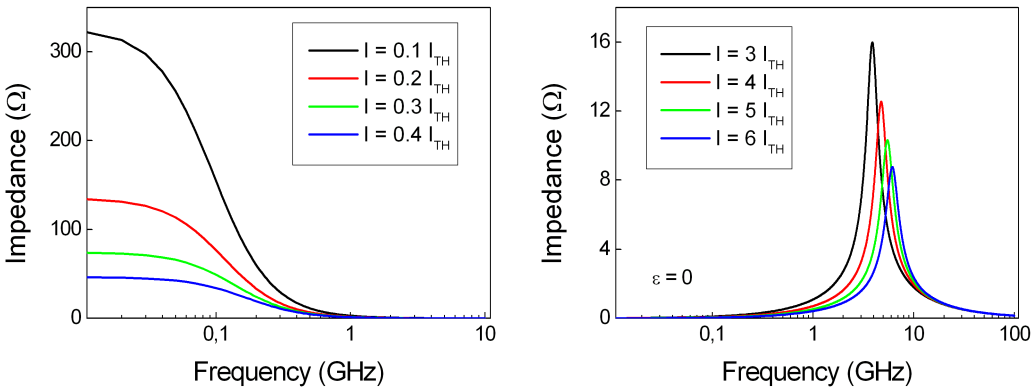

Figure 3.4: Impedance versus frequency for a bulk volume semiconductor laser biased below (left) and above threshold (right) .

expressed as:

$$N(V) = N_i exp\left(\frac{qV}{mK_BT}\right) = N_i exp\left(\frac{V}{mV_T}\right) \tag{3.34}$$

where N_i is the intrinsic carrier density for $V = 0$, which depends on dopant concentrations and intrinsic semiconductor characteristics, m is the ideality factor of the diode, ranging between 1 (highly doped semiconductor) and 2 (intrinsic semiconductor) and $V_T = \frac{K_BT}{q}$ is the thermal voltage.

By considering the small signal approximation of $N = N_0 + n(\omega)e^{i\omega t}$ and $V = V_0 + v(\omega)e^{i\omega t}$, where $n(\omega) \ll N_0$ and $v(\omega) \ll V_0$, Eq. 3.34 can be linearly approximated around the polarization point $V = V_0$ and becomes:

$$N(V) = N_0 + \left.\frac{dN}{dV}\right|_{V=V_0} \cdot v(\omega)e^{i\omega t} = N_0 + \frac{N_0}{mV_T} \cdot v(\omega)e^{i\omega t} \tag{3.35}$$

When the laser is biased below threshold, $S_0 \approx 0$ and, by substituting Eq. 3.35 into Eq. 3.14, the small signal carrier density rate equation becomes:

$$i\omega \frac{N_0}{mV_T} v(\omega) = \frac{i(\omega)}{qV_{act}} - \frac{1}{\tau_{\delta n}} \frac{N_0}{mV_T} v(\omega) \tag{3.36}$$

and the frequency dependent impedance below threshold is:

$$Z(\omega)_{I<I_{TH}} = \frac{v(\omega)}{i(\omega)} = R_d \frac{1}{1 + i\omega\tau_{\delta n}} \tag{3.37}$$

where R_d is the differential resistance of the junction, when $V = V_0$ and $N = N_0$, defined as $R_d = \frac{mV_T}{N_0} \frac{\tau_{\delta n}}{qV_{act}}$. Equation 3.37 describes the frequency response of a single pole system, such as a RC low pass filter, which time constant is equal to the differential carrier lifetime $\tau_{\delta n}$ given in Eq. 3.17. In Fig. 3.4 (left) the impedance below threshold is plotted as a function of frequency for different bias currents.

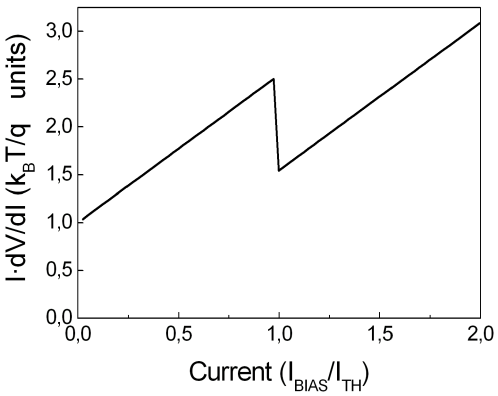

Figure 3.5: Calculated $I \cdot {}^{dV}/_{dI}$ (in ${}^{K_B T}/_{q}$ units) as a function of applied current, for $m = 1$.

The substitution of Eq. 3.35 into Eq. 3.14, when the laser is biased above threshold, gives the following expression for the impedance as a function of frequency:

$$Z(\omega)_{I>I_{TH}} = \frac{v(\omega)}{i(\omega)} = R_d \frac{i\frac{\omega}{\tau_{\delta n}} + \frac{\epsilon S_0}{\tau_{\delta n}\tau_P}}{-\omega^2 + i\omega\gamma + \omega_r^2} \tag{3.38}$$

The impedance peak corresponds to the resonance frequency of the laser, which also increases with increasing bias. Figure 3.4 (right) shows the impedance dependence on frequency for different bias currents above threshold with $\varepsilon = 0$.

The dynamic resistance R_d of a semiconductor laser is obtained differentiating the voltage V with respect to the applied current I, at the polarization point $I = I_0$, $R_d = \frac{dV}{dI}\Big|_{I=I_0}$. Considering a simple equivalent electrical circuit, consisting of a diode representing the p-n junction and a series resistance R_S accounting for the electrical path from the contacts to the junction, the voltage applied to the device can be written as:

$$V = R_S I + m V_T \ln\left(\frac{I}{I_S}\right) \tag{3.39}$$

where I_S is the diode saturation current. Assuming that the voltage drop at the junction is constant above threshold, i.e. the carrier density is clamped to the threshold value, the derivative of V is readily obtained, giving:

$$I_0 \left.\frac{dV}{dI}\right|_{I=I_0} = m V_T + R_S I_0 \qquad I_0 < I_{TH} \tag{3.40}$$

$$I_0 \left.\frac{dV}{dI}\right|_{I=I_0} = R_S I_0 \qquad I_0 > I_{TH} \tag{3.41}$$

Consequently, a kink in correspondence of I_{TH} is expected in the plot of $I\frac{dV}{dI}$, as shown in Fig. 3.5, and from the dynamic resistance of the diode is then possible

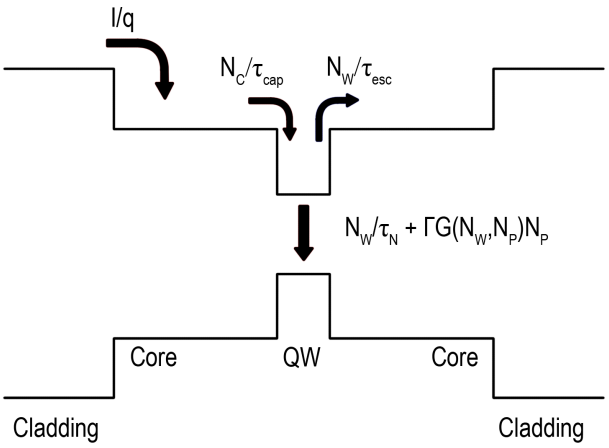

Figure 3.6: Schematic diagram of a QW laser structure and carrier capture, re-emission, and recombination processes.

to obtain experimentally the ideality factor m of the diode and the series resistance R_S.

3.3 Carrier capture and escape in Quantum Well lasers

The previous analysis of the dynamical properties of bulk semiconductor lasers can be extended to Quantum Well (QW) semiconductor lasers modifying the RE set presented in Sec. 3.1. In our model, we assume that vertical and lateral carrier distribution in the core are homogeneous and neglect carrier transport effects between the wells in MQW structures. As in Sec. 3.1, a single-particle RE model for a laser emitting in a single longitudinal mode is presented. The model described here can be found in [Cold 95] and [Esqu 99].

The structure of a QW laser and the main processes occurring in it are depicted in Fig. 3.6. We consider the total number of carriers in the core region, N_C, and in the QW's, N_W, and the total number of photons in the the cavity, N_P. Carriers are injected from the cladding layers at a rate I/q, building up a population of unconfined carriers in the core. Carriers in the core leave the core region and enter the QW's at a rate N_C/τ_{cap}, being τ_{cap} the capture time of carriers in the core region. Carriers in the QW's, N_W, can be re-emitted in the core region, or recombine via stimulated emission or via other non-stimulated recombination mechanisms. These contribution are considered respectively via the escape rate of carriers in the QW's, N_W/τ_{esc}, where τ_{esc} is the escape time constant of QW's carriers, via the non-

stimulated recombination rate, N_W/τ_N, where τ_N is the carrier lifetime as defined in Sec. 3.1, and via stimulated emission occurring at the rate $\Gamma G(N_W, N_P)N_P$, where $G(N_W, N_P)$ is the optical gain.

Thus the RE set for a QW laser can be written as:

$$\frac{dN_C}{dt} = \frac{I}{q} - \frac{N_C}{\tau_{cap}} + \frac{N_W}{\tau_{esc}} \tag{3.42}$$

$$\frac{dN_W}{dt} = -\left(\frac{1}{\tau_N} + \frac{1}{\tau_{esc}}\right) N_W + \frac{N_C}{\tau_{cap}} - N_P \Gamma G(N_W, N_P) \tag{3.43}$$

$$\frac{dN_P}{dt} = \left(\Gamma G(N_W, N_P) - \frac{1}{\tau_P}\right) N_P \tag{3.44}$$

The steady state solutions of Eqs. 3.42-3.44 are obtained by setting to zero the time derivatives. The dependence of τ_N, τ_{cap} and τ_{esc} on the carrier numbers in the core and in the QW's is neglected for giving a simple expressions and a clear physical interpretation. An analysis of the steady state solutions considering the effect of carrier density on the carrier time constants leads to the same qualitative results.

The steady state number of carriers in the core, N_{C0}, is obtained from Eq.3.42, $N_{C0} = \eta N_{W0} + \tau_{cap} {}^{I_0}/_q$, where $\eta = \tau_{cap}/\tau_{esc}$, N_{W0} is the steady state number of carriers in the QW's and I_0 is the bias current. The value η defines the ratio between carriers in the core and in the QW's in the equilibrium state, i.e. $I_0 = 0$, and it is determined by the band structure of the laser. The condition $\eta \ll 1$ must hold for high speed operation, as it is equivalent to say that the rate at which carriers leave the QW's is much smaller than the rate at which they enter the QW's from the core, thus minimizing the effect of carrier escape.

Below threshold, Eqs. 3.42 and 3.43 give :

$$N_{C0} = \eta \frac{I_0 \tau_N}{q} \left(1 + \frac{\tau_{esc}}{\tau_N}\right) \tag{3.45}$$

$$N_{W0} = \frac{I_0 \tau_N}{q} \tag{3.46}$$

Below threshold both N_{C0} and N_{W0} increase with the applied current I_0. Equation 3.45 describes the effect of the core region as an additional reservoir of carriers with respect the bulk volume lasers: if $\tau_{esc} \ll \tau_N$, (escape processes are dominant with respect to carrier recombination) the core and QW's carrier numbers are at the equilibrium, on the opposite if $\tau_{esc} \gg \tau_N$, the carrier number in the core is dominated by the accumulation of carriers due to finite value of capture time and the ratio ${}^{N_{C0}}/_{N_{W0}}$ is far above the equilibrium.

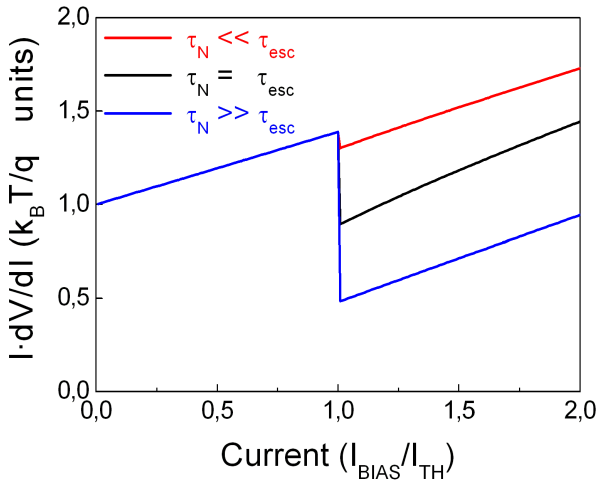

Figure 3.7: Calculated $I \cdot {}^{dV}/_{dI}$ (in ${}^{K_B T}/_{q}$ units with $m = 1$) as a function of applied current for a QW's laser.

Above threshold, neglecting ϵ and assuming ideal clamping of carrier at the threshold value, the carrier number in the QW's becomes $N_{W0} = N_{Wth} = \frac{I_{TH}\tau_N}{q}$ and the steady state solution of Eq. 3.42 gives:

$$N_{C0} = \eta N_{Wth} + \tau_{cap}\frac{I_0}{q} = \tau_{cap}\frac{I_0 + (\tau_N/\tau_{esc})\, I_{TH}}{q} \tag{3.47}$$

Above threshold the carrier number in the QW's is clamped to N_{Wth} and the carrier number in the core increases with the bias current I_0.

In the case of a QW laser, the external voltage is related to the quasi-Fermi level separation of the carriers in the core, not to that of the QW carriers. The relationship between the external voltage and the core carrier density can be deduced similarly to that of a bulk laser (Sec. 3.2). Using this relationship (Eq. 3.34) and from Eqs. 3.45, 3.47, the dynamic resistance, $R_d = \frac{dV}{dI}\big|_{I=I_0}$, below and above threshold is obtained as:

$$I_0 \left.\frac{dV}{dI}\right|_{I=I_0} = mV_T + R_S I_0 \qquad I_0 < I_{TH} \tag{3.48}$$

$$I_0 \left.\frac{dV}{dI}\right|_{I=I_0} = \frac{mV_T}{\left(I_0 + \frac{\tau_N}{\tau_{esc}} I_{TH}\right)} I_0 + R_S I_0 \qquad I_0 > I_{TH} \tag{3.49}$$

Thus the kink depth in the dynamic resistance at threshold is $1 + \frac{\tau_N}{\tau_{esc}}$ as shown in Fig. 3.7 for different values of τ_N/τ_{esc}.

The solution of Eqs. 3.42-3.44 in the small signal regime is obtained expanding the variables around their steady state values, e.g. $I = I_0 + i(\omega)e^{i\omega t}$. We assume that the differential values of τ_{cap} and τ_{esc} are the same in the small signal approximation

and $\tau_{\delta n}$ is the differential carrier lifetime in the QW's.

As in Sec. 3.1, the resulting linear system with variables $i(\omega)$, $n_C(\omega)$, $n_W(\omega)$ and $n_P(\omega)$ can be expressed in a matrix form:

$$\begin{pmatrix} \frac{i(\omega)}{q} \\ 0 \\ 0 \end{pmatrix} = \begin{pmatrix} \left(j\omega + \frac{1}{\tau_{cap}}\right) & -\frac{1}{\tau_{esc}} & 0 \\ -\frac{1}{\tau_{cap}} & j\omega + \frac{1}{\tau_{\delta n}} + \frac{1}{\tau_{esc}} + \omega_r^2\tau_P & \frac{1}{\tau_P} \\ 0 & -\omega_r^2\tau_P & j\omega + \omega_r^2\frac{\epsilon}{G_0'} \end{pmatrix} \begin{pmatrix} n_C(\omega) \\ n_W(\omega) \\ n_P(\omega) \end{pmatrix} \tag{3.50}$$

where the QW's differential gain is $G_0' = Ad_w\frac{dG_0}{dN_w}$ with A being the active region area and d_w the total QW thickness, and the resonance frequency and damping are defined as:

$$\omega_r^2 = \frac{v_g G_0' S_0}{\tau_P} \tag{3.51}$$

$$\gamma = \frac{1}{\tau_{\delta n}} + \frac{\omega_r^2}{4\pi^2}\left(\tau_P + \frac{\varepsilon}{G_0'}\right) \tag{3.52}$$

Applying the Cramer's rule to Eq. 3.50, the modulation response and the intrinsic impedance are directly obtained, considering that the small signal voltage is proportional to the small signal core carrier density. The exact solution of Eq. 3.50 is a relatively complicated equation [Cold 95, Esqu 99] that can be greatly simplified for a better intuitive understanding, if some restrictions are imposed.

Assuming that $\eta \ll 1$, the modulation response $H(\omega)$ and the intrinsic impedance $Z(\omega)$ can be written as :

$$H(\omega) = \frac{\omega_r^2}{(1 + j\omega\tau_0)\left(\omega_r^2 + j\omega\gamma - \omega^2\right)} \tag{3.53}$$

$$Z(\omega) = R_d\frac{1}{1 + j\omega\tau_0}T(\omega) \tag{3.54}$$

with $T(\omega)$, below threshold:

$$T(\omega) = \frac{1 + j\omega\tau_I}{1 + j\omega\tau_{\delta n}} \tag{3.55}$$

and above threshold:

$$T(\omega) = \frac{\omega_r^2 + j\omega\gamma_I - \omega^2}{\omega_r^2 + j\omega\gamma - \omega^2} \tag{3.56}$$

where $\tau_I^{-1} = \tau_{\delta n}^{-1} + \tau_{esc}^{-1}$ and $\gamma_I = \tau_{esc}^{-1} + \gamma$. The dynamic resistance of the diode

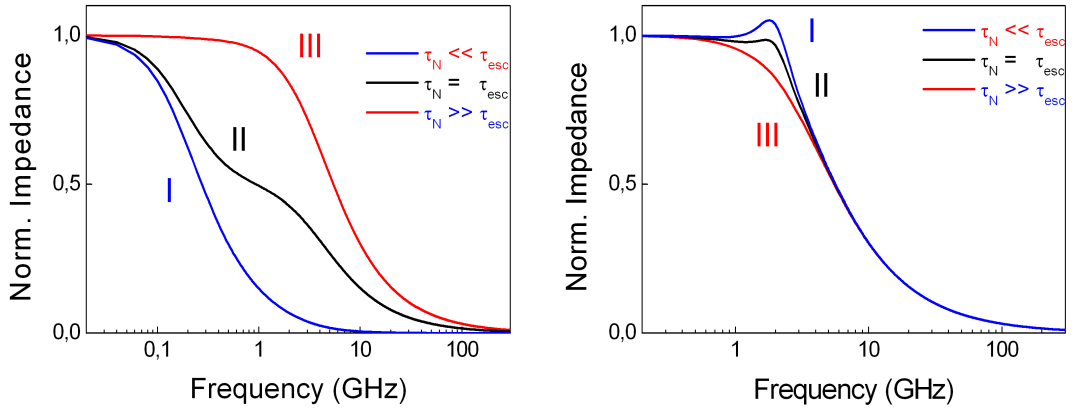

Figure 3.8: Magnitude of the normalized impedance $|Z(\omega)/Z(0)|$ versus frequency below (left) and above (right) threshold for three different cases of the ratio τ_N/τ_{esc}.

R_d has been defined in Eq. 3.49 and the time constant τ_0 is equal to τ_{cap} if the effect of the capacitance C_{sc} of space charge region in the p-n junction is neglected, otherwise $\tau_0 = \tau_{cap} + R_S C_{sc}$. The assumption $C_{sc} = 0$ allows a clear explanation of the phenomena related with capture escape and is valid in general for QW's laser. A complete treatment including a finite value of C_{sc} is provided in ref. [Esqu 99].

From Eq. 3.53, it can be seen that the effect of the carrier capture and escape processes on the modulation response is only an additional low pass filter with time constant τ_0 with respect to the bulk semiconductor laser.

The intrinsic impedance depends on $T(\omega)$ whose poles and zeros positions change with the ratio $\tau_{\delta n}/\tau_{esc}$ via the parameters τ_I and γ_I.

Depending on $\tau_{\delta n}/\tau_{esc}$, qualitatively different behaviors of the frequency dependent impedance are observed, which are plotted in Fig. 3.8.

Three different cases are discussed, considering different values of $\tau_{\delta n}/\tau_{esc}$ with the previous assumption $\eta \ll 1$.

Case I: $\tau_{\delta n} \ll \tau_{esc}$.

In this case, $T(\omega) = 1$ both below and above threshold and the impedance simplifies to a simple low-pass filter with time constant τ_0. The differential diode resistance (Eq. 3.49) takes the expression of conventional diodes, both below and above threshold $R_d = mV_T/I_0$.

Case II: $\tau_{\delta n} = \tau_{esc}$.

Below threshold, two poles at τ_{eff} and τ_0 and one zero at τ_I with significantly different values are observed in the impedance. Above threshold, the impedance exhibits a peak with relative height $T(\omega_r) = 1 + (\tau_{esc}\gamma)$ at the relaxation frequency and a low-pass filter due to the influence of τ_0.

Case III: $\tau_{\delta n} \gg \tau_{esc}$.

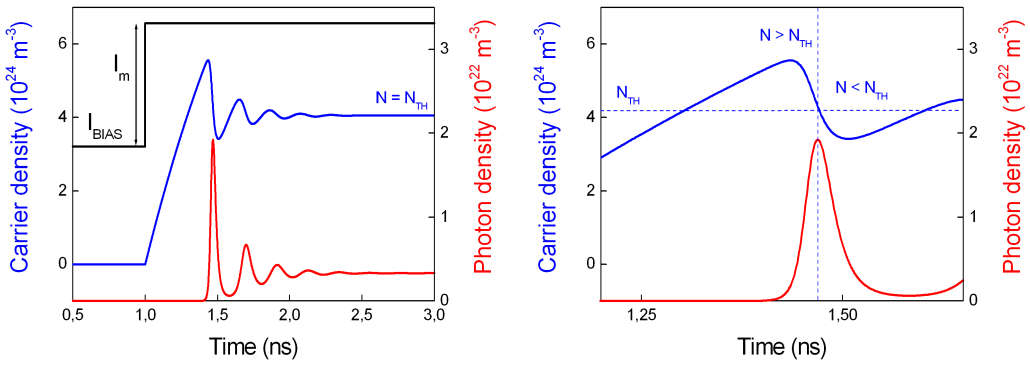

Figure 3.9: (left) Transient behavior of a laser at the turn-on: current (black), carrier density (blue) and photon density (red). (right) Enlarged view during the first spike of relaxation oscillations.

Below threshold the pole at τ_0 and the zero at τ_I are both at high frequencies, thus the pole at $\tau_{\delta N}$ dominates the frequency dependent impedance.

Above threshold, there is a pronounced peak at the relaxation frequency. A large drop is observed at threshold in the intrinsic differential diode resistance and R_d vanishes above threshold due to clamping of the carrier number in the core. In this case, the behavior of R_d is the same as for ideal bulk lasers, in which the carrier number in the active region is clamped above threshold.

3.4 Gain Switching

The transient behavior at the turn-on of a laser exhibits damped oscillations of the output power before the steady state operation is reached, as expected from the discussion in the previous section. Figure 3.9 (left) shows a numerical simulation of the current, carriers and photons evolution at the turn-on of the laser, when the applied current is in the form $I(t) = I_{BIAS} + I_m rect(t)$, where I_{BIAS} is the low level current value, I_m is the step amplitude and the function $rect(t)$ is an instantaneous step increase. From the rate equation for carriers, Eq. 3.1, if a step current from below to above threshold is applied, carrier density increases following:

$$N(t) = N_m \left(1 - \exp\left(-\frac{t}{\tau_N}\right)\right) + N_{BIAS} \tag{3.57}$$

where $N_{BIAS} = \frac{I_{BIAS}\tau_N}{qV_{act}}$, $N_m = \frac{I_m\tau_N}{qV_{act}}$. In fact, carriers respond to the step-like current excitation as a low pass filter with time constant equal to the carrier lifetime τ_N. Carriers increase following Eq. 3.57 and overcomes N_{TH} starting stimulated emission and photon generation, as shown in Fig. 3.9 (left). Photon density grows

and depletes carrier density by stimulated recombination, causing N to decrease during the leading edge of the first spike of relaxation oscillations, see Fig. 3.9 (right). When $N < N_{TH}$, losses overcome gain, photon density decreases and the pulse tends to extinguish. Then, carrier density grows again as the applied current is still above threshold, causing the process to repeat and starting the oscillatory behavior of carriers and photons until the steady state is reached with the clamping of carrier density to N_{TH}.

The damped oscillating behavior of a laser can be used to generate short pulses. If only the first spike of the relaxation oscillations is generated, fast pulses can be obtained, with duration in the order of the inverse of relaxation oscillation frequency and peak power several times greater than the continuous power output. This technique is called *gain-switching* [Lau 88] as it relies on the principle that the gain is switched above and below threshold during the pulse duration. It can be obtained by optical excitation from another laser or electrical excitation when the laser is modulated by an external electrical source. Two kinds of current waveforms are commonly used for gain switching a laser: a pulse train with fast rising edge or a radio frequency (RF) sinusoid.

The gain switching technique has the advantage with respect to other pulse generation methods, such as mode-locking or Q-switching [Vasi 00], to be simple and flexible. In fact, in both mode-locking and Q-switching techniques, an absorber section must be included in the cavity, thus the device must be fabricated *ad hoc* or an external cavity has to be built, whereas pulse generation from gain-switched (GS) semiconductor lasers is obtained simply by direct modulation with an electrical current source. Also, the pulse repetition rate of a mode-locked laser is fixed by the cavity length, whereas with GS sources the pulse train period is equal to the current modulation frequency and consequently can be easily varied. On the other hand, GS sources generate highly *chirped* pulses with a relevant amount of jitter because of the carrier induced frequency modulation at the laser turn-on and the stochastic fluctuations of spontaneous emission preceding pulse generation. However, the chirped nature of GS pulses can be used to compress the pulse with dispersion compensating fiber or Fiber Bragg Gratings and optical injection (see next Section) can be employed to reduce the amount of jitter.

Figure 3.10 show the numerical simulations of a GS laser, obtained with the implementation of the RE set of Eqs. 3.1-3.3. Two electrical waveforms of the injected current are considered: rectangular (Fig. 3.10 left) and sinusoidal (Fig. 3.10 right).

The highly chirped character of pulses generated from GS lasers affects the pulse

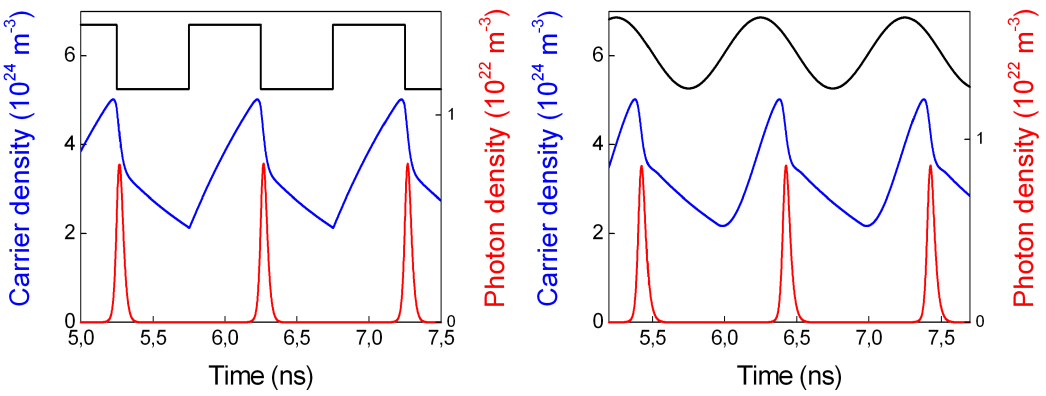

Figure 3.10: GS pulse train generation by rectangular and sinusoidal electrical modulation: current (black), carrier density (blue) and photon density (red).

spectrum as shown in Fig. 3.11, where the simulation results for a GS laser, obtained with different modulation parameters, are plotted in the temporal and spectral domains. The pulse spectrum is obtained applying a Discrete Fourier Transform (DFT) algorithm to the slow varying envelope of the pulse, defined as $\sqrt{P\,(t)}\exp\left(j\phi(t)\right)$, where $P(t)$ and $\phi(t)$ are the pulse intensity and phase obtained with the RE model, respectively.

The single and double peaked pulses are generated varying the bias current. At a low value of I_{BIAS} corresponds a brief current transition above threshold and a low resonance frequency, thus a single pulse from the first spike of relaxation oscillations. At higher I_{BIAS}, also the second spike of relaxation oscillations is excited, resulting in a double peaked pulse. The non-linear character of the chirp is clearly shown in Fig. 3.11 (a), as it follows from carrier oscillations around threshold. This characteristic chirp produces an asymmetric spectral intensity, typical of GS lasers, with a shoulder on the positive frequency side, which corresponds to the rising edge of the pulse. From the pulse spectrum is also clear the signature of the relaxation oscillation frequency, f_r, which produces the quasi sinusoidal modulation of the spectrum in Fig. 3.11 (b). This behavior is even more pronounced in the double peaked pulse of Fig. 3.11 (c)-(d), in which the temporal peak spacing is roughly equal to the inverse of the peak spectral spacing, i .e. the relaxation oscillations frequency. The spectral period in Fig. (b) (d) is not constant over the entire spectrum, as during the pulse the instantaneous f_r (which has been derived in the small signal approximation) is not constant but varies with the applied current on a large signal scale.

It's interesting to notice that the previously described spectral characteristics of GS laser pulses have not received much attention in literature [Lau 88]. The chirp of GS lasers is often assumed linear or quasi linear, as it is assumed in pulse

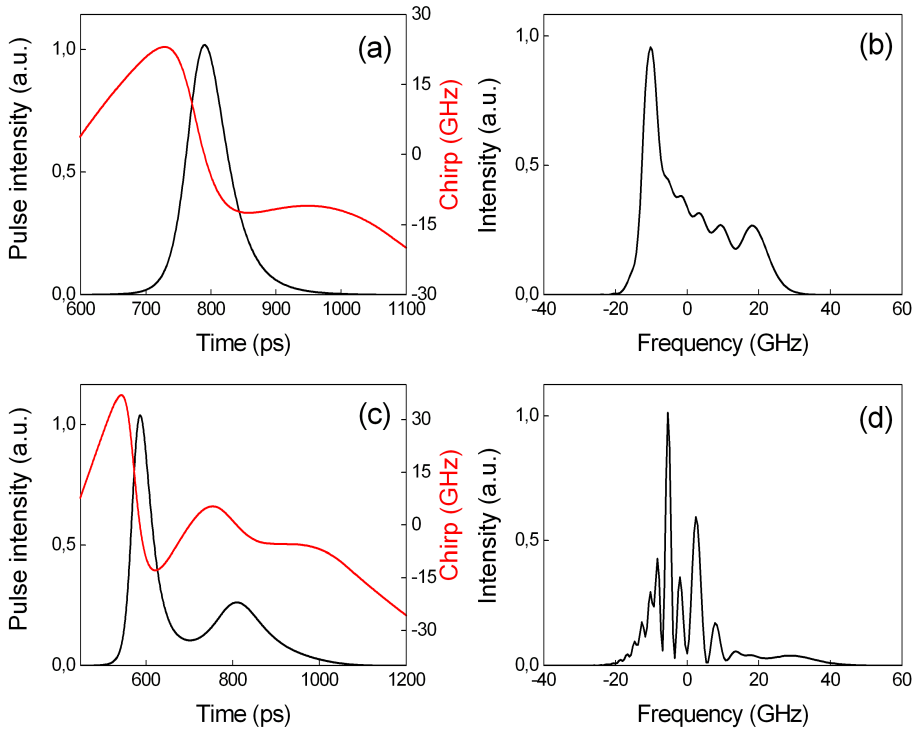

Figure 3.11: Simulated temporal intensities, chirp (a)-(c) and spectral intensities (b)-(d) of the pulse obtained from a GS laser at different I_{BIAS}.

compression with fiber dispersion compensation experiments [Taka 87, Liu 91], while the asymmetric spectrum is a clear evidence of its non linearity. Also, the spectral signature of f_r, more evident in the double peaked pulse, but also present in the single peaked pulse, has been usually neglected in most of the works on GS lasers [Barr 98, Vu 08]. This could be due to the fact that it is often hidden by the spectral resolution in practical experiments.

3.5 Optical injection of semiconductor lasers

The static and dynamic behavior of a semiconductor laser can be modified if additional physical elements are introduced, corresponding to additional terms into the RE set described in Sec. 3.1. In optically injected lasers, the additional variables come from an external source injecting coherent light into the laser. A schematic configuration of optical injection in semiconductor lasers is depicted in Fig. 3.12, where unidirectional light injection from one laser, referred as the master laser (ML), to another, referred as the slave laser (SL), is obtained with two different schemes for EE and vertical cavity lasers using unidirectional optical components, i.e. an optical isolator and an optical circulator.

Optical injection is a coherent phenomenon and it has to be treated with the field rate equations, in which the photon population is expressed via the optical field $E(t) = \sqrt{P(t)}\exp(j\omega t)$, where *P(t)* is the intensity and ω is the field angular pulsation. The photon RE in the slave laser can then be expressed as [Nori 08]:

$$\frac{dE(t)}{dt} = \frac{(1-j\alpha)}{2}\left(v_g\Gamma G - \frac{1}{\tau_P}\right)E(t) + \kappa\sqrt{P_{inj}}\exp(-j\Delta\omega t) + \beta\frac{N}{\tau_N} \tag{3.58}$$

where P_{inj} is the injected power from the ML to the SL, κ is the coupling coefficient and $\Delta\omega$ is the angular pulsation difference between the ML and the SL. The other variables in Eq. 3.58 have been defined for the single particle RE set of Eqs. 3.1-3.3, expect for the gain , that is now defined as a function of the optical field:

$$G = \frac{v_g\frac{dG}{dN}(N - N_{TR})}{1 + \epsilon\left|E(t)\right|^2} \tag{3.59}$$

The coupling coefficient is defined as:

$$\kappa = \frac{1}{\tau_L}\left(\frac{1}{r_2} - r_2\right)\sqrt{\eta_{inj}} \tag{3.60}$$

where r_2 is the output mirror reflectivity, τ_L is the VCSEL round trip time, $\frac{2L}{v_g}$, and η_{inj} is the coupling efficiency of the injected light to the optical field in the VCSEL cavity.
By solving Eq. in the steady state regime, the following condition on the detuning range for injection locking is found [Chan 08]:

$$-\kappa\frac{\lambda^2}{2\pi c}\sqrt{\frac{P_{inj}}{P_0}} \leq \Delta\lambda \leq \frac{\lambda^2}{2\pi c}\sqrt{\frac{P_{inj}}{P_0}}\sqrt{1+\alpha^2} \tag{3.61}$$

where $\Delta\lambda = \lambda_{master} - \lambda_{slave}$ is the wavelength detuning, P_{inj} is the injected power and P_0 is the power emitted from the SL.

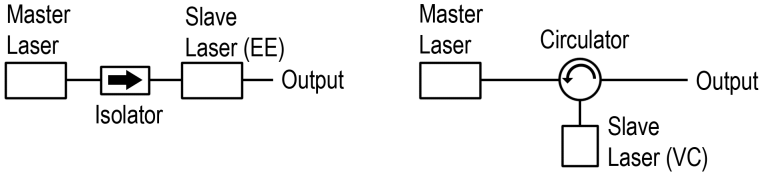

Figure 3.12: Experimental set-up for optical injection of semiconductor lasers: edge emitting (EE) and vertical cavity (VC).

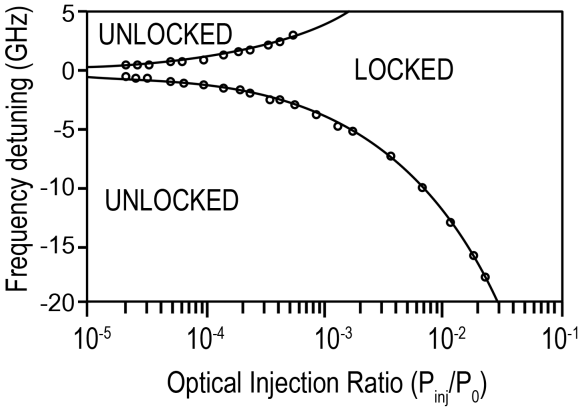

Figure 3.13: Locking range: calculated (line) and experimental (circles), adapted from [Hui 91].

The locking range is asymmetric due to the linewidth enhancement factor. The physical origin of this asymmetry can be explained qualitatively as follows. The external light injection reduces the carrier density which will in turn reduce the gain of the slave laser. As the linewidth enhancement factor couples the gain and the phase inside the slave cavity, the gain change through α gives a red shift of the slave-cavity wavelength. Therefore, the slave laser tends to be locked to a wavelength longer than its lasing wavelength (red side) [Chan 08].

A two-dimensional stability plot can be generated with wavelength detuning as the vertical axis and injection ratio as the horizontal axis, which is usually used to determine the locking condition, including injection regime and locking range. Figure 3.13 shows an example of this plot comparing the theory and experiments, by plotting Eq. 3.61 and by measuring the locking range, respectively.

If we use control theory to solve the stability of the injection-locked RE, there exist unstable and stable locking regions within the locking range shown in Eqs. 3.61. In the unstable region, various nonlinear phenomena could take place, such as pulsation and chaos. These effects have been studied by a number of groups. Stable regime of injection locking is often used for the performance improvement of directly modulated lasers, such as the increase of maximum modulation frequency and jitter reduction. In Chapter 6 are presented the results obtained with a GS VCSEL subjected to optical injection, resulting in a jitter reduction of the generated pulses.

Chapter 4

Opto-electrical characterization of 1550 nm VCSELs with tunnel junction

In this Chapter, the opto-electrical properties of 1.55 μm VCSELs with Tunnel Junction (TJ) are investigated. The VCSEL structure is presented and the static electrical measurements are discussed, through a comparison with standard p-n junction laser diodes and an equivalent circuit including the TJ. Static current-voltage measurements are fitted to the equivalent circuit and the bias dependence of the circuit parameters is investigated. A frequency dependent analysis of the VCSEL impedance above and below threshold is presented, including carrier capture-escape effects in QW's structures. This analysis allows the understanding of the unconventional features of the device and leads to the extraction of carrier time constants and recombination coefficients. An equivalent small signal circuit is proposed for the modeling of the electrical parasitics of the packaged device and their values are obtained with the fitting to the frequency dependent impedance measurements. The measured modulation response of the packaged device is presented and a transfer matrix approach is proposed for the removal of the bias independent parasitics and the extraction of intrinsic laser parameters. A complete list of the VCSEL parameters obtained from impedance and modulation response measurements is reported at the end of the Chapter.

4.1 Introduction

Long wavelength VCSELs are becoming a real alternative to standard EE lasers in high speed communication applications [Koya 06]. The TJ based VCSELs emitting at 1.55 μm have recently demonstrated 40 Gb/s data rates [Hofm 11] and modulation bandwidths in excess of 15 GHz [Mull 09]. Commercial devices up to 10 Gb/s are already available at a competitive price. A complete characterization and modeling of the DC and high frequency electrical properties of packaged VCSELs is necessary to properly design the driving electronics, as well as to determine the main parameters needed to simulate the device performance in optical links. In addition, measurements of the high frequency electrical impedance below threshold can provide important information about intrinsic physical parameters [Esqu 99, Shte 95]. Equivalent circuit models for semiconductor lasers have been employed since the 80s [Katz 81, Tuck 83], with different degrees of complexity. Several circuit models have been proposed for conventional and TJ based VCSELs [Zhu 10], based on the particular geometry and considering different types of parasitics. In general these circuits are compared with on-wafer measurements performed with microwave coplanar probes, avoiding the parasitics of submount, package and bonding wires. However, these parasitics are part of the electrical access when packaged devices are used in communication applications, and therefore a complete characterization of the equivalent circuit elements is needed. In this Chapter, the experimental characterization of the DC and high frequency electrical properties of packaged 1.55 μm TJ based InAlGaAs VCSELs is presented a procedure to determine the elements of the equivalent circuit and to extract intrinsic physical parameters is proposed [Cons 11a].

4.2 VCSEL structure and measurement set-up

The laser is a commercial (Raycan) fiber pigtailed 2.5 Gb/s VCSEL, packaged in TO-56 can. It is based on InAlGaAs active region, tunnel junction (TJ), air-gap aperture and InAlGaAs/InAlAs mirrors [Park 06]. The VCSEL structure is shown schematically in Fig. 4.1. The active region consist of seven pairs of strain compensated 7 nm thick InAlGaAs QWs.

From top to bottom, the VCSEL structure consists of the top DBR mirror with 28 pairs of InAlGaAs/InAlAs layers with 99.9% reflectivity, coated with a high Au reflective mirror. The TJ and the 7-QWs active region are sandwiched between two 2.5 λ-thick N-InP spacer layers. The diameter of the active region is 9 μm [Rayc 09] and the air gap region provide optical and current confinement. The bottom DBR

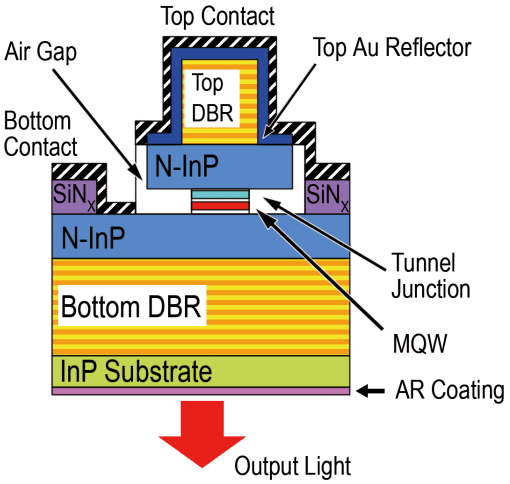

Figure 4.1: Schematics of the VCSEL structure (adapted from [Park 06]).

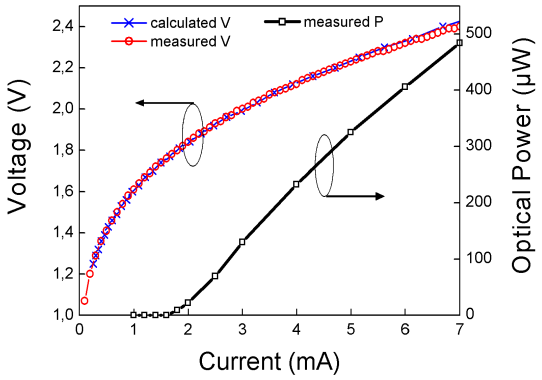

Figure 4.2: Experimental *P-I-V* and calculated *I-V* characteristics

mirror is composite of 38 pairs of InAlGaAs/InAlAs layers with 99.5% reflectivity, grown on the InP substrate with anti reflection coating. The VCSEL is bottom emitting, and both contacts are on the top side of the VCSEL structure.

The *P-I-V* characteristics were measured at a controlled heat-sink temperature of 25^{o}C with a Source Measure Unit (SMU, Keithley 238) together with a calibrated Ge photodiode.

4.3 Static current-voltage characteristics

Figure 4.2 shows the measured *P-I-V* characteristics. A well known procedure [Joyc 78] to analyze the *I-V* characteristic of a standard p-n junction with a series resistance is based on the plot of the derivative $I\,{}^{dV}/_{dI}$ vs. I, which can be described by (see Sec. 3.2):

$$I\frac{dV}{dI} = (R_d + R_{s0})\,I \tag{4.1}$$

where R_{s0} is the series resistance and R_d is the active region differential resistance given by:

$$R_d = \frac{mkT}{qI} \tag{4.2}$$

being m the junction ideality factor (typically between 1 and 2), k the Boltzmann

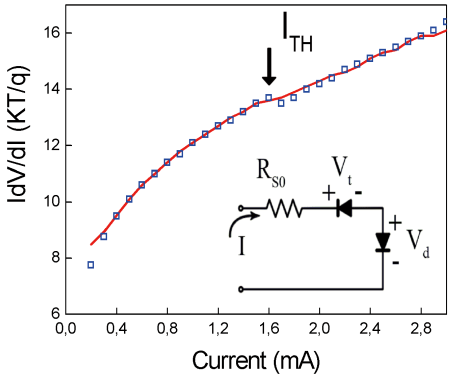

Figure 4.3: Comparison between measured (solid red line) and calculated (blue squares) $I\,^{dV}/_{dI}$ characteristics. The inset shows the DC equivalent circuit.

constant, T the absolute temperature, and q the electron charge. A linear fit of the measured $I\,^{dV}/_{dI}$ vs. I characteristic provides the values of R_{s0} and m from the slope and the intercept with the abscissa axis, respectively. Equations 4.1 and 4.2 are also valid for a laser diode below threshold, but above threshold the clamping of the Fermi levels caused by the stimulated emission makes zero the differential resistance in the right hand side of Eq. 4.1. In consequence, the $I\,^{dV}/_{dI}$ vs. I characteristic shows a clear downwards step at threshold [Paol 76, Joyc 78].

The measured $I\,^{dV}/_{dI}$ characteristic is shown in Fig. 4.3 with solid red line. The results in Figs. 4.2 and 4.3 show two non-conventional features:

- The value of m as obtained by the extrapolation of Eq. 4.1 towards zero is very high, between 7 and 10 depending on the current range; additionally the I-V characteristics are clearly non-linear both below and above threshold.
- There is not a clear step at threshold, although some signature of threshold is still apparent from the slope change around threshold in the measured $I\,dV/dI$ curve in Fig. 4.3.

The high value of the apparent ideality factor is attributed to the voltage drop in the TJ, V_t, which depends non-linearly on the current. This voltage drop can be related with the current by [Dema 70, Meht 06]:

$$I = I_p \frac{V_t}{V_p} \exp\left(1 + \frac{V_t}{V_p}\right) \tag{4.3}$$

where V_p and I_p are the forward peak voltage and current of the TJ, respectively.

m	$R_{s0}(\Omega)$	$I_S(nA)$	$V_p(mV)$	$I_p(\mu A)$	R_d @ I_{TH} (Ω)	R_t @ I_{TH} (Ω)
2	41.1	0.003	382	73.1	32.1	147.1
2.8	40.0	0.39	365	93.7	45.0	135.4
5	31.7	97	356	242	80.3	108.2

Table 4.1: Electrical parameters extracted from the fit of the *I-V* characteristic and differential active layer and TJ resistances at threshold.

The differential tunnel resistance R_t is obtained from Eq. 4.3 as:

$$R_t = \frac{dV_t}{dI} = \frac{V_t}{1+\left(\frac{V_t}{V_p}\right)}\frac{1}{I} \tag{4.4}$$

Then the *I-V* characteristics of the device can be modeled by the DC equivalent circuit shown in the inset of Fig. 4.3, and the total applied voltage can be written as $V = I\,R_S + V_t + V_d$, where V_d is the voltage drop in the active region, which can be approximated as $V_d \approx \frac{mkT}{q}\ln\left(\frac{I}{I_S}\right)$, with I_s being the p-n junction saturation current.

The experimental *I-V* and $I\,dV/dI$ characteristics below threshold were fitted to Eqs. 4.1 - 4.4, using R_{s0}, m, I_s, I_p, and V_p as fitting parameters. Different combinations of the fitting parameters provided a good agreement between calculations and experiments, and values of the ideality factor ranging between 1 and 5 could be obtained.

The values of the fitting parameters and the active region and tunneling differential resistances at threshold are summarized in Tab. 4.1 for different values of diode ideality factor: i) $m = 2$, the typical value in laser diodes [Paol 76, Joyc 78], ii) $m = 2.8$, the value reported for similar InAlGaAs QWs [Yang 09], and iii) $m = 5$, the value which provides the best fit. As no remarkable differences are observed between the quality of the fitting in the three former cases, in the following $m = 2.8$ is considered, which is the value measured for similar material [Yang 09].

The calculated and measured *I-V* characteristic are compared in Fig. 4.2, showing a very good agreement. For the selected value of m, the contribution of the TJ, active region and series resistance to the total differential resistance are plotted in Fig. 4.4. At threshold, the total differential resistance of the device is rather high, around 200 Ω, and the contribution of TJ, series resistance and active region are 60%, 20% and 20%, respectively. The high voltage drop at the TJ explains the high value of the apparent m when the *I-V* characteristic is analyzed considering only a p-n diode with series resistance.

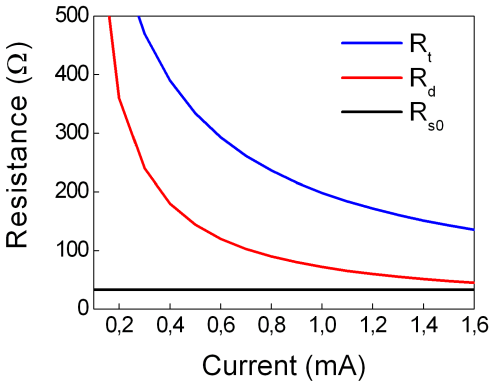

Figure 4.4: Calculated differential resistances of the TJ (blue) and active layer (red) as a function of the current in comparison with the DC series resistance (black).

The second non-conventional feature in the measured $I\,dV/dI$ characteristic, the small step at threshold, has been previously reported in other types of laser diodes and attributed to different physical processes. Esquivias *et al.* [Esqu 99] measured the electrical impedance of InGaAs/GaAs QW lasers and analyzed the results considering the dynamic interaction between the three-dimensional carriers in the confinement layer and the two-dimensional carriers in the QWs. They observed the reduction or the absence of step in the differential resistance at threshold for some particular devices, which was interpreted as a consequence of the absence of clamping in the 3D carrier density caused by the carrier capture bottleneck together with a low re-emission rate from the QWs to the confinement region. Following ref. [Esqu 99], the active layer differential resistance above threshold is expressed as:

$$R_d = \frac{\frac{mkT}{q}}{\left(I + \frac{\tau_{\delta n}}{\tau_{esc}} I_{TH}\right)} \tag{4.5}$$

with $\tau_{\delta n}$ and τ_{esc} being the differential carrier lifetime and the escape time, presented in Chapter 3. Equation 4.5 indicates that the step at threshold depends on the ratio between $\tau_{\delta n}$ and τ_{esc}: when τ_{esc} is much lower than $\tau_{\delta n}$ the differential resistance drops to zero, as it is usually observed in bulk and QW lasers, but when τ_{esc} is much larger than $\tau_{\delta n}$ there is no step at threshold in the $I\,dV/dI$ characteristic. When $\tau_{\delta n}$ and τ_{esc} are comparable, the height of the step at threshold can be used to estimate the ratio between the two time constants [Weis 94a].

Eliseev *et al.* [Elis 05] also reported the absence of step at threshold, and even the existence of an upwards step, in GaAs based laser diodes. They attributed this behavior to injection induced conductivity. In the InAlGaAs QW lasers considered

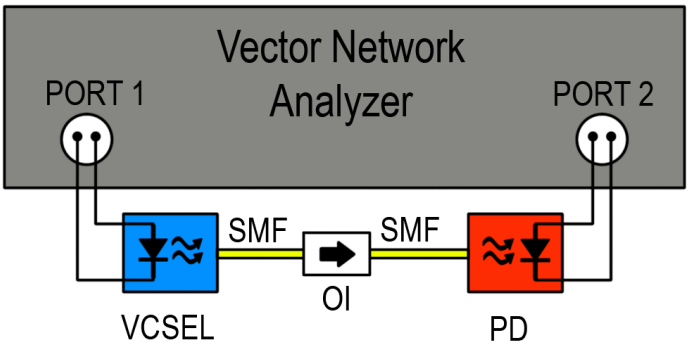

Figure 4.5: Set-up for the measurement of the S-parameters. An optical isolator (OI), a photodiode (PD) and two standard Single Mode Fiber (SMF) pathcords are used in the measurement of S_{21}.

here, the high electron barrier expected in this material system suggests a more likely interpretation based on the low re-emission of carriers from the QWs to the barriers. In fact, Yang [Yang 09] measured escape times ranging between 2.5 and 12 ns for InGaAlAs 1.5 μm laser diodes together with a behavior of the electrical impedance consistent with the carrier capture/escape model. In the reported experiments, the interpretation of the $I\,dV/dI$ characteristic based on the dynamic processes is also consistent with the results on the high frequency impedance measurements reported in next section. Using Eqs. 4.2 and 4.5 and considering $m = 2.8$, the estimated value of the ratio $\tau_{esc}/\tau_{\delta n}$ is 4.3.

The $I\,dV/dI$ characteristics below and above threshold were calculated using Eqs. 4.2-4.5 and the parameters obtained after the fitting procedure described above. They are compared in Fig. 4.3 with the experimental results, showing an excellent agreement.

4.4 Electrical impedance below threshold

The scattering parameters (S-parameters) were measured with a Vector Network Analyzer (VNA, Agilent E8363B). The small sinusoidal signal (-30 dBm) from the VNA is superposed to the DC current from the SMU through a bias-tee and swept from 0 to 10 GHz. The real and imaginary parts of the S_{11} parameter are directly measured at the VNA, for each selected bias current. For the measurement of the S_{21} parameter, which is presented further in this Chapter, a fast photodiode (40 GHz) is used together with an optical isolator, for avoiding back reflections, and two fiber patchcords, as shown in Fig. 4.5.

The external leads of the TO-packaged device were shortened and they were

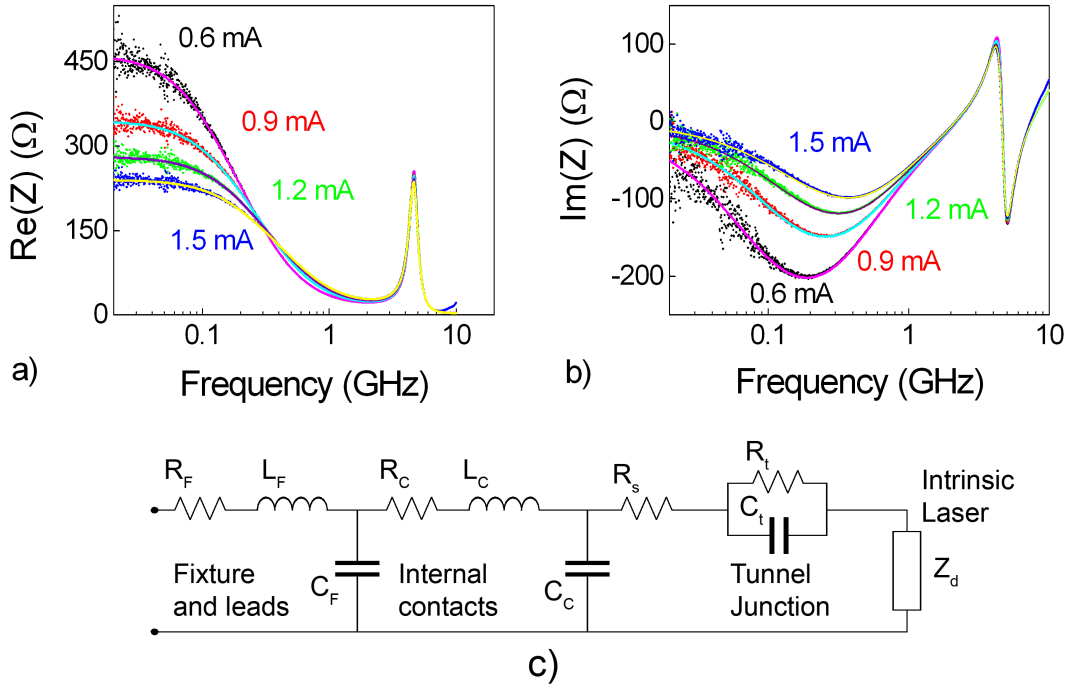

Figure 4.6: Real (a) and imaginary (b) part of the electrical impedance at different bias current below threshold: measurements (dots) and fitting to Eq. 4.6 (lines). Small signal equivalent circuit (c).

directly connected to Port 1, with the VCSEL anode inserted into the central pin of the SMA connector, and the VCSEL cathode in contact with the SMA receptacle. The calibration plane was placed at the end of the SMA connector. The device used in the measurements reported in this Chapter has a threshold current (I_{TH}) of 1.6 mA and central wavelength of 1555.38 nm at 4 mA.

Figure 4.6 (a)-(b) show the real and imaginary parts of the subthreshold impedance for different injection levels, as extracted from the reflection coefficient S_{11}. The measured laser impedance was modeled with the equivalent circuit shown in Fig. 4.6 c). This equivalent circuit is based on the device structure and it includes a simplified version of the circuit model for the electrical parasitics of a TO-type package [Chen 07].

The equivalent circuit includes four main parts: fixture and TO-header parasitics, chip parasitics, TJ and active region. The fixture and TO-header parasitics are modeled with a series resistance R_F, a series inductanceL_F and a parallel capacitance C_F arising from the connection between the SMA connector and the leads of the TO-56 mount. The chip parasitics are modeled through a series resistance R_C and a series inductance L_C, due to the internal bonding wire contacts, and a parallel capacitance C_C accounting for the distributed capacitance between the

$R_s(\Omega)$	$L_F(nH)$	$L_C(nH)$	$C_F(pF)$	$C_C(pF)$	$R_F(\Omega)$	$R_C(\Omega)$
32.8	1.23	3.2	0.52	1.14	2.4	14.4

Table 4.2: Extracted bias independent element values of the equivalent circuit.

chip contacts. The semiconductor layers are modeled by the series combination of a resistance R_s, which includes the resistance of semiconductor layers and metal-semiconductor interfaces, the TJ and the active region. The TJ is considered as the parallel combination of the tunnel resistance R_t and tunnel capacitance C_t. The active region is modeled considering capture/escape effects according to [Esqu 99]:

$$Z_d(\omega) = R_d \frac{1 + j\omega \left(\tau_{esc}^{-1} + \tau_{\delta n}^{-1}\right)^{-1}}{1 - \omega^2 \tau_0 \tau_{\delta n} + j\omega \left(\tau_0 + \tau_{\delta n} + \tau_0 \tau_{\delta n} \tau_{esc}^{-1}\right)} \tag{4.6}$$

where R_d is the below threshold active layer differential resistance, and τ_0 is an additional time constant which includes contributions arising from τ_{cap}, the carrier capture time, and from the time constant associated to the space charge region.

The measured impedance (real and imaginary parts) was fitted to the theoretical expression of the equivalent circuit in Fig. 4.6 c), for bias currents between 0.4 mA and 1.6 mA (step 0.1 mA) at frequencies ranging between 20 MHz and 8 GHz. Only four curves in the measured current range are shown for clarity in Fig.4.6 a) and b). In order to decrease the number of fit parameters, the diode differential resistance $R_d(I)$ and tunnel resistance $R_t(I)$ were calculated from the analysis of the static I-V measurements, using Eqs. 4.2 and 4.5. In the fit procedure, the electrical parasitics R_F, L_F, C_F, R_C, L_C, C_C and R_s were considered independent of the bias, while the TJ capacitance C_t and the dynamic time constants τ_{esc}, $\tau_{\delta n}$ and τ_0 were considered bias dependent. In the fit process, the total error, considering the complete set of bias and frequencies, was minimized.

The results of the simulated impedance after the fitting procedure are compared with the experimental characteristics in Fig. 4.6 a) and b), showing a very good agreement up to 8 GHz and a small deviation above this frequency. The extracted bias independent circuit elements are summarized in Tab. 4.2, and the evolution of the bias dependent parameters are plotted in Fig 4.7.

The bias independent peak in the impedance at about 5 GHz is caused by the fixture and chip electrical parasitics L_F, C_F, L_F, and C_C. Two different inductances and capacitances, as shown in the equivalent circuit, must be introduced in order to reproduce the high frequency peak in the impedance, as a single inductance/capacitance combination did not provide good fitting quality. The values of

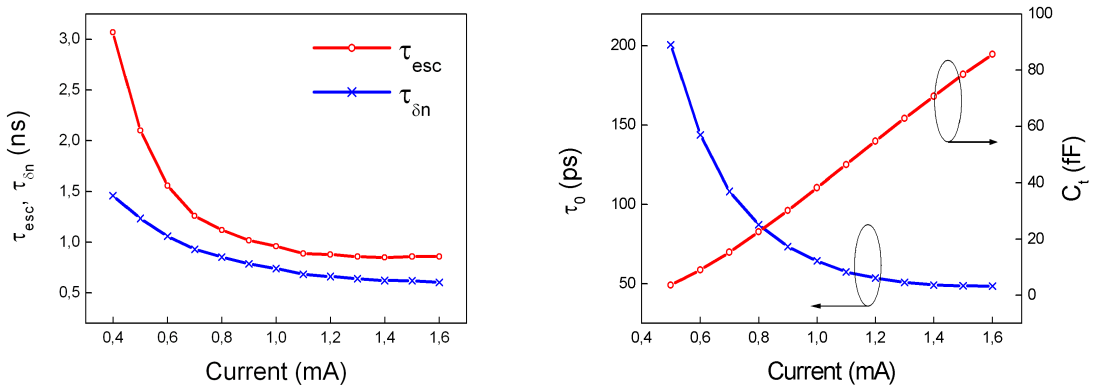

Figure 4.7: Extracted differential carrier lifetime $\tau_{\delta n}$ and escape time τ_{esc} as a function of current (left) and extracted values of the TJ capacitance C_t and time constant τ_0 as a function of current (right).

the parasitic elements are comparable to those previously extracted in similar VCSELs, indicating that the proposed modeling of access parasitics is appropriate for packaged VCSELs. The total series resistance ($R_F + R_C + R_s$) extracted from the high frequency measurements was slightly higher than the series resistance R_{s0} extracted from the static I-V characteristics, probably as a consequence of the different electrical access in the high frequency and DC set-ups.

The tunnel capacitance C_t increases with the bias while the dynamic time constants τ_{esc}, $\tau_{\delta n}$ and τ_0 decrease (see Fig. 4.7). The escape time ranges between 3 ns and 1 ns, indicating a low carrier re-emission as expected from the high electron barrier in this material system, and in agreement with the reported values in similar QWs [Yang 09]. The decrease of the escape time with bias is a consequence of the state filling effect which enhances the carrier re-emission. The same trend in the escape time has been reported in InGaAs/GaAs QW lasers [Rome 00]. The ratio $\tau_{esc}/\tau_{\delta n} \approx 1.5$ is lower than the value extracted from the DC measurements but still indicating the correct interpretation of the step in the $I\,dV/dI$ characteristics. The time constant τ_0 ranges between 200 ps and 50 ps, and it is interpreted as arising from the capture time τ_{cap} and from the space charge layer capacitance of the active junction C_{sc} [Esqu 99]:

$$\tau_0 = \tau_{cap} + \frac{\tau_{esc}}{\tau_{esc} + \tau_{\delta n}} R_d C_{sc} \tag{4.7}$$

The decrease of τ_0 with the current is a consequence of the inverse proportionality of R_d with the current, and it is similar to that found in nominally undoped InGaAs/GaAs lasers [Esqu 99].

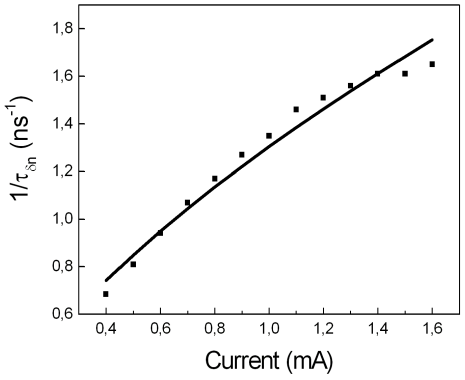

Figure 4.8: Inverse differential carrier lifetime and best fit to Eqs. 4.8 and 4.9

The dependence of the extracted differential carrier lifetime $\tau_{\delta n}$ on the bias current was used to estimate the recombination coefficients by the standard fitting procedure [Minc 99] to the expression:

$$\frac{1}{\tau_{\delta n}} = \frac{\partial R(N)}{\partial N} = A + 2BN + 3CN^2 \tag{4.8}$$

where A, B and C are the non-radiative, radiative and Auger recombination coefficients, respectively, N is the carrier density and *R(N)* the total recombination rate. Assuming an injection efficiency of 100%, *R(N)* is related to the current by:

$$\frac{I}{qV_{act}} = AN + BN^2 + CN^3 \tag{4.9}$$

Figure 4.8 shows $\tau_{\delta n}^{-1}$ vs. I and the results of the best fit to Eqs. 4.8 and 4.9. The extracted recombination coefficients are summarized in Tab. 4.3, in comparison with other results reported in the literature for QW devices based on InAlGaAs/InP material. As it is well known, there is a high uncertainty in the values of the recombination coefficients due to differences in the active layers and operating point, the method of extraction, and also to the simplicity of Eq. 4.9. In this context, the values obtained here are reasonable, confirming the validity of the considered approach.

It is important to remark that the quality of the fitting of the calculated impedance to the experiments was also good when considering as input the values of $R_d(I)$ and $R_t(I)$ obtained from the analysis of the *I-V* using a different diode ideality factor m. In these cases the extracted parasitics elements were similar to those found for $m = 2.8$ and the dynamic time constants showed the same trend with the current with values only slightly different to those previously reported.

Ref.	This thesis	[Minc 99]	[Houl 05]	[Yang 09]
No. QW's	7	5	6	2
Wavelength	$\sim 1.5\,\mu m$	$\sim 1.5\,\mu m$	$\sim 1.3\,\mu m$	$\sim 1.5\,\mu m$
A (s^{-1})	$2.1{\cdot}10^{7}$	$7{\cdot}10^{7}$	$2.5{\cdot}10^{8}$	$4.5{\cdot}10^{7}$
B (cm^3s^{-1})	$0.9{\cdot}10^{-10}$	$1.5{\cdot}10^{-10}$	$4{\cdot}10^{-10}$	$1{\cdot}10^{-10}$ (guess)
C (cm^6s^{-1})	$1.6{\cdot}10^{-29}$	$1.4{\cdot}10^{-28}$	$5{\cdot}10^{-28}$	$1.9{\cdot}10^{-29}$

Table 4.3: Comparison between the extracted recombination coefficients of strained InAlGaAs QWs and previously reported values.

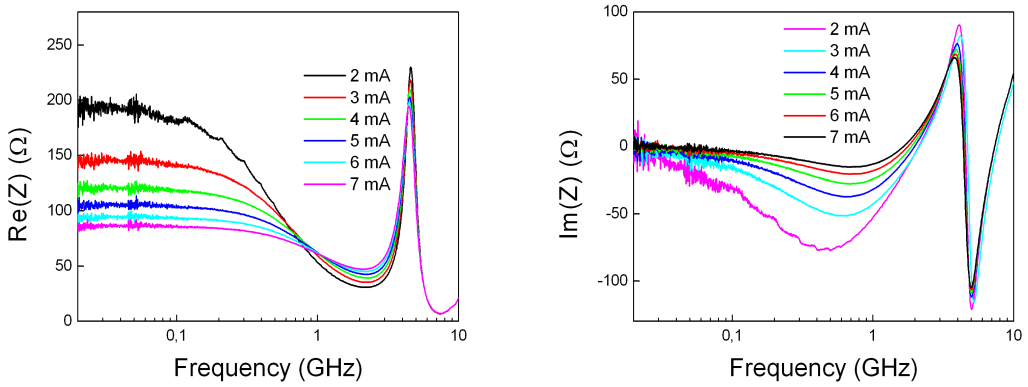

Figure 4.9: Measured real (left) and imaginary (right) electrical impedance at different bias current above threshold.

4.5 Electrical impedance above threshold

Figure 4.9 shows the measured real and imaginary parts of the impedance at different bias above threshold. It can be clearly observed that there is not a discontinuity of the low frequency magnitude of the impedance at threshold, consistently with the DC *I-V* results. The low-frequency impedance takes a high value (250 Ω – 80 Ω) and varies strongly with the bias current, contrary to the behavior of standard laser diodes for which the input impedance takes a low fixed value corresponding to the series resistance. These features are very important for the proper design of the electronic driver in direct modulation.

The analysis of the intrinsic impedance of a semiconductor laser predicts a peak at the relaxation frequency [Mori 79, Kan 92], which has been experimentally observed in different devices [Weis 94a, Hard 90]. The absence of such a peak has been related with carrier capture/escape effects [Esqu 99]. As it can be observed in Fig. 4.9, the measured impedance shows a high frequency peak corresponding

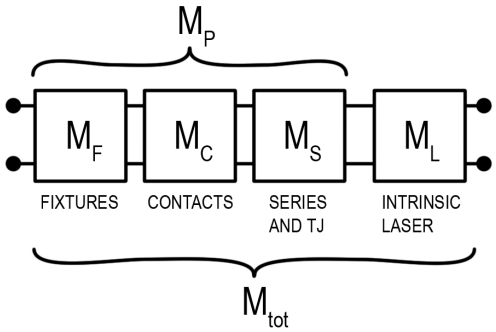

Figure 4.10: Schematic diagram of the laser and electrical access through the transfer matrix formalism.

to the fixture and chip parasitics, but it does not show a peak at the relaxation frequency, which takes values between 1 and 3 GHz as determined by independent modulation response measurements, as illustrated in the next Section. This fact confirms again the interpretation of the electrical characteristics of these devices as a consequence of the reduced re-emission of the QW carriers to the barrier layer ($\tau_{esc}/\tau_{\delta n} > 1$), similarly to the behavior observed in p-doped InGaAs/GaAs lasers [Esqu 99, Weis 94b]. The theoretical electrical impedance above threshold considering carrier capture/escape effects is described by the equivalent circuit in Fig. 4.6 but replacing Z_d in Eq. 4.6 by the corresponding expression for the active layer impedance above threshold [Esqu 99].

4.6 Modulation response and parameter extraction

The effect of electrical access and chip parasitics has to be considered for the calculation of the modulation response (MR) of the laser. The equivalent circuit of Fig. 4.6 is used to extract the VCSEL MR from the measured S_{21} parameter, taking into account the contribution of fixture and leads, chip contacts and TJ. The S_{21} parameter has been measured with the set-up shown in Fig. 4.5. The laser is fed with different values of the bias current from 2 mA to 7 mA and a superposed sinusoidal signal (-30 dBm). The S_{21} parameter is measured between 0 and 10 GHz.

The contribution of the electrical access and chip contacts, is considered following a transfer matrix approach, similar to the one described in [Baco 09]. The whole system under measure is divided in two sub-systems: one representing the parasitics, due to electrical access, contacts and TJ, and the other representing the VCSEL optical cavity. Each subsystem is represented with an ABCD parameter matrix, which offers a more convenient description with respect to S-matrix because it allows the representation of cascaded sub systems through matrix multiplication. The

complete system, including parasitics and laser cavity, is represented with the ABCD matrix product schematically shown in Fig. 4.10, which is equal to $M_{tot} = M_P \times M_L$, where M_{tot} is the ABCD matrix describing the whole system, M_P is the ABCD matrix associated with the electrical parasitics, M_L is the ABCD matrix associated with the laser optical cavity and $\times$ is the matrix cross product. Consequently, the intrinsic laser parameters of the laser can be obtained from $M_L = M_P^{-1} M_{tot}$, if M_P is known.

The ABCD matrix M_P is obtained directly from the equivalent circuit in Fig. 4.6, as the product $M_P = M_S \times M_C \times M_F$, where M_S, M_C and M_F are the ABCD matrices of the series impedance circuits, the chip contacts and the fixture and leads section, respectively. Those matrices are obtained directly from the equivalent circuit in Fig. 4.6, using the definition of ABCD parameters:

$$M_F = \begin{pmatrix} 1 + j\omega C_F \left(R_F + j\omega L_F\right) & R_F + j\omega L_F \\ j\omega C_F & 1 \end{pmatrix} \tag{4.10}$$

$$M_C = \begin{pmatrix} 1 + j\omega C_C \left(R_C + j\omega L_C\right) & R_C + j\omega L_C \\ j\omega C_C & 1 \end{pmatrix} \tag{4.11}$$

$$M_S = \begin{pmatrix} 1 & R_s + \frac{R_t}{1 + j\omega R_t C_t} \\ 0 & 1 \end{pmatrix} \tag{4.12}$$

Once the S-parameters matrix of the complete system is measured with the VNA, the electrical parasitics are corrected following these three steps : (i) conversion from S-parameters to ABCD parameter of the whole measured system M_{tot}, (ii) calculation of the laser intrinsic ABCD parameters using $M_L = M_P^{-1} M_{tot}$ and (iii) conversion to S-parameters of M_L for obtaining the corrected S_{21} of the VCSEL.

The conversion formulas from S-parameters to ABCD-parameters and *viceversa* are given in the following expressions [Ghos 10].

From S to ABCD:

$$A = \frac{(1 + S_{11})(1 - S_{22}) + S_{12}S_{21}}{2S_{21}} \tag{4.13}$$

$$B = Z_0 \frac{(1 + S_{11})(1 + S_{22}) - S_{12}S_{21}}{2S_{21}} \tag{4.14}$$

$$C = \frac{1}{Z_0} \frac{(1 - S_{11})(1 - S_{22}) - S_{12}S_{21}}{2S_{21}} \tag{4.15}$$

$$D = \frac{(1 - S_{11})(1 + S_{22}) + S_{12}S_{21}}{2S_{21}} \tag{4.16}$$

From ABCD to S:

$$S_{11} = \frac{A + {}^{B}/_{Z_0} - CZ_0 - D}{A + {}^{B}/_{Z_0} + CZ_0 + D} \tag{4.17}$$

$$S_{12} = \frac{2\,(AD - BC)}{A + {}^{B}/_{Z_0} + CZ_0 + D} \tag{4.18}$$

$$S_{21} = \frac{2}{A + {}^{B}/_{Z_0} + CZ_0 + D} \tag{4.19}$$

$$S_{22} = \frac{-A + {}^{B}/_{Z_0} - CZ_0 + D}{A + {}^{B}/_{Z_0} + CZ_0 + D} \tag{4.20}$$

where Z_0 is the characteristic impedance of the VNA.

The directly measured S_{21}, usually considered the as-measured MR, is shown in Fig. 4.11 (left) and the MR corrected following the above described procedure is shown in Fig.4.11 (right, with thin lines). The main differences between uncorrected and corrected MRs are the height of the peak, higher in the corrected MR, and the slope of the response at high frequencies, with a higher slope in the corrected MR. The corrected MRs were fitted to the theoretical MR of a QW laser, given in Eq. 3.53, which considers the standard response of a bulk laser (relaxation frequency and damping) and an additional pole at τ_0 accounting for the carrier capture time and the space-charge capacitance time constant.

The fitting results are also shown on the right graph of Fig. 4.11 (thick lines). The theoretical MR fits well to the corrected experimental MR at low frequencies and at the peak, but at high frequencies the corrected MR drops faster than the theoretical MR. This fact could indicate an over correction of the MR at high frequencies caused by the uncertainty of the circuit elements used in the correction procedure.

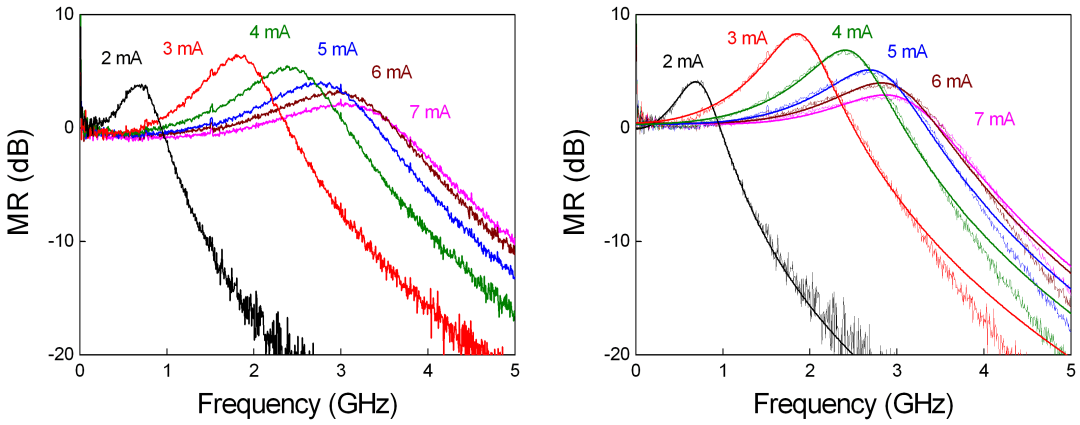

Figure 4.11: Modulation response for different bias currents: uncorrected (left graph) and corrected and fitted to Eq. 3.53 (right graph, thin and thick solid lines, respectively).

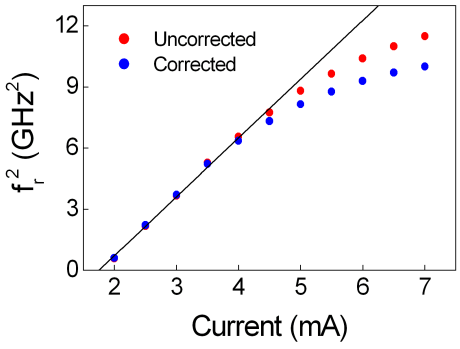

Figure 4.12: Squared resonance frequency as a function of applied current for uncorrected (red dots) and corrected (blue dots) data.

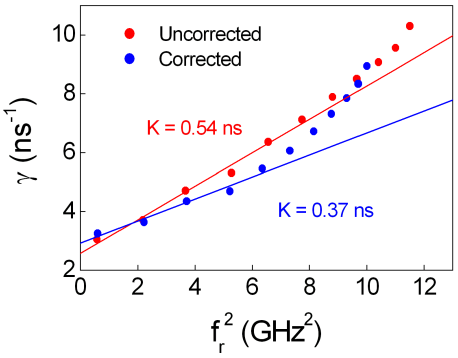

Figure 4.13: Damping factor versus squared resonance frequency for uncorrected (red dots) and corrected (blue dots) data.

The resonance frequency f_r, damping γ and additional pole τ_0 were obtained as a function of the applied current from fitting of the corrected MR to Eq. 3.53. Figure 4.12 shows the dependence of the squared resonance frequency on injected current, comparing the uncorrected and corrected extracted values. The squared resonance frequency shows the linear behavior with the current predicted by Eq. 3.25 up to around 5 mA, without important differences caused by the parasitics correction. Above this bias, thermal effects become relevant, as the temperature of active region increases above 40º (see Section 5.2), and the slope of the plot decreases, showing some differences between uncorrected and corrected results. The differential gain $^{dG}/_{dN}$ can be extracted from the linear part of the plot making use of Eq. 3.25, yielding a value of $1.2{\cdot}10^{-16}$ cm^2. This value is low in comparison with the best values reported in EE lasers at ~1.55 µm, which reach up to 1.3-1.5 10^{-15}cm^2 [Mats 98].

Table 4.6 compares the value of $^{dG}/_{dN}$ obtained in this work, as well as other dynamic internal parameters which will be commented later, with reported values on 1.55 µm EE lasers based in InGaAlAs, either in the barrier or in the QW and barrier. Reported values for 1.3 µm VCSEL are also included for completeness. We have not found in literature reported values for neither EE lasers at 1.55 µm based on the same active layer material than the commercial VCSEL analyzed here (Strain Compensated, *SC*, InGaAlAs) nor for any VCSEL emitting at 1.5 µm. It is well known that the differential gain depends on the band structure of the active layer and on the injected carrier density [Cold 95]. The value obtained here is similar to that predicted for Lattice Matched (LM) InGaAs QW with InGaAsP barriers at high injection [Cold 95], but lower than those values reported in EE lasers (see

Table 4.6), possibly due to the high carrier injection typical of VCSEL.

The transparency current density can be extracted from the threshold carrier density, estimated from the results of the impedance characterization, and the extracted differential gain, yielding a value $N_{TR} \sim 1.2{\cdot}10^{18}$ cm^{-3}, a reasonable value for this type of active region [Cold 95].

The maximum 3 dB modulation bandwidth, f_{3dB}, measured in the devices is 4.1 GHz at 7 mA (see Fig. 4.11). Although much lower than best reported values in unpackaged 1.55 µm VCSELs (greater than 15 GHz, see reference [Mull 09]), this is a very good performance for a packaged devices nominally scheduled for 2.5 Gbps.

Figure 4.13 shows the dependence of the damping as a function of squared resonance frequency, comparing the uncorrected and corrected extracted values. The linear dependence predicted by Eq. 3.25 is obtained up to around 5 mA, similarly to the behavior of the resonance frequency, as at higher bias thermal effects become relevant. In this case the effect of parasitic corrections affects the extraction of the K-factor, defined as the slope in Fig. 4.13, yielding 0.54 ns and 0.37 ns before and after correction. The measured K-factor is similar to other values reported in literature for InGaAlAs based lasers (see Table 4.6), and provides a maximum intrinsic modulation bandwidth of 23.7 GHz.

Making use of Eq. 3.24, the gain compression factor is found to be $0.45{\cdot}10^{-17}$ cm^3, a small value in comparison with other devices (see Table 4.6), consistently with the low value of $^{dG}/_{dN}$, and attributed again to the high carrier injection conditions of the device under characterization.

4.7 Summary of VCSEL parameters

The full list of VCSEL parameters are summarized in Tab. 4.4-4.6. This set of parameters can be useful for detailed device modeling, for the design of the driving electronics and for the simulation of a full optical communication link in which the 1.55 µm TJ based VCSEL is used as an emitter.

Symbol	Parameter	Value
R_1	Top mirror reflectivity	99.9%
R_2	Bottom mirror reflectivity	99.5%
n	Refractive index	3.2
L	Optical cavity length	3.15 µm
r	Active region radius	4.5 µm
L_{QW}	Single QW length	7 nm
N_{QW}	Number of QW's	7
L_{AR}	Active region length	49 nm
Γ_l	Longitudinal confinement factor	0.05
Γ_{tr}	Transverse confinement factor	1

Table 4.4: VCSEL structure parameters obtained from [Park 06] and [Rayc 09].

Symbol	Parameter	Value
A	Non-radiative recombination coefficient	$2.1{\cdot}10^{7}$ s^{-1}
B	Radiative recombination coefficient	$0.9{\cdot}10^{-10}$ cm^3s^{-1}
C	Auger recombination coefficient	$1.6{\cdot}10^{-29}$ cm^6s^{-1}
$\tau_N(I_{TH})$	Carrier lifetime at threshold	1.36 ns
N_{TR}	Transparency carrier density	$3.14{\cdot}10^{18}$ cm^{-3}
N_{TH}	Threshold carrier density	$4.36{\cdot}10^{18}$ cm^{-3}
τ_P	Photon lifetime	5.6 ps
$\tau_{\delta n}(I_{TH})$	Differential carrier lifetime at threshold	0.34 ns
$\tau_{esc}(I_{TH})$	Carrier escape time at threshold	0.86 ns
$\tau_0(I_{TH})$	Single RC pole at threshold	48 ps
dG/dN	Differential gain	$1.22{\cdot}10^{-16}$ cm^2
K	K-factor	0.37 ns
ε	Gain compression factor	$9.71{\cdot}10^{-18}$ cm^3

Table 4.5: Extracted VCSEL parameters from static and high frequency measurements.

Reference	Cavity	QW material	Barrier material	Strain	$^{dG}/_{dN}$ $(10^{-16}cm^2)$	ϵ $(10^{-17}cm^3)$	K (ns)
[Grab 91]	FP	InGaAs	InGaAlAs	LM	3.2	0.5	0.2
[Shim 95]	FP	InGaAs	InGaAlAs	LM	1.9-2.8	-	-
[Shim 95]	FP	InGaAs	InGaAlAs	SL	4.6-9.3	-	-
[Mats 98]	FP	InGaAsP	InGaAlAs	SC	13-15	1.6-4.5	0.135-0.15
[Liu 01]	FP	InGaAlAs	InGaAlAs	LM	6.9	13.4	0.96
[Liu 01]	FP	InGaAlAs	InGaAlAs	SL	9.2	7.7	0.46
[Baco 10]	VCSEL 1.3 µm	InGaAlAs	InGaAlAs	SC	4.8	2.09	0.41
This work	VCSEL 1.5 µm	InGaAlAs	InGaAlAs	SC	1.6	0.45	0.37

Table 4.6: Comparison of differential gain, gain compression factor and K-factor for lasers with different structure, active material and strain (Lattice Matched, LM, Strained Layer, SL, and Strain Compensated, SC).

4.8 Conclusions

The electrical properties of TJ based 1.5 μm VCSELs have been characterized and relevant information has been obtained on the intrinsic properties of packaged lasers after properly considering the fixture and mount electrical parasitics. An equivalent circuit is presented including parasitics, TJ and carrier capture/escape processes which present a very good agreement with the measurements. The VCSEL under study shows a very high input differential resistance above threshold, ranging between 200 Ω and 80 Ω, which depends strongly on the applied bias. This high input resistance is mainly attributed to the TJ.

The static and dynamic electrical measurements show the absence of voltage saturation at threshold, which is interpreted as arising from the interplay between three and two dimensional carriers, in QW's and core region, respectively. In particular, a value of the escape time higher than the carrier lifetime explains this behavior and it is confirmed by impedance measurements above threshold.

The analysis of the subthreshold electrical impedance considering carrier capture/escape effects provides a reasonable estimation of the escape time, the carrier lifetime, and of the A, B and C recombination coefficients.

The VCSEL MR has been measured and the effect of electrical parasitics associated with fixture, chip contacts and series resistance has been considered for the calculation of the intrinsic MR of the laser. A transfer matrix approach is used to correct the measured MR from the electrical parasitics. The dependency of resonance frequency and damping on applied bias is obtained from the corrected MR, allowing the calculation of the laser intrinsic parameters.

Chapter 5

Pulse generation from gain switched 1550 nm VCSELs

This Chapter reports the characterization of the optical pulses generated from a GS VCSEL emitting at 1550 nm. The gain switching technique is briefly described and previous results by other authors with both GS EE lasers and VCSEL are reviewed. The VCSEL used in the experiments is characterized under CW operation in terms of P-I-V curve, spectral features and thermal behavior. The VCSEL is GS with a sinusoidal current and the modulation parameters are varied in order to obtain the shortest pulses. The dependence of pulse duration, peak power, timing jitter and spectral bandwidth on the gain switching conditions is discussed. The shortest pulses obtained at different repetition rates are finally summarized.

5.1 Introduction

The gain switching technique is based on the excitation of the first spike of the relaxation oscillations at the laser turn-on when the laser is directly modulated and biased below threshold. In Chapter 3, the large signal modulation of a laser diode has been introduced and the gain switching technique has been described. Briefly, the main advantages of the technique are its simple implementation and the possibility of tuning the pulse repetition rate. On the other hand, pulses from GS sources are highly chirped and are usually affected by a large amount of jitter.

Picosecond pulse generation from GS semiconductor lasers was firstly reported with AlGaAs based EE devices. The shortest pulse duration obtained at this wavelength is 4 ps at a repetition rate of only 10 MHz [Bimb 84], generated with an electrical pulse train at high injection level. More typical values at 850 nm are between 10-15 ps [Aspi 82, Elli 83] and 40 ps [Lin 80], with repetition rates up to 2.5 GHz [Auye 81]. Slightly longer durations are reported for InGaAsP EE lasers. The shortest pulse obtained at 1310 nm has a duration of 6.7 ps at a repetition rate of 100 MHz [Liu 89]. Around 1550 nm a pulse-width of 11 ps at repetition rate of 1 GHz has been obtained [Whit 85], more typical values are between 25 and 60 ps [Liu 81, Lin 85] and a repetition rate of 11.2 GHz has been reported [Lin 84b].

Due to the high negatively chirped character of pulses obtained with GS lasers (see Chapter 3 Sec. 3.4), pulse propagation through an optical fiber with positive dispersion and appropriate length allows pulse compression. With this technique, Nakazawa et al. [Naka 90] compressed a pulse train at 500 MHz with duration 25-30 ps down to subpicosend pulse width (180-250 fs), using a GS DFB laser emitting at 1550 nm and different stages of amplification. Around 1310 nm, pulses from a GS DFB lasers compressed to 2 ps have also been reported [Liu 91].

The shortest duration obtainable from GS lasers, without compression, is related to the modulation conditions and to the laser structure. Aspin et al. [Aspi 81] showed that a small cavity length shortens the minimum pulse duration as a consequence of the reduced photon lifetime. The advent of VCSELs, with typical cavity length in the order of a few micrometers, was then promising for the generation of very short pulses. A 4 ps pulse was obtained by Karin et al. [Kari 90] with a GaAs based VCSEL, optically GS with a dye laser pump. However, it was pointed out by other authors that such short duration were unfeasible in practical VCSELs using electrical excitation, due to the high reflectivity ($> 99\%$) of DBR mirrors introduced to obtain low threshold operation, which increases the photon lifetime [Hasn 92]. Typical pulse widths from 850 nm GS VCSELs are between 12 ps [Pepe 93a] and 28 ps [Lin 91] and repetition rates up to 8 GHz have been achieved [Wies 93]. A

very short pulse of only 3.4 ps has been obtained with fiber compression of a 14.6 ps pulse at 500 MHz [Pepe 94] and a pulse train at 10 GHz with compressed pulse duration of only 8.7 ps has been reported [Naka 07].

A few works report on pulse generation from GS VCSEL at different wavelength than around 850 nm, because of the realization of robust, reliable long wavelength VCSELs took place only in recent years, see Chap. 2. At 1.1 µm, pulses generated at a repetition rate of 10 GHz and with compressed width of 11.5 ps have been presented [Koiz 09]. At the communication relevant wavelength of 1550 nm, pulses with duration of 55 ps and repetition rates up to 3 GHz have been investigated in this work and pulse properties, i.e. peak amplitude, duration, jitter and spectral width, have been characterized as a function of the gain switching parameters *[Cons 08, Cons 10a]*.

5.2 CW VCSEL characterization

The laser used in the experiments is a commercial (Raycan), fiber pigtailed 1550 nm 2.5-Gb/s VCSEL, based on InAlGaAs MQWs active region, buried TJ, air-gap aperture, and InAlGaAs-InAlAs DBR mirrors [Park 06]. The device structure and details have been described in Chapter 4.

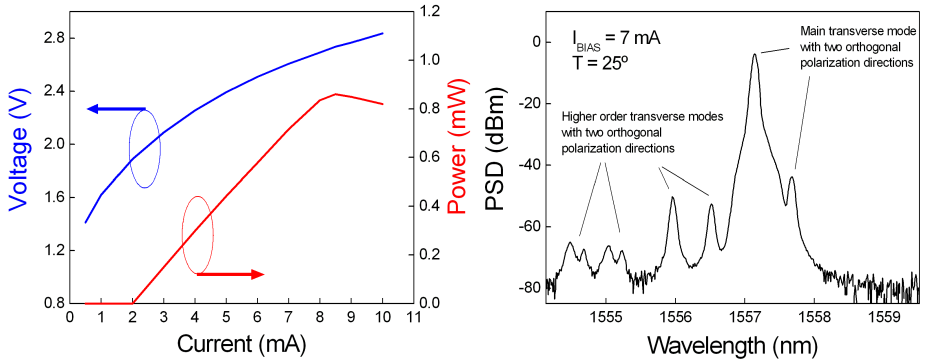

Figure 5.1: *P-I-V* curve (left) and emission spectrum for I_{BIAS} = 7 mA (right).

The experimental set-up for the CW characterization consist of a Source Measure Unit (SMU, Keithley 238), used as a current generator and voltmeter, a power meter, an Optical Spectrum Analyzer (OSA, Ando AQ-6315A) with spectral resolution of 0.05 nm, and a home made temperature control based on a Peltier cell in contact with the copper heat sink where the laser is mounted.

The *P-I-V* curve is measured between 0 and 10 mA, and the threshold current (I_{TH}) of the device is 2 mA at 25º C, as shown in Fig. 5.1 (left). The output power

of the device is limited by the thermal roll occurring at about 8 mA, reaching the maximum value of 0.8 mW in CW operation.

The spectrum of the VCSEL biased with 7 mA at 25º C is shown in Fig. 5.1 (right). The peaks in the spectrum are the multiple transverse mode excited, each with two orthogonal polarization directions. The stronger peak at 1557.2 nm corresponds to the dominant polarization of the fundamental transverse mode of the cavity. Spaced 0.5 nm (62.5 GHz) towards longer wavelength is the orthogonal polarization mode, suppressed of more than 35 dB with respect to the main peak over the whole current range. The wavelength spacing between the two polarization modes is due to the difference of the effective refraction index of the VCSEL cavity along each polarization axis, i.e. its birefringence, being a very high value with respect to the ones usually reported (1-10 GHz), see [Hend 97] and references therein.

Peaks at shorter wavelength correspond to the second and higher order transverse mode, also characterized by the two orthogonal polarizations. This has been checked with a rotatable linear polarizer, that has also been used to verify that no polarization switching occurs in the current range of operation.

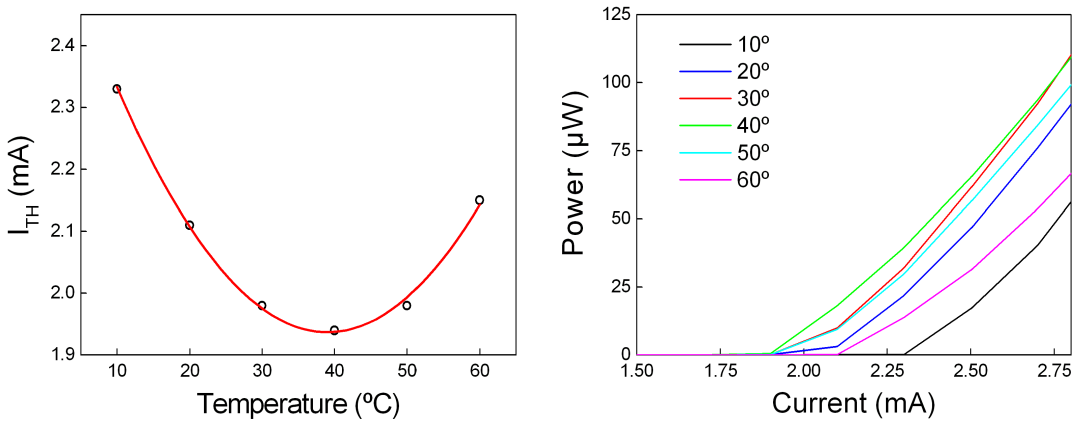

Figure 5.2: Threshold current versus temperature (left) and P-I curves near threshold at different temperatures (right).

The threshold current as a function of the heat sink temperature (T_{HS}) is shown in Fig. 5.2 (left). Between 10º and 60º, the variation of I_{TH} is about 300 µA, having its minimum of 1.93 mA value for $T_{HS} = 40$º C. The P-I curves at different temperatures are shown in Fig. 5.2 (right), with the applied current ranging from 1.5 mA to 2.8 mA.

The thermal impedance of the device, R_{TH}, has been calculated measuring the wavelength excursion of the laser as a function of temperature and dissipated power, following the method described in [Joyc 75, Mann 81]. R_{TH} is defined as the temperature variation of the device per dissipated power, $R_{TH} = \frac{\Delta T}{\Delta P_{diss}}$ [Joyc 75], and

the method used for its calculation consists of two sets of measurements: i) the wavelength peak is measured, when the laser is biased at a constant current and the temperature T_{HS} is varied, thus obtaining the gradient $\frac{\Delta\lambda}{\Delta T}\Big|_{I\,const}$; ii) the temperature T_{HS} is kept constant and the dissipated power is measured as a function of the applied current, obtaining $\frac{\Delta\lambda}{\Delta P_{diss}}\Big|_{T\,const}$ [Mann 81]. Finally, R_{TH} is calculated as $R_{TH} = \left(\frac{\Delta\lambda}{\Delta P_{diss}}\Big|_{T\,const}\right)\left(\frac{\Delta\lambda}{\Delta T}\Big|_{I\,const}\right)^{-1}$.

Figure 5.3 shows the results of the measurements used for the calculation of R_{TH}, which gives a value of 1608 K/W, slightly greater than the value measured from the manufacturer in unpackaged devices (about 1500 K/W) [Rayc 09].

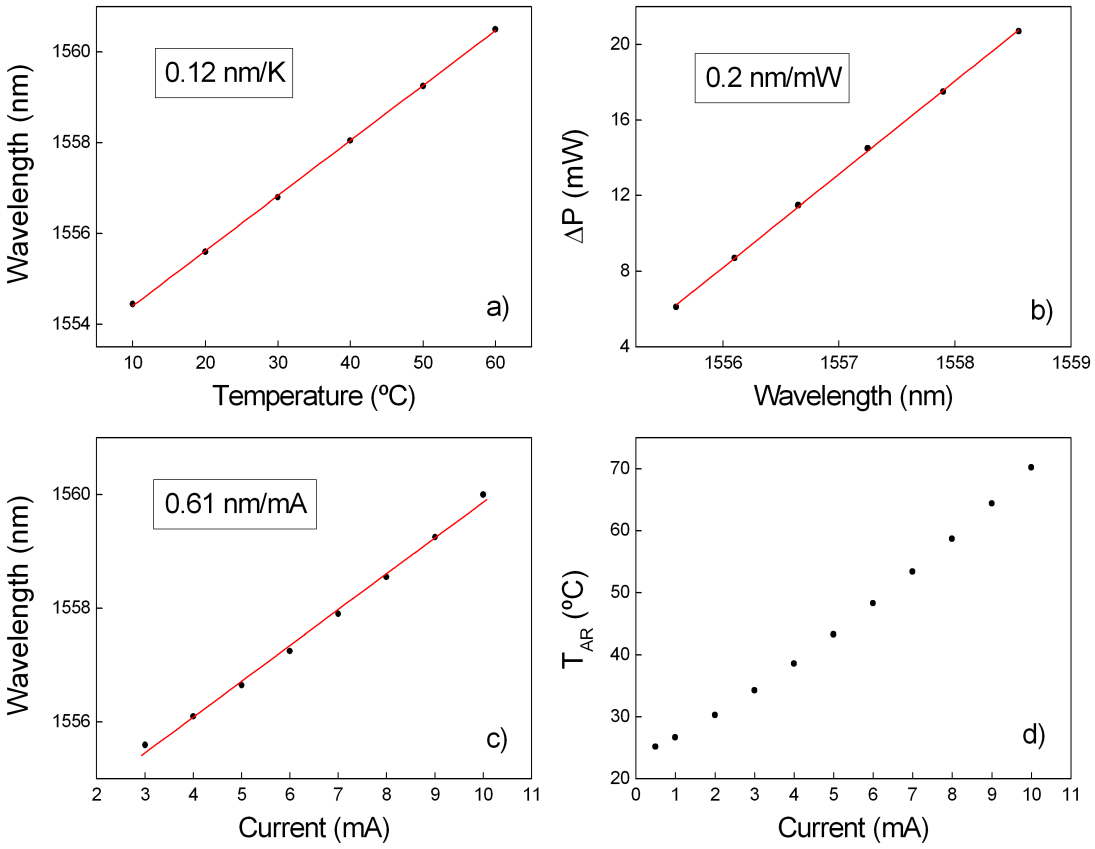

Figure 5.3: Calculation of R_{TH} : a) peak wavelength shift versus heat sink temperature at constant current, b) dissipated power as a function of peak wavelength varying I_{BIAS} at constant T_{HS}, c) peak wavelength shift versus applied current at constant T_{HS} and d) temperature of the active region as a function of applied current.

The temperature of the active region (T_{ACT}) has been calculated considering the electrical power dissipated in the device and the thermal impedance R_{TH}, as $T_{ACT} = T_{HS} + R_{TH}(P_{IN} - P_{OUT})$, where P_{IN} and P_{OUT} are the input electrical power, given by the product of the applied current and voltage, and the output

optical power, respectively.

The values of T_{ACT} obtained in the applied current range are shown in Fig. 5.3 d). The high increase of T_{ACT} with applied bias, about 5^{o}/mA above threshold, is a consequence of the Joule heating and of the high measured value of R_{TH}.

5.3 Dependence of the pulse properties on Gain-Switching conditions

The set-up for pulse generation from the GS VCSEL under study is shown in Fig. 5.4.

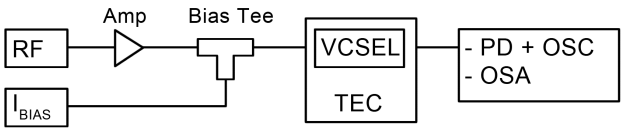

Figure 5.4: Set-up for pulse generation and characterization.

The VCSEL is fed through a bias-tee with a bias current I_{BIAS} and an amplified sinusoidal radio frequency (RF, Agilent 8648B) signal, with frequency f_{RF} and amplitude P_{RF}. The amplitude of the sinusoid is given in dBm, as the nominal output of the RF generator on a 50 Ω load. The laser heat-sink temperature is controlled by a Thermo Electrical Controller (TEC) based on a Peltier cell. The temporal evolution of the pulses are measured with a fast photodiode and oscilloscope (Tektronix CSA800, module 80C06-CR) and the pulse spectra are measured with the OSA.

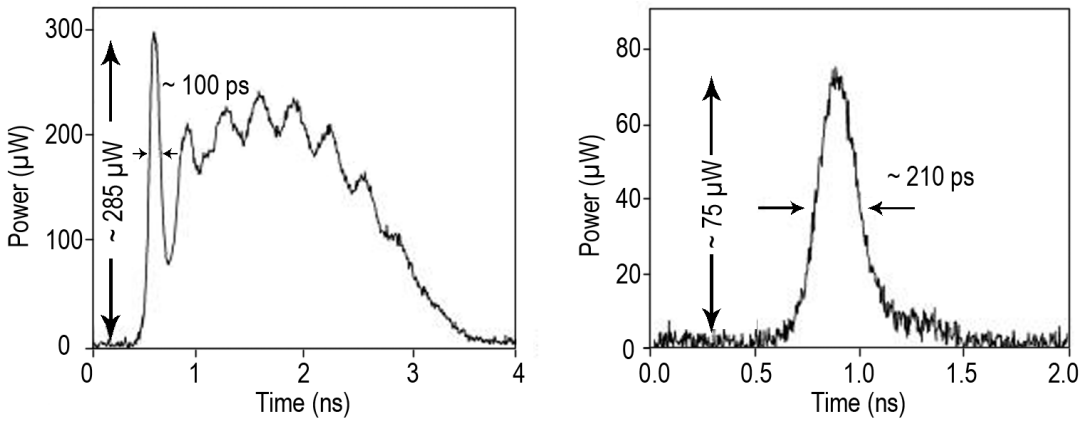

Figure 5.5: Relaxation oscillations observed with f_{RF} = 100 MHz, P_{RF} = 10.5 dBm for $I_{BIAS}/I_{TH} = 1$ (left) $I_{BIAS}/I_{TH} = 0.25$ (right).

The pulse intensies of the GS VCSEL for f_{RF}= 100 MHz and P_{RF} = 10.5 dBm,

with $I_{BIAS}/I_{TH} = 1$ and $I_{BIAS}/I_{TH} = 0.25$ are shown in Fig. 5.5, left and right, respectively. For $I_{BIAS}/I_{TH} = 1$, a strong initial peak followed by the relaxation oscillations, at a frequency of approximately 3.6 GHz, is observed. In these conditions the injected current overcomes the lasing threshold during a time large enough to excite more than one single spike. At a bias current much lower than threshold, $I_{BIAS}/I_{TH} = 0.25$, as shown in Fig. 5.5 (right), the maximum value of the injected current and the time interval in which current overcomes threshold are both reduced, resulting in the generation of a single pulse per period, corresponding to the first spike of relaxation oscillations. However, as the peak current is lower than in previous case, the relaxation frequency is lower and consequently the pulse is weaker and longer.

Figure 5.6 shows the peak power and pulse width of the first excited peak as a function of f_{RF} for different values of I_{BIAS}/I_{TH}. The relaxation oscillations are observed until a certain value of f_{RF} that depends on I_{BIAS}/I_{TH}. The increase of f_{RF} increases the amplitude and reduces the duration of the first spike, until a single pulse per period is generated. Further increase in f_{RF} produces pulses with lower amplitude and longer duration, as the injected current per period is reduced with shorter sinusoid period. The value of f_{RF} separating multi spike from single spike regions, also depends on P_{RF}, as both I_{BIAS} and P_{RF} affects the relaxation oscillation frequency. Single pulses with shorter duration are obtained at higher f_{RF}, with the higher values of I_{BIAS}, as it is shown in Fig. 5.6 (right).

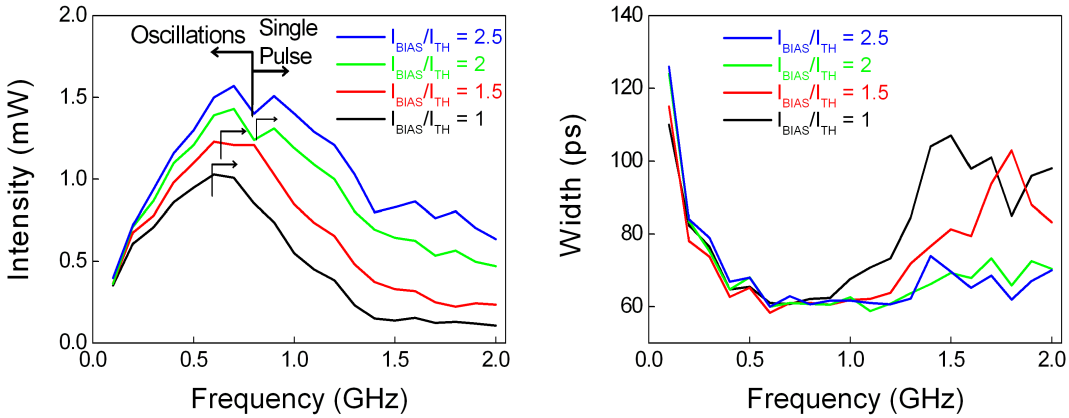

Figure 5.6: Amplitude (left) and duration (right) of the first spike of relaxation oscillations versus f_{RF}, with $P_{RF} = 10.5$ dBm, varying I_{BIAS}/I_{TH} between 1 and 2.5. The arrows indicate the value of f_{RF} separating the regimes of multiple and single peak output.

Single pulse per period are generated and the dependence of the pulse amplitude and Full Width at Half Maximum (FWHM) as a function of I_{BIAS} is investigated

at 2 GHz, varying I_{BIAS} between 1.5 and 3.5 I_{TH}, for different values of P_{RF} (7, 10 and 13 dBm), see Fig. 5.7 (left). With I_{BIAS}, the maximum injected current also increases, resulting in a higher relaxation oscillation frequency and in a larger portion of the sinusoid above I_{TH}. Consequently, at low values of I_{BIAS}, weak and relatively long pulses are obtained and as I_{BIAS} increases pulses are stronger and shorter. This behavior is observed until the amplitude of the pulse saturates and the FWHM increases again, due to the excitation of the second relaxation oscillation at high values of I_{BIAS}. As a result, the pulse duration has a minimum value at a certain value of I_{BIAS}, depending on f_{RF} and P_{RF}, typical of GS lasers [Paul 88]. The same dependence on I_{BIAS} is observed for different values of P_{RF}, with greater amplitude and smaller pulse duration for increasing values of P_{RF}, as the relaxation oscillation frequency is also increased.

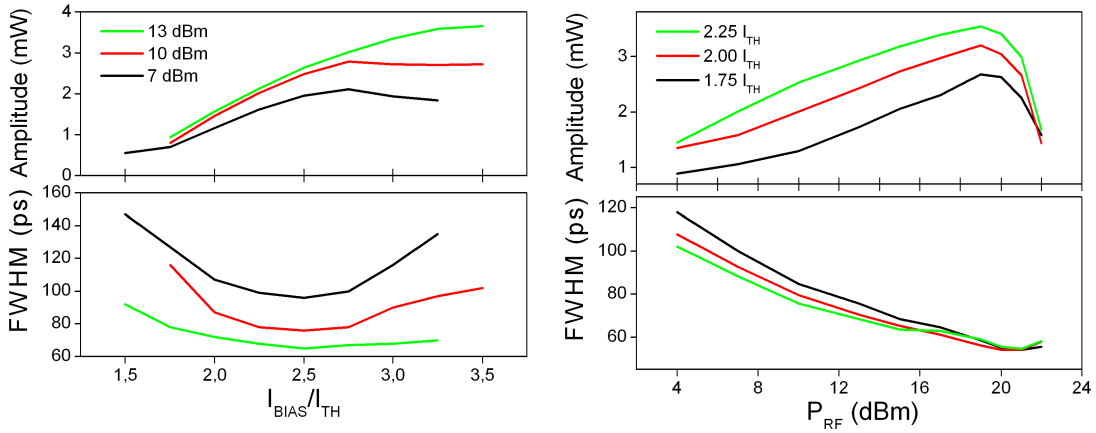

Figure 5.7: Pulse amplitude and FWHM as a function of I_{BIAS}/I_{TH} at a repetition rate of 2 GHz for P_{RF} =7, 10 and 13 dBm (left). Pulse amplitude and FWHM as a function of P_{RF}, at repetition rate of 1.5 GHz, for different I_{BIAS}/I_{TH} =1.75, 2 and 2.25 (right).

Figure 5.7 (right) shows the pulse amplitude and FWHM at a repetition rate of 1.5 GHz as a function of P_{RF} with I_{BIAS} as the parameter. When P_{RF} is increased until 19 dBm, the peak amplitude is higher and the duration shorter, but above this value the pulse amplitude rapidly decreases and the FWHM slightly increases. This is attributed to the fact that, initially, the laser responds with faster and more intense pulses that evolve into sharper and shorter spikes due to the increasing injected current. However, above some point, the large modulation amplitude induces substantial device heating [Hasn 92, Wies 93] that degrades the laser response. As mentioned in Sec. 5.2, the thermal impedance of our VCSEL is around 1680 K/W. This value was used to estimate the temperature of the active region (T_{AR}) for the driving conditions in Fig. 5.7 (right). For the range of I_{BIAS} considered, when P_{RF}

is higher than 19 dBm, T_{AR} exceeds 50^{o} C, as it was checked by measuring the emission wavelength shift. Pulse degradation is then attributed to the high temperature reached in the active region.

The pulse timing jitter was measured directly at the oscilloscope at 1/3 the pulse amplitude on the pulse rising edge. The results at 1.5 GHz and 2 GHz are compared in Fig. 5.8. The pulse widths at both frequencies are similar, as it's expected from the small difference in relaxation oscillation frequency of the laser. However, we observed differences in the timing jitter and pulse amplitude. In both cases, the measured jitter initially decreases with P_{RF} due to the larger current amplitude that speeds up laser response and narrows the distribution of turn-on delays [Pepe 93b].

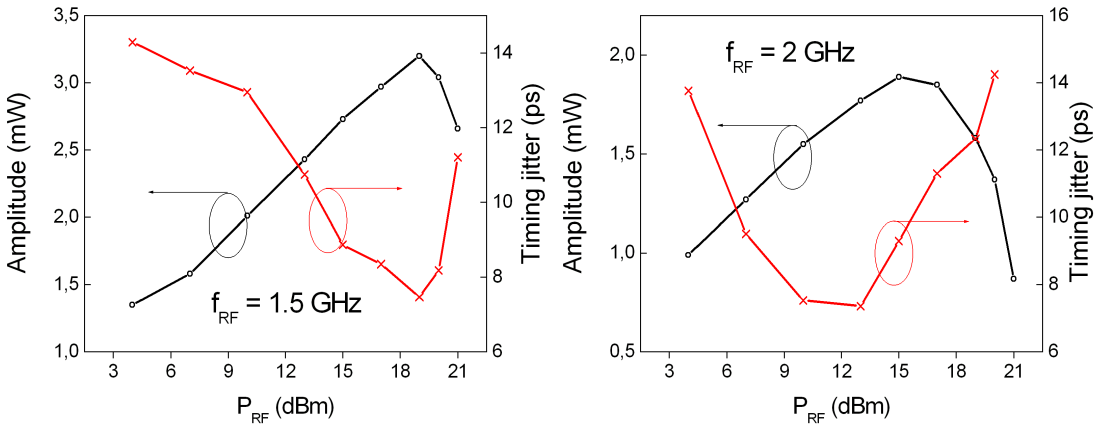

Figure 5.8: Timing jitter and pulse amplitude versus P_{RF} with $I_{BIAS}/I_{TH} = 2$ for $f_{RF} = 1.5$ GHz (left) and $f_{RF} = 2$ GHz (right).

At 1.5 GHz, the jitter reduction lasts until $P_{RF} \sim 19$ dBm, the value where a maximum of the pulse amplitude is observed, while at 2 GHz, the minimum jitter is obtained for P_{RF} ~12 dBm, a value lower than the maximum of the pulse amplitude which takes place at P_{RF} ~16 dBm. The increase of jitter after some point is thought to be related with device heating, which causes an increase of the statistical distribution of carrier lifetime and consequently of the turn-on times. The difference in the value of P_{RF} at which the minimum jitter occurs at 1.5 and 2 GHz is attributed to both electrical and thermal effects, which are closely intermixed at the very high modulation amplitude used in these experiments.

The spectra of the pulse trains obtained at 2 GHz with $I_{BIAS}/I_{TH} = 2$ for three values of P_{RF} (5, 19, and 21 dBm) are plotted in Fig. 5.9 (right). The traces are centered at the peak wavelength for clarity. As P_{RF} is increased, the spectrum redshifts (2.51 nm at 21 dBm respect to 5 dBm, not shown in the figure) and the peak value decreases, due to the heating effect of injected current. The spectral width

broadens because of the deeper modulation of carriers, thus giving rise to more chirped pulses. The secondary peak at about 0.5 nm above the main peak, which emits in the orthogonal polarization with respect to the main peak, is enhanced, due to the competition of the two polarization modes at the turn-on of the laser, which is increased by the greater values of P_{RF}.

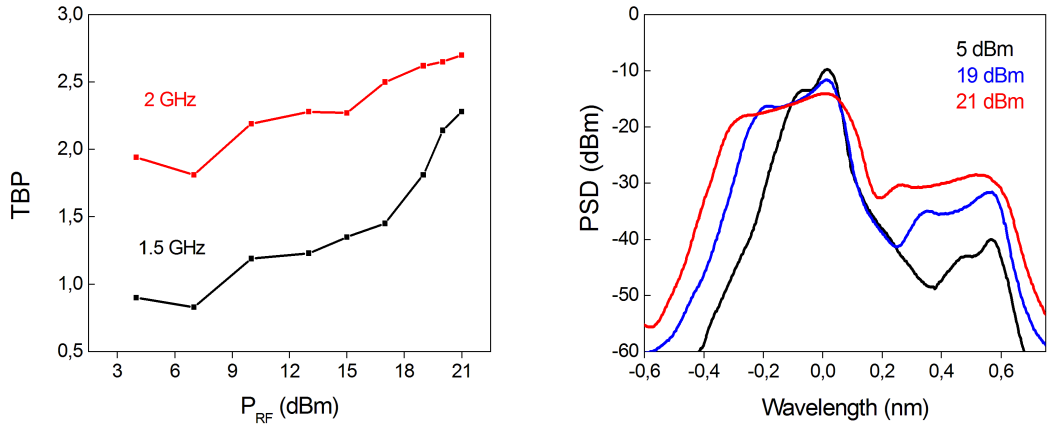

Figure 5.9: The TBP as a function of P_{RF} with $I_{BIAS}/I_{TH} = 2$ and $f_{RF} = 1.5$ and 2 GHz (left). The pulse spectra with $f_{RF} = 2$ GHz, $I_{BIAS}/I_{TH} = 2$ and $P_{RF} = 5$, 19 and 21 dBm (right), spectra have been wavelength shifted for clarity.

The broadening of the pulse spectra caused by the frequency chirp during switch-on was studied as a function of the gain switching conditions. The spectra of the generated pulses are measured and the Time Bandwidth Product (TBP) was calculated as the product of the FWHM of the temporal and spectral widths. The measured TBP is shown in Fig. 5.9 (left) as a function of P_{RF}, for $I_{BIAS}/I_{TH} = 2$ at 1.5 and 2 GHz. The TBP increases with P_{RF} due to the larger modulation of carrier density, as expected with the gain switching technique. For $P_{RF} = 7$ dBm and $f_{RF} = 1.5$ GHz, the pulses have a very low TBP of 0.83 and duration of 92.7 ps. At 2 GHz, the TBP is larger than at 1.5 GHz, due to the faster increase of carriers at higher frequency, yielding deeper carrier oscillation during the light emission, and in consequence higher chirp and TBP.

The operating conditions I_{BIAS} and P_{RF} were varied in order to obtain the shortest pulse widths at frequencies between 1 and 3 GHz. Table 5.1 reports the pulse durations, the spectral widths, the TBP, and the gain switching parameters. The increase of f_{RF} shortens the time slice in which current overcomes threshold and efficient pulse generation is obtained if more carriers per period are injected. Consequently, I_{BIAS} and P_{RF} have been increased with f_{RF}.

At 1 GHz, the TBP is as low as 0.91 for pulse duration of 65 ps. When increasing the frequency, shorter pulses are obtained, but with larger spectral widths, thus

$f_{RF}(GHz)$	I_{BIAS}/I_{TH}	$P_{RF}(dBm)$	$\Delta t(ps)$	$\Delta\nu(GHz)$	TBP
1	2	13	65	14	0.91
1.5	2.25	18	64	25.2	1.61
2	2.5	19	61	26	1.58
2.5	2.75	19	55	37.5	2.06
3	3	18	55	40	2.2

Table 5.1: Pulse duration and bandwidth at different repetition rates and gain switching conditions.

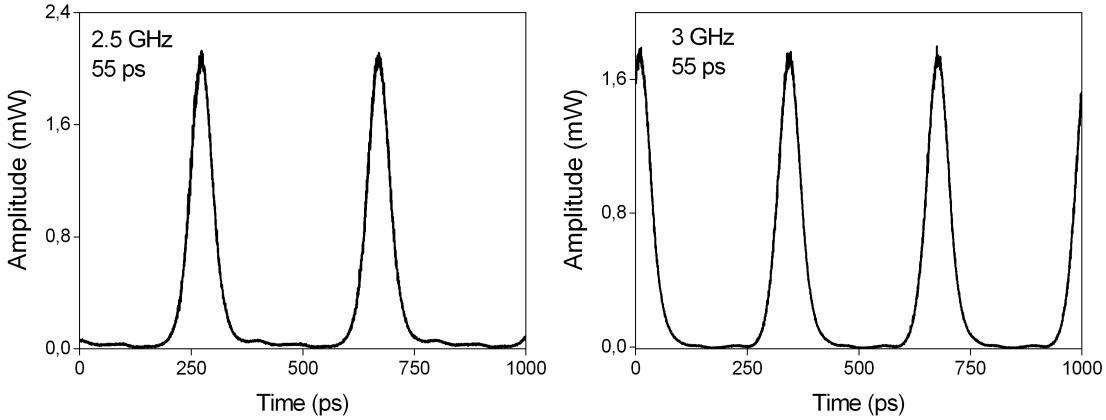

Figure 5.10: Pulse trains with the shortest pulse duration obtained at 2.5 (left) and 3 GHz (right).

greater TBP values. The shortest pulses are obtained at repetition rates of 2.5 and 3 GHz. At both frequencies, the FWHM is 55 ps and the TBP varies between 2.06 and 2.2. The minimum pulse duration of 55 ps is longer than the best reported value in 850-nm VCSELS, 14.6 ps [Pepe 94]. The pulse trains with the shortest pulse duration obtained at 2.5 and 3 GHz are plotted in Fig. 5.10.

5.4 Conclusions

In this Chapter, the generation of pulses from a GS VCSEL emitting at 1.5 µm is reported. The dependence of pulse peak amplitude, duration, jitter and TBP on the gain switching parameters is investigated. Optimum values of I_{BIAS} and P_{RF} are found for shortest pulse generation at repetition rates between 1 and 3 GHz. Device heating from current injection at high modulation intensities is found to be a limiting factor for the generation of shorter pulses, as it directly affects pulse quality, reducing peak amplitude and increasing pulse width and jitter. The polarization

mode competition at high modulation frequencies is also increased together with the spectral width of the main mode and the pulse chirp. Depending on the gain switching parameters, short and highly chirped pulses (55 ps and 2.2 TBP) or longer low chirped pulses (65 ps 0.91 TBP) can be obtained.

Chapter 6

Jitter reduction in optically injected gain switched VCSEL

In this Chapter, the experimental results and numerical simulations of an optically injected GS 1.55 μm VCSEL are presented. Optical injection is briefly described and its application to semiconductor lasers for performance improvement is presented, e.g. reduction of the chirp, enhancement of the modulation bandwidth, increase of the side mode suppression ratio. The experimental set-up is described and the suppression of the secondary polarization mode, depending on the polarization of the injected light, when the laser is operating either in CW or GS, is reported. The pulse generated when the VCSEL is GS at 100 MHz and 1 GHz, varying the modulation parameters, are characterized in peak amplitude, timing jitter and FWHM duration. A relevant decrease of the timing jitter due to optical injection is observed, with a slight increase of the pulse width. A rate equations model, which consider transverse carrier distribution and the two polarization modes, is presented. Numerical simulations are performed with the same conditions of the experiments and a good qualitative agreement is obtained between simulations and experimental results.

6.1 Introduction

Optical injection (OI) refers to the technique in which the light from a laser (named as the *master* laser, ML) is sent to another laser (the *slave* laser, SL), via a unidirectional passive optical component such as an optical circulator, to modify in a controlled manner the emission characteristics of the SL, as illustrated in Chapter 3. A rich variety of phenomena takes place in a semiconductor laser when subjected to OI, such as injection locking, periodic pulsations, multi stability and chaos [Ohts 05]. Injection locking occurs when the frequency of the SL is locked to the frequency of the ML. Since the first studies on OI in semiconductor lasers, injection locking has proved to be an efficient way to improve the transmission performance of the injected laser. In 1980, the first demonstration of injection locking on a AlGaAs semiconductor laser was reported by Kobayashi and Kimura [Koba 80], who obtained a significant frequency stabilization of the injected laser. Single longitudinal mode operation of a multi mode FP laser subjected to OI was reported two years later by Iwashita and Nakagawa [Ywas 82]. The same year, Lang [Lang 82] published the first theoretic work on injection locking of semiconductor lasers, which established the theoretical framework and paved the way for various subsequent theoretical predictions and studies.

In the last two decades, many research group have demonstrated laser performances improvement in terms of chirp reduction [Lin 84a, Olss 85], modulation bandwidth enhancement [Simp 95, Liu 97], and broadband noise reduction [Jin 00] in EE devices subjected to OI. In the last years, a great interest has raised for OI in VCSELs, due to the promising characteristics of these devices with respect to EE lasers, e.g. single longitudinal mode operation, circular output beam, low threshold, wafer level testability, low current operation, which make VCSELs competitive optical sources for telecommunication channels and all optical signal processing [Koya 06].

Very high modulation speed and resonance frequency have been reported recently in a 1.5 µm VCSEL subjected to OI [Chro 07]. Adjustable chirp by means of OI in directly modulated 1.55 µm VCSELs at 10 GHz have also been reported, allowing error-free transmission over 40 km of SM fiber [Gatt 09]. Non linear dynamics of parallel and orthogonal polarization injection has been recently investigated by Hurtado et al. [Hurt 09] and a rich variety of phenomena has been experimentally demonstrated, e.g. periodic pulsations in limit cycle and period doubling and chaos. Recently the VCSEL to VCSEL injection scheme, in which both ML and SL are VCSELs, is receiving much attention due to practical advantages of this scheme in a real telecommunications system [Gatt 09, Haya 09]. The influence of OI on the

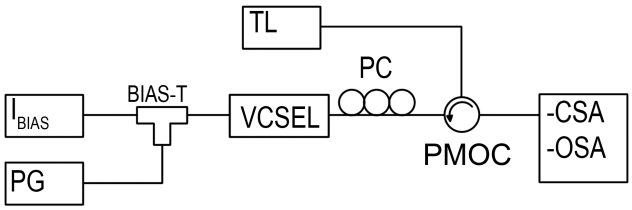

Figure 6.1: Set-up for optical injection in GS VCSEL. Components are described in the text.

timing jitter of GS VCSELs has been investigated by Noriega et al. [Nori 08] and the authors found that a reduction of more than 70% of the pulse timing jitter can be achieved. The theoretical prediction reported in [Nori 08] have been experimentally demonstrated recently in a long wavelength GS VCSEL subjected to OI [Cons 09c, Cons 09b, Cons 10b] at the repetition rates of 1 GHz and 100 MHz.

6.2 Orthogonal polarization suppression

The setup used to perform optical injection in a GS long wavelength VCSEL is shown in Fig. 6.1. The VCSEL structure and CW characteristics have been described in Chapter 4 and 5.

Light from a external cavity Tunable Laser (TL, Anritsu Tunics Plus-CL) is injected into the VCSEL through a Polarization Maintaining Optical Circulator (PMOC). A polarization controller (PC) is used to change the polarization of the injected light into the VCSEL. The VCSEL is fed through a bias-tee with a bias current I_{BIAS} and a rectangular pulse train from a pulse generator (PG, Anritsu MP1800A), with frequency f_{PG}, pulse amplitude V_{PG} and pulse width W_{PG}. Temporal and spectral pulse intensities are measured respectively with the optical module (Tektronix 80C06-CR, 20 GHz of bandwidth) of a Communication Signal Analyzer (CSA, Tektronix CSA8000) and with an OSA with 0.07 nm wavelength resolution (Anritsu MS9710B).

The VCSEL threshold current, I_{TH}, is 2.3 mA. The VCSEL spectrum, under CW operation, has multiple peaks, corresponding to the fundamental and higher order transverse modes, each characterized with two orthogonal linear polarization modes, as explained in Chapter 5. The two peaks at 1555.4 nm and 1555.9 nm, shown in Fig. 6.2, correspond to the parallel ($\parallel$) and orthogonal ($\perp$) polarizations of the fundamental transverse mode. Under CW operation and for all the current range, the orthogonal mode is suppressed more than 30 dB with respect to the parallel mode and no polarization switching is observed.

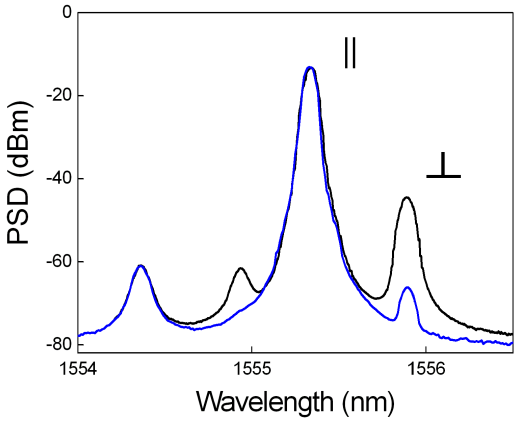

Figure 6.2: Optical spectrum of the CW biased VCSEL when I_{BIAS} = 3 mA without polarization selection (solid black line) and with the orthogonal polarization suppressed (solid blue line).

The solid black line of Fig. 6.2 corresponds to the optical spectrum when I_{BIAS} = 3 mA and the frequency detuning is zero. In the setup of Fig. 6.1, the PC is adjusted in such a way that the light is injected parallel to the dominant linear polarization. In this situation, the secondary orthogonal polarization suffers a maximum attenuation because it orthogonally couples to the preferential direction of the polarization maintaining OC. This is illustrated in Fig. 6.2, where the solid blue line corresponds to the spectrum with the orthogonal polarization suppressed.

Under CW operation the orthogonal polarization is suppressed more than 30 dB with respect to the parallel polarization of the fundamental transverse mode (see the two peaks at longer wavelengths of the solid line of Fig. 6.2). However, when the VCSEL is modulated the secondary orthogonal polarization is enhanced. We show in Fig. 6.3 the spectra obtained when the VCSEL is GS with a repetition rate of 100 MHz under the following conditions: I_{BIAS} = 3 mA, V_{PG} = 2.5 V, W_{PG} = 250 ps and a consequent low duty cycle of 2.5%, when free running (black line) and under OI (blue line).

During GS operation, the mode competition at the turn-on of the laser is enhanced and the Side Mode Suppression Ratio (SMSR) is consequently reduced more than 20 dB with respect to the CW operation, resulting in a poor suppression of about 7 dB of the orthogonal mode with respect to the parallel mode, as shown with solid black line in Fig. 6.3. The solid blue line of Fig. 6.3 corresponds to the spectrum of the GS VCSEL when the VCSEL is subjected to OI, the frequency detuning is zero and the PC is adjusted in such a way that the ML polarization matches the parallel polarization of the VCSEL, resulting in a suppression of more than 20 dB of the orthogonal mode.

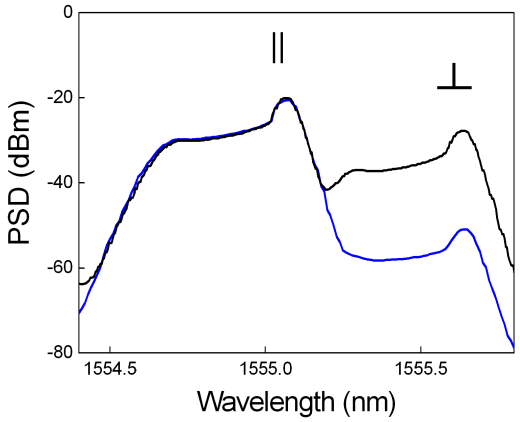

Figure 6.3: GS VCSEL spectra for a repetition rate of 100 MHz without polarization selection (solid black line) and with the orthogonal polarization suppressed (solid blue line).

6.3 Injection range for jitter reduction

The timing jitter, pulse width and peak amplitude have been measured when the VCSEL is GS at two different repetition rates (1GHz and 100 MHz) as a function of the injected optical power (P_{inj}) and the frequency detuning $\Delta\nu = \nu_{ML} - \nu_{\parallel}$, defined as the difference between the frequency of the ML (ν_{ML}) and the frequency of the parallel mode of the VCSEL ($\nu_{\parallel}$).

We first consider the case in which the VCSEL is GS at f_{PG} = 1 GHz, with V_{PG} = 2.5 V, W_{PG} = 500 ps, and I_{BIAS} = 1.3 I_{TH}. The PC is adjusted in such a way that the ML polarization matches the parallel polarization of the VCSEL, and the VCSEL is locked to the ML, with consequent suppression of the orthogonal mode. Figure 6.4 shows the spectra of the GS VCSEL when it is free running (solid black line) and subjected to OI (solid blue line), when P_{inj} = 1 mW and $\Delta\nu$ = 5 GHz.

Spectral broadening and SMSR reduction with respect to CW operation are observed, as expected in GS lasers, due to the chirping effect of carrier induced index modulation and the enhancement of mode competition at the laser turn-on, respectively [Vasi 00]. Both effects are counteracted by OI, as the spectral width is reduced from 14.8 GHz, in the case of free running GS VCSEL, to 9.3 GHz, when the GS VCSEL is subjected to OI, and the SMSR is enhanced of more than 20 dB. This is in agreement with previously reported results on GS DFB lasers subjected to OI [Guig 07].

The pulse intensities obtained with P_{inj} = 1 mW and λ_{ML} = 1558.58, 1548.48 and 1558.26 nm, that correspond to a frequency detuning of $\Delta\nu$ = -35, -22.5 and 5 GHz, respectively are shown in Fig. 6.5. The left column shows the averaged pulse

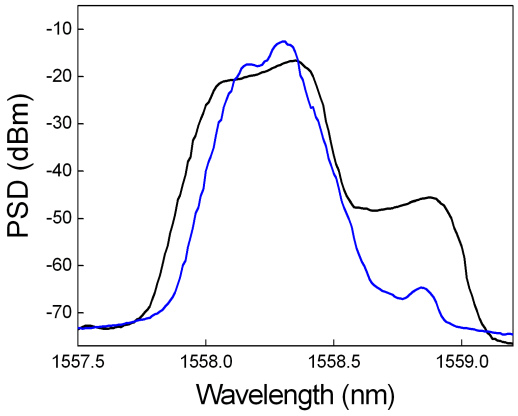

Figure 6.4: GS VCSEL spectra for a repetition rate of 1 GHz without (solid black line) and with (solid blue line) OI (P_{ML} = 1 mW, $\Delta\nu$ = 5 GHz).

intensities, from which the pulse FWHM and peak amplitude are obtained. On the right column the oscilloscope traces are shown, from which the timing jitter has been measured on the rising edge of the pulse at one third of the maximum. Pulses obtained when λ_{ML} = 1558.58 nm are very similar to the ones obtained without OI (with FWHM of 59.7 ps and peak amplitude of 0.79 mW) because the frequency detuning, $\Delta\nu$ = -35 GHz, is very large (the VCSEL is unlocked and the OI has negligible effect on the injected VCSEL).

The peak amplitude, pulse width and timing jitter obtained with P_{inj}= 1 mW and varying the frequency detuning $\Delta\nu$ between -40 and + 45 GHz are shown in Fig. 6.6. Figures 6.5 and 6.6 show that pulses become wider and more asymmetric as λ_{ML} approaches $\lambda_{\|}$. That detrimental fact is however compensated by the much smaller values of the timing jitter when λ_{ML} approaches $\lambda_{\|}$, as it is shown in Fig. 6.6. The decrease of the timing jitter is also evident in Figs. 6.5 (d)-(f) in which the detuning is varied from -35 GHz to 5 GHz.

Figure 6.6 shows that for a detuning range from –20 to 27 GHz optical injection reduces the 11.6 ps jitter of the solitary VCSEL to a value below 4 ps. The averaged value of the jitter over that 47 GHz detuning range is 3.45 ps that results in a jitter reduction larger than 70%. Over that $\Delta\nu$ range the averaged FWHM is 73 ps corresponding to a slight increase of the pulse width (22 %) with respect to the free running case. It can also be seen that low values of the jitter also result in pulse broadening. A clear anticorrelation between pulse peak and pulse width is seen in Fig. 6.6 in the detuning range –24 GHz $< \Delta\nu <$ 30 GHz, with a value of the correlation coefficient, defined as the covariance of two variables divided by the product of their standard deviations [Mend 06], of -0.93.

Similar measurements were also performed at 100 MHz, because of the relevance

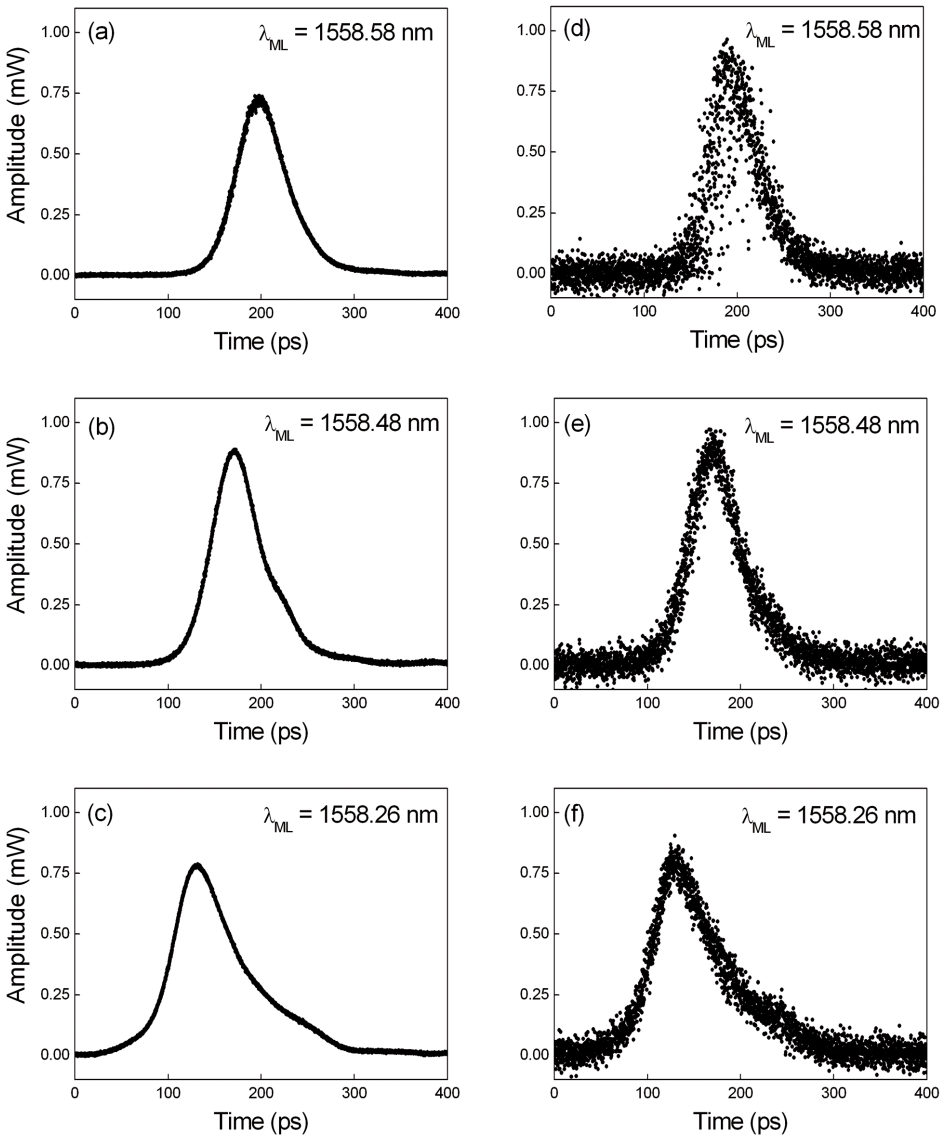

Figure 6.5: Averaged shapes of pulses generated by the GS VCSEL subjected to OI for three values of λ_{ML} and $P_{ML} = 1$ mW are shown in parts (a), (b) and (c) that correspond to a frequency detuning of $\Delta\nu$ = -35, -22.5 and 5 GHz, respectively. The corresponding oscilloscope traces are shown in parts (d)-(f).

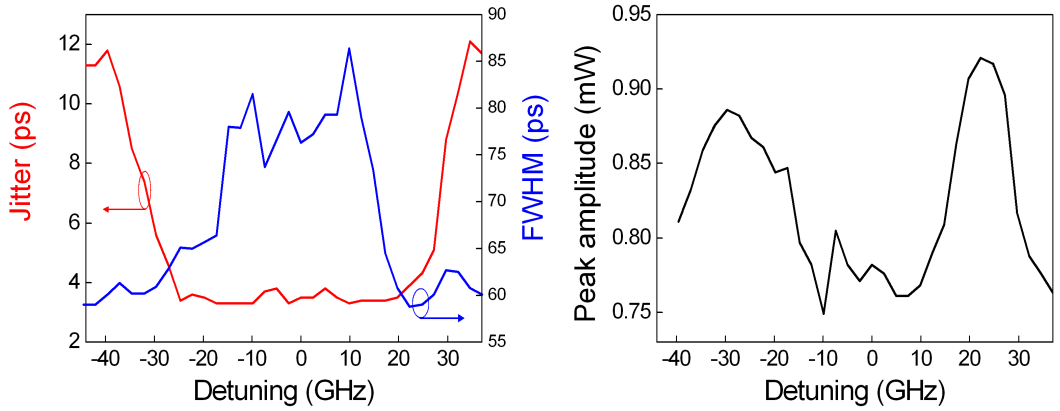

Figure 6.6: Jitter, FWHM (upper figure, left and right axis respectively) and peak amplitude (lower figure) as a function of frequency detuning $\Delta\nu$ when $P_{inj} = 1$ mW and $f_{PG} = 1$ GHz, $V_{PG} = 2.5$ V, $W_{PG} = 500$ ps, and $I_{BIAS} = 1.3\ I_{TH}$.

of applications of GS pulses at this low frequency. Concretely, the interest is on the realization of the OCDMA encoder, based on fiber optical delay lines and GS VCSEL, described in Chapter 7.

The VCSEL is GS at $f_{PG} = 100$ MHz, with $V_{PG} = 2.5$ V, $W_{PG} = 250$ ps and $I_{BIAS} = 0.87\ I_{TH}$, generating pulses of about 60 ps FWHM duration when free running, thus a very low duty cycle of 0.6 %. The injected power P_{inj} is kept at 1 mW and the detuning $\Delta\nu$ is varied between -47 and + 44 GHz, the measured pulse FHWM and timing jitter are shown in Fig. 6.7. Under OI the timing jitter decreases with respect to its value of 11 ps for the free running GS VCSEL, over a wide detuning range. For $\Delta\nu$ between –20 GHz and GHz, the jitter is less than 3 ps, which corresponds to a reduction of 72 % with respect to the free running case. As it can be appreciated in Fig. 6.7, the qualitative behavior of jitter and FWHM is similar to the 1 GHz repetition frequency case.

6.4 Comparison with simulation

The jitter reduction obtained in the reported experiments has been previously predicted by Noriega *et al.* [Nori 08] in a single transverse and polarization mode 1.55 µm VCSEL. The model employed in [Nori 08] has been extended by the same author, including the two orthogonal polarization modes which characterize the device under study. Here the main characteristics of the model are summarized and the results of the simulations are compared with experiments described in Sec. 6.3, with the goal of validating the model and obtaining a better understanding of the OI effects.

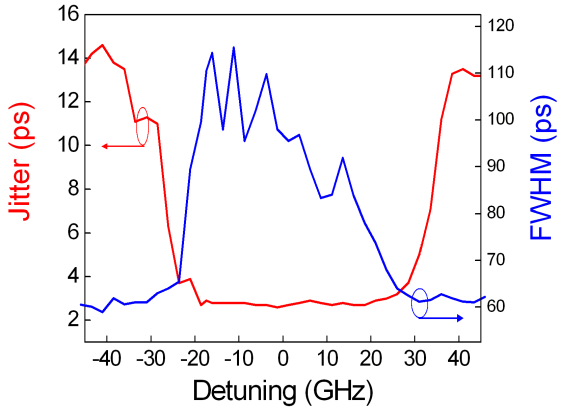

Figure 6.7: Jitter (red solid line, left axis) and pulse FWHM duration (blue solid line, right axis) as a function of $\Delta\nu$ when the repetition frequency is 100 MHz and $P_{ML} = 1$mW.

The model incorporates both spatial dependence of carrier density and optical field profiles [Vall 98]. A cylindrical weakly-index guided VCSEL with transverse modes LP_{mn} is considered and the dynamical (temporal) evolution of the complex field amplitude of each mode is given by:

$$\frac{dE_i(t)}{dt} = \frac{(1-j\alpha)}{2}\left(v_g g_i(t) - \frac{1}{\tau_{P,i}}\right)E_i(t) + \sqrt{\frac{\beta\pi d\int_0^a N(r,t)rdr}{\tau_N}}\xi_i(t) + \kappa_i\sqrt{P_{inj}}\exp(-j2\pi\Delta\nu_i t) \quad (6.1)$$

where $g_i(t)$ and $\tau_{P,i}$ are the modal gain and photon lifetime, respectively, of the i mode, v_g is the group velocity, Γ is the longitudinal confinement factor, a is the radius of the waveguide, d is the active region thickness, τ_N is the carrier lifetime, α is the linewidth enhancement factor, β is the spontaneous emission factor, ξ is a complex white Gaussian noise term of zero mean, and $N(r,t)$ is the carrier density, which is dependent on the spatial coordinate r and time t. The last term of Eq. 6.1 accounts for optical injection, where P_{inj} is the injected power, κ_i is the coupling coefficient into the i mode and $\Delta\nu_i = \nu_{ML} - \nu_i$ is the frequency detuning between the ML frequency and the frequency of the i mode. Results are given in terms of the detuning $\Delta\nu = \nu_{ML} - \nu$ with respect to the frequency of the lowest threshold mode.

The modal gain $g_i(t) = \int_0^\infty \Psi_i^2(r)\, A\, (N(r,t) - N_{TR})\, rdr / \langle\Psi_i^2\rangle$ is defined for the i mode, where the symbol $\langle\,\rangle$ is used for denoting the following integral, $\langle f\rangle = \int_0^\infty f(r)rdr$, where r is the modulus of the spatial vector in the active layer, $\Psi_i(r)$ is

the electrical field profile of the i mode, N_{TR} is the carrier density at transparency and A is the gain coefficient. The modal gain is dependent on the degree of spatial overlap between the mode intensity profile and the carrier distribution. The evolution of the carrier density profile, $N(r,t)$, is given by the carrier continuity equation applied to the active region:

$$\frac{\partial N(r,t)}{\partial t} = +\frac{J(r,t)}{qd} - \frac{N(r,t)}{\tau_N} + \frac{D}{r}\frac{\partial}{\partial r}\left(r\frac{\partial N(r,t)}{\partial r}\right) - \sum_i a_i \Psi_i^2(r) g_i(t) P_{inj}(t) \quad (6.2)$$

where D is the diffusion coefficient, $J(r,t)$ is the current density injected in the active region, q is the electron charge, and $a_i = v_g \Gamma / (2\pi d \langle \Psi_i^2 \rangle)$. We consider a uniform injection of current over a disk of radius s and then, $J(r) = J$ if $r < s$, and $J(r) = 0$ elsewhere. The evolution of the electrical field is found by integrating Eqs. 6.1 and 6.2. A complete description of the model together with the values of the parameters can be found in [Vall 98, Nori 08, Cons 10b].

In the presented model, The VCSEL is assumed as emitting only in the two linear polarizations of the fundamental mode LP_{01} at a wavelength 1558.3 nm for the dominant parallel polarization mode and 1558.79 nm for the orthogonal mode. This is accomplished in the model by considering that the modal losses of these two polarizations are much smaller than those of the rest of the modes. Also, the transverse field profile is assumed to be the same for the two polarizations , $\Psi_1(r) = \Psi_2(r)$, corresponding to the fundamental transverse mode. Under CW operation the orthogonal polarization is suppressed more than 30 dB with respect to the parallel polarization in agreement with the experimental results.

A square-wave modulation is applied to the VCSEL with a repetition rate of 1 GHz and duty cycle of 50%. The laser is switched from below threshold to above threshold. A bias current $J_{BIAS} = 0.5\ J_{TH}$ and current amplitude of $J_{ON} = 2\ J_{TH}$ are considered, being J_{TH} the threshold current density. The power of the injected signal P_{inj} is given in dBs with respect to the power of the solitary laser P_{ON}, that corresponds to the on-state current J_{ON}. The light is injected parallel to the dominant linear polarization.

The simulated optical spectrum of the free-running VCSEL is shown in Fig. 6.8 (solid black line). Spectral broadening due to chirping effects is observed and the SMSR of the orthogonal polarization is only 7.5 dB with respect to the parallel polarization, which means a reduction of more than 20 dB with respect to CW operation, in agreement with the experimental results shown in Fig. 6.3.

The optical spectrum of the VCSEL subjected to OI, when P_{inj} = -34 dB and $\Delta\nu = 5$ GHz, is also shown in Fig. 6.8 (solid blue line). The OI reduces the spectral

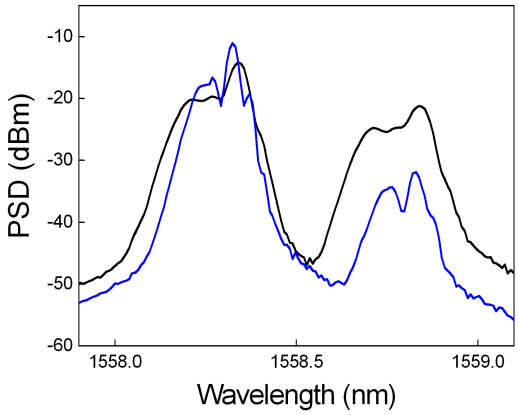

Figure 6.8: Theoretical results for the optical spectrum of a GS VCSEL without (solid black line) and with (solid blue line) OI (P_{inj} = -34 dB and $\Delta\nu$ = 5 GHz).

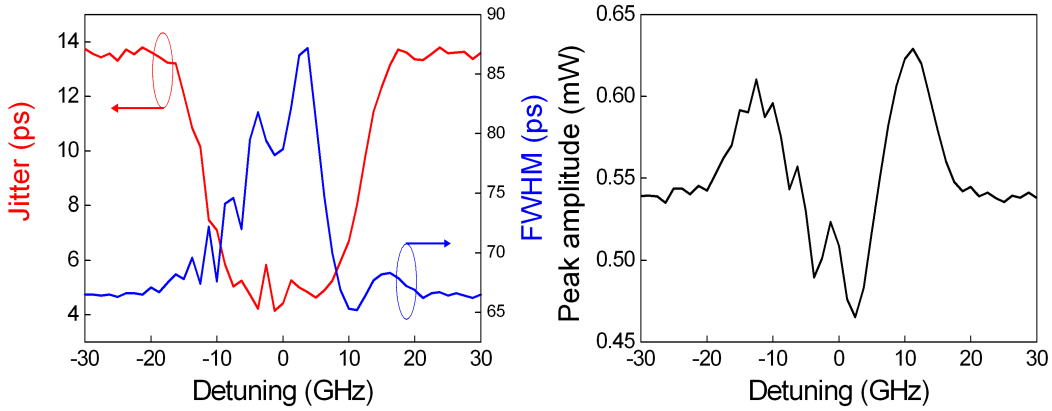

Figure 6.9: Theoretical results for jitter and FWHM duration (red and blue line, upper figure respectively) and peak amplitude (lower figure graph) as a function of frequency detuning $\Delta\nu$ when the repetition frequency is 1 GHz and P_{inj} = -34 dBm.

width of the parallel mode of 29 % and improves the SMSR of the orthogonal mode of 13 dB, with respect to GS operation. These results are in qualitative agreement with the measurements shown in Fig. 6.4.

The timing jitter, FWHM duration and peak amplitude of the pulses are obtained from the model as function of P_{inj} and $\Delta\nu$. Only the parallel polarization component is considered for comparison with the experimental results. Figure 6.9 shows the jitter and FWHM as a function of the frequency detuning $\Delta\nu$ for an injection power of -34 dB. A good qualitative agreement is obtained between the theoretical and the experimental results shown in Fig. 6.6. It is found that for a detuning range from -10 to 10 GHz, OI reduces the 13.6 ps jitter of the solitary VCSEL to a value below 7 ps. The averaged value of the jitter over that 20 GHz detuning range is 5.2 ps that results in a jitter reduction larger than 60%. When the injected power P_{inj} is

increased, jitter reduction can be achieved for a greater detuning range. However, the oscillations of the jitter (see Fig. 6.9 for small negative values of $\Delta\nu$) also increase. Over the detuning range from –10 to 10 GHz the averaged FWHM is 76 ps that produces a slight increase of 15% in pulse width with respect to the free running case. It can also be seen that low values of the jitter result in pulse broadening.

Figure 6.9 shows the peak amplitude as a function of the frequency detuning $\Delta\nu$ for an injection power of -34 dB. The theoretical result is again in good agreement with the experimental result shown in Fig. 6.6. A clear anticorrelation between the pulse amplitude and the pulse width is seen in Figs. 6.9 and 6.9 in the detuning range -15 GHz $< \Delta\nu <$ 15 GHz with a value of the correlation coefficient of -0.93. This value is very close to the one obtained from the experimental results.

6.5 Conclusions

The effect of OI on the characteristics of the pulses generated by a GS single transverse mode VCSEL emitting at 1550 nm is investigated. An experimental analysis is carried out of the effect of OI on the timing jitter, maximum power, and pulse width of optical pulses for two repetition rates, 100 MHz and 1 GHz, and for different values of the detuning between the frequency of the optical injection and the VCSEL. The qualitative behavior is similar for both repetition rates. In the 1 GHz case, jitter reduction larger than 70% over a 47 GHz detuning range centered around the VCSEL lasing frequency is obtained. This jitter reduction is accompanied by a slight increase in pulse width with respect to the free-running case. A clear anticorrelation between peak power and pulse width is observed. A theoretical study has been performed by using a model that incorporates both spatial dependence of carrier density and optical field profiles. The two polarization modes of the fundamental transverse mode are taken into account in the model. Timing jitter, maximum power, and pulse width are obtained for a repetition rate of 1 GHz, and for different values of the detuning between the frequency of the injected light and the VCSEL. The results obtained from numerical simulations for pulse characteristics are in good qualitative agreement with the experimental results.

Chapter 7

Optical Code Division Multiple Access Encoder based on a 1550 nm gain switched VCSEL

In this Chapter, an optoelectronic transmitter for a fiber based multi-user optical channel is proposed. The proposed device is based on a VCSEL emitting at 1.55 μm. The VCSEL is GS with a rectangular pulse train, with short pulse duration and low duty cycle. A special driving circuit has been developed for the generation of short electrical pulses with abrupt rising edge, for having efficient excitation of the laser relaxation oscillations during the GS laser operation. The multi-user approach is based on a Code Division Multiple Access (CDMA) channel, in which the communication from each user is coded in a specific manner. We report the implementation of a simple encoder based on a set of optical delay lines and two fiber splitter/combiner. A code signature for a 10 users 20 Mb/s channel is obtained and presented with the proposed encoder.

7.1 Introduction

CDMA is a network access strategy in which data from multiple users are transmitted concurrently over the network and differentiated with code specific detection. CDMA on a fiber optics communication channel allows asynchronous user access and avoids the overhead associated with synchronization or network protocols. Since its first proposal [Pruc 86], Optical CDMA (OCDMA) has been considerably developed due to the growing demand on information speed, channel capacity and traffic management. Different coding approaches have been developed in the last two decades: intensity time coding, spectral amplitude, spectral phase and spatial encoding are the four principal techniques used nowadays, see [Pruc 06] and references therein. Optical codes have been recently proposed for multi user indoor free space infrared [Hern 09] and visible light communication channels [Medi 11] and in this context, the code family of Random Optical Codes (ROC) [Mart 09] has emerged as a promising solution.

This Chapter presents the design and realization of an OCDMA encoder based on a temporal intensity coding approach, due to its simple implementation, reduced dimension and low cost realization. A set of delay lines is used to encode an optical pulse into a low intensity pulse train, i.e. replicas of the pulse are suitably positioned into various time slots or time chips. The main pulse is generated from a GS VCSEL emitting at 1.55 μm. Code generation has been demonstrated with a bit period of 50 ns, divided into 125 chips and an optical code with weight 8 has been used [Cons 09a].

7.2 System description

In OCDMA channels, the single bit is coded with a peculiar sequence of pulses with sub-bit duration, called chips. The code length, L_C, is the maximum number of chips that can be allocated inside one bit, i. e. $L_C = T_{BIT}/T_{CHIP}$, where T_{BIT} is the bit duration and T_{CHIP} is the chip duration. For example, a 1 Gb/s transmission (equivalent to a bit duration of 1 ns), coded with a code length of 1000, has a chip duration of 1 ps. The code weight, W_C, is the number of chips ($W_C < L_C$) coding the bit: their temporal positions inside the bit length makes the code signature, see Fig. 7.1. Two different codes with the same L_C and W_C differ by the code signature, given by the chip positions.

The proposed OCDMA encoder is based on the construction of a code from a periodic pulse train, in which the pulse duration is the chip duration T_{CHIP} and the period corresponds to the bit duration T_{BIT}. As a consequence, the pulse train duty

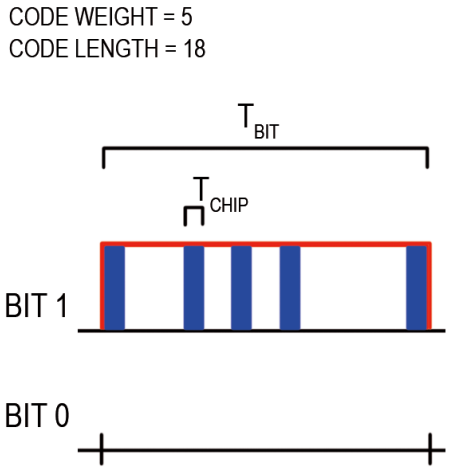

Figure 7.1: Coding principle of an on-off keying transmission.

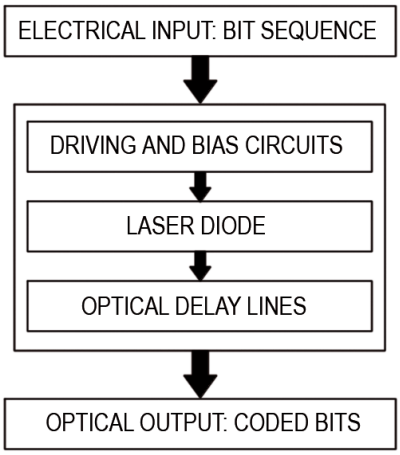

Figure 7.2: Block diagram of the OCDMA encoder

cycle, given by the pulse duration divided by the period, corresponds to the inverse of the code length L_C. The higher is the value of L_C, the higher is the number of potential users who can communicate on the same OCDMA channel[Pruc 06]. Thus, a pulse train with low duty cycle and short pulse duration is needed for our implementation of an OCDMA encoder.

The block diagram of the proposed encoder is depicted in Fig. 7.2. The bit sequence is sent to the driving circuit that modulates the laser and the bits are then coded through a set of optical delay lines. In the following sub sections, each part of the block diagram is described.

7.2.1 Driving and bias circuit

In Chapter 3, the pulse generation from a GS laser has been described and in Chapter 5 the pulse properties obtained with a GS VCSEL emitting at 1.55 µm have been discussed. The results indicate that pulses with duration of 55 ps can be obtained with a sinusoidal signal at the frequency of 2 GHz and 3 GHz, which allows a code lengths of 9 and 6, respectively. These low values of L_C are inadequate for a multi user OCDMA channel, being the typical code lengths an order of magnitude greater [Pruc 06]. Thus, a rectangular pulse train with low duty cycle has been chosen to drive the GS laser and a Step Recovery Diode (SRD) has been used for the generation of a short electrical pulse with fast rising time. The SRD is a diode with a very short recovery time, i.e. the time needed to switch from forward to reverse bias [Pack 84]. This characteristic is used to re-shape and shorten electrical

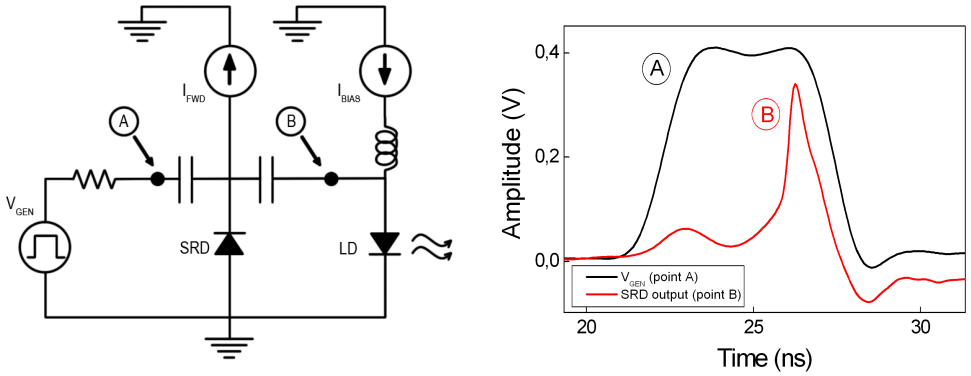

Figure 7.3: The driving and bias circuits (left). Waveforms at point A (black line) and B (red line) of the driving circuit (right).

pulses with properly designed circuits based on SRD.

The complete driving circuit is shown in Fig. 7.3 a). The signal (V_{GEN}) is a rectangular pulse waveform with pulse width of 5 ns and period of 50 ns. The pulse width is the minimum permitted by the available instrumentation (Tektronix AWG 420) and the period duration is large to increase the code length. A Step Recovery Diode is used to shorten the rise time and the duration of the rectangular pulse. The diode is forward biased with a current (I_{FWD}) of 6 mA. When V_{GEN} is 0 V, the diode is still forward biased and a low impedance value exists between the two terminals so that the cathode is almost at the ground potential. When V_{GEN} grows to a positive value, the diode switches to a high impedance state and all the charge is quickly transferred to the load. Due to the fast transition time of the SRD, the rise time and the duration of the current pulse are reduced. Figure 7.3 b) shows the waveforms captured at the oscilloscope. The pulse width of 5 ns is shortened to 0.9 ns. The output pulse is clearly asymmetric. The driving circuit could be improved if a second diode were used. In this work, the driving circuit has been designed to obtain a suitable waveform for gain-switching the laser with the available instrumentation.

7.2.2 Laser diode

The laser diode is a VCSEL emitting at 1.55 µm manufactured by Raycan, similar to the device described in Chapter 4. The choice of a VCSEL as the optical transmitter of the encoder is due to the well known advantageous characteristics of the device, described in Chapter 2: low threshold current, low power consumption, single longitudinal mode operation and high fiber coupling efficiency. The VCSEL threshold current (I_{TH}) is 2 mA and the bias current (I_{BIAS}) is set to 0.85·I_{TH} to

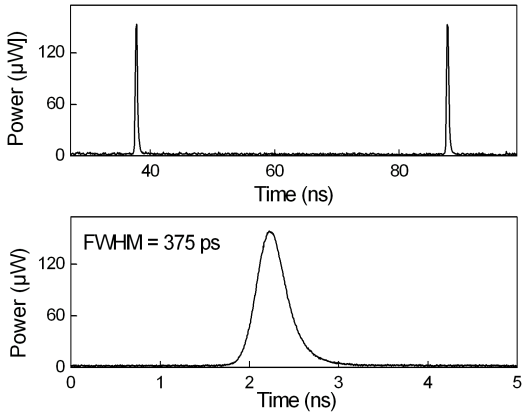

Figure 7.4: Single pulse (down) and pulse train (up) generated by the VCSEL.

extract only the first spike of relaxation oscillations in GS operation.

Figure 7.4 shows the pulse train and the single pulse obtained when the input at the driving circuit is a pulse with duration of 5 ns and the period is 50 ns. The optical pulse at the VCSEL output has a FWHM of 375 ps, yielding a duty cycle of 0.8%, which corresponds to 125 chip positions available for coding.

7.2.3 Optical delay lines

Coding process is obtained through the system shown in Fig. 7.5. The pulse train enters a 1x8 splitter and 8 weaker pulse replicas are obtained. They propagate through different lengths of fibers, each one selected in order to match the chip positions of the code. Pulses arrive with relative shifts in time at the 8x1 combiner, and the code is obtained at its output. The chip duration is 400 ps and, considering a group velocity in fiber of 0.2 mm/ps (for a refractive index of 1.5), the fiber length for one chip is around 80 mm. As the 1x8 splitter introduces insertion losses in the system ($>$ 9dB), an Erbium Doped Fiber Amplifier (EDFA) is placed at the VCSEL output, providing 5 dBm peak power for the input pulses.

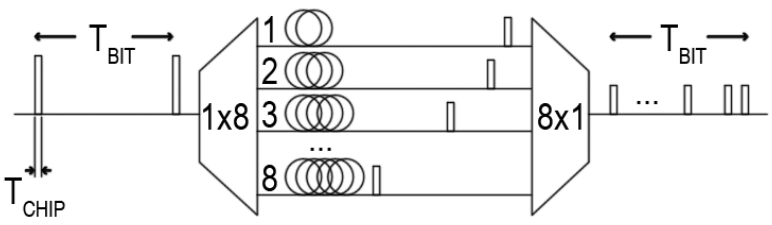

Figure 7.5: The optical delay lines used to generate the code.

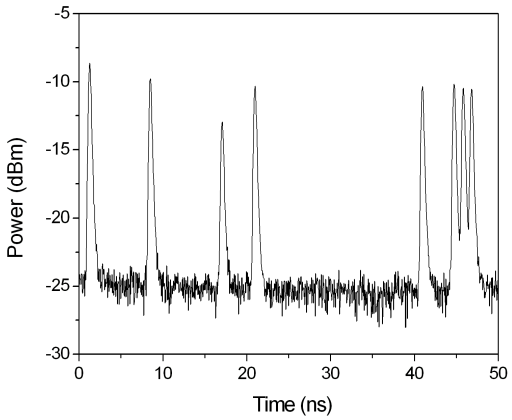

Figure 7.6: The code signature obtained at the output of the 8x1 combiner.

A Random Optical Code (ROC) [Mart 09] has been chosen for the generation of the code signature. The chip positions are obtained with a pseudo random number generator and one code signature is associated to each channel user. In the proposed OCDMA encoder implementation, a 10 users channel and a code family with $L_C = 125$, $W_C = 8$ are considered. The bit coding for a general user obtained with the selected ROC in the considered channel is shown in Fig. 7.6.

7.3 Conclusions

In this Chapter, an optoelectronic transmitter for an OCDMA communication channel at 1.55 µm is proposed. An electrical circuit based on a SRD allows the generation of electrical pulses with short duration and fast rising edge. The electrical pulse train drives the GS VCSEL and an optical pulse train with period of 50 ns and pulse duration of 375 ps is generated at the VCSEL output. The OCDMA code is obtained with a set of optical delay lines from the low duty cycle optical pulse train. A code signature based on the ROC code family, with length 125 and weight 8, is generated for a 10 users OCDMA channel at 20 Mb/s. The complete system is a compact, affordable and efficient solution which can be applied to a communication channel where a multi user environment is needed.

Chapter 8

Time resolved chirp measurements based on a birefringent interferometer

In this Chapter, a novel technique for the complete characterization of optical pulses is demonstrated. In the introduction, different techniques for the instantaneous frequency measurement of an optical signals are presented, with special attention to the Phase Reconstruction using Optical Ultrafast Differentiation (PROUD). A novel implementation of PROUD, based on optical differentiation using a birefringent interferometer, is reported. This new method is compared with previously reported techniques for the chirp measurement, presenting its benefits with respect to previous implementations. The time resolved frequency chirp of pulses generated with a GS semiconductor laser, with durations ranging between 100 ps and 800 ps, is measured. The pulse spectra have been reconstructed from the optical phase obtained with our implementation of PROUD and the measured pulse intensity. From the measured intensity and the recovered chirp, the linewidth enhancement factor of the laser is obtained. Furthermore, the proposed technique is compared to an iterative procedure for the phase retrieval using the temporal and spectral measured intensities. Finally, the advantages and limitations of the proposed method are summarized.

8.1 Introduction

The knowledge of the instantaneous frequency of an optical signal is a relevant issue in fiber optical communications where chirp compensation is often required to increase the transmission bit rate or length. In addition, pulse compression techniques, material characterization and chirped pulse amplification are fields of interesting applications for instantaneous frequency measurements of optical pulses. Moreover, in semiconductor lasers, the linewidth enhancement factor can be extracted from the pulse intensity and chirp [Koch 84].

The measurement of the pulse optical phase often reduces to a phase retrieval problem, as the temporal and spectral intensity are the two directly measured quantities from which the optical phase has to be deduced. When both temporal and spectral intensities are available, there exists a class of algorithm [Fien 82], basically inspired by the Gerchberg-Saxton algorithm [Gerc 72], which allows the phase retrieval from an iterative procedure based on Fourier transforming. The Gerchberg-Saxton algorithm was originally proposed for image reconstruction in astronomical measurements; in that case the phase retrieval concerned the spatial phase of the observed object. Indeed, the Gerchberg-Saxton algorithm has found multiple applications in different fields of engineering and physics.

In ultrafast optics, i.e. femtoseconds pulses, there is no direct detection system fast enough to capture the pulse temporal evolution and consequently the Gerchberg-Saxton cannot be applied. In fact, in this scenario, not only the phase is the unknown quantity but also the pulse temporal intensity. For this reason, pulse autocorrelation via a non-linear crystal was initially employed for the estimation of the duration and shape of pulses generated from broad band solid state femto lasers, e. g. Ti:sapphire laser. However, autocorrelation has an intrinsic limitation on its degree of precision, as the pulse shape must be assumed *a priori*, for a correct estimation.

Several techniques have been proposed for femtoseconds pulses characterization and there exits today a wide class of pulse measurement methods [Walm 09]. Namely, the most common techniques used in ultrafast experiments are the frequency resolved optical gating (FROG) [Treb 00] and spectral shearing interferometry for direct electrical field reconstruction (SPIDER) [Iaco 98]. Both types of techniques are based on a non-linear interaction of the pulse under test, having an intrinsic limitation on the sensitivity of the measurement, and hence find appropriate application in high power, low repetition rate femtoseconds pulse trains. In the telecommunication environment, linear versions of both FROG and SPIDER have been proposed by Dorrer et al. [Dorr 02, Dorr 03], allowing the measurement of the instantaneous frequency of pulses with durations ranging from hun-

dreds of femtoseconds to tens of picoseconds and peak amplitudes of hundreds of micro Watts. However, these technique part from the assumption that the temporal intensity is not available, as it is for femtosecond pulses, while in communications applications, where longer pulses are used, a fast photodiode and oscilloscope are often enough. In this context the instantaneous frequency is often referred as the Time Resolved Chirp (TRC) of the pulse. Several technique have been proposed for the TRC measurement, involving spectral [Debe 98, Vill 08] or temporal [Berg 88, Lave 03, Sato 05, Tamm 97] measurements. The work proposed by Bergano et al. [Berg 88], i.e. the frequency discriminator technique, is easily implemented with a variable spectral filter and a fast photodiode and oscilloscope: it is based on filtering the optical signal with a known linear spectral function and obtaining the TRC from the measured pulse intensities.

The *phase reconstruction using optical ultrafast differentiation* (PROUD) method [Li 07, Li 09b] is very similar to the discriminator technique, as it is also based on the spectral filtering and temporal intensity detection of the pulse. The major advantage of PROUD with respect to the discriminator technique is that the formulation of PROUD takes into account the phase of the optical transfer function of the filter, i. e. an optical differentiator.

The implementation of PROUD proposed in this Chapter [Cons 11c, Cons 11b] is based on a birefringent interferometer, acting as the required optical differentiator, which transfer function can be easily changed between two pulse measurements. The pulses generated from a GS DFB laser have been characterized in amplitude and phase, for different modulation condition, measuring the TRC of pulses with different shapes and durations ranging from 100 ps to 800 ps. The pulse spectra are reconstructed from the retrieved phase and measured intensity, allowing the comparison with the independently measured spectra from which an error estimation is obtained.

From the intensity and TRC curves, the linewidth enhancement factor of the DFB laser under study is obtained, using a simple analytic formula. Additionally, the Gerchberg-Saxton algorithm, previously mentioned, is considered for the phase retrieval of the considered pulses. It is shown that the spectral resolution required for a correct phase estimation is limiting the applicability of the algorithm to the considered pulses.

8.2 PROUD technique and experimental set-up

The PROUD technique is based on the acquisition of two temporal intensities, i. e. the original pulse and the differentiated pulse, and the knowledge of the spectral transfer function of the optical differentiator. The measured pulse intensities (original and differentiated) are used to obtain the instantaneous frequency of the original pulse. The general idea of spectral filtering and temporal detection is schematically depicted in Fig. 8.1. By filtering with a linear transfer function the pulse to be measured, the pulse temporal intensity is changed accordingly to its time resolved frequency content. The instantaneous frequency is then recovered performing a simple calculation, using the original and differentiated intensities and the slope of the linear spectral filter.

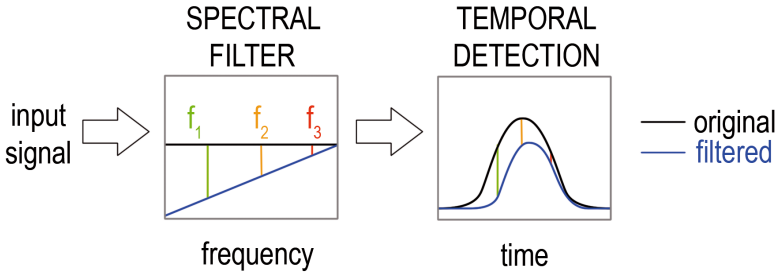

Figure 8.1: Schematic representation of spectral filtering and temporal detection for TRC measurement.

In PROUD, the spectral filtering is obtained with an optical differentiator, which transfer function can be written as $H(\omega) = jA_D(\omega - \Delta\omega)$, where A_D is the differentiator amplitude coefficient, ω is the base-band frequency, and $\Delta\omega = \omega_0 - \omega_R$ is the difference between the signal carrier frequency ω_0 and the differentiator resonance frequency ω_R [Slav 06]. Let $u(t) = \sqrt{P(t)}\exp(j\phi(t))$ be the temporal complex envelope of an optical pulse, with $P(t)$ being the pulse intensity, $\phi(t)$ the pulse phase and $\omega_i(t) = {}^{d\phi(t)}/_{dt}$ the pulse instantaneous frequency. Under the condition $|\Delta\omega| > \omega_i(t)$, the instantaneous frequency of the pulse can be recovered from the pulse intensity $|u(t)|^2$ and the intensity at the differentiator output $|v(t)|^2$, with the following direct expression [Li 07]:

$$\omega_i(t) = \sqrt{\frac{\left(\frac{|v(t)|}{A_D}\right)^2 - \left(\frac{d|u(t)|}{dt}\right)^2}{|u(t)|^2}} - \Delta\omega \tag{8.1}$$

It's worth noting that the condition $|\Delta\omega| > \omega_i(t)$ simply implies that the spectral bandwidth of the input signal is entirely positioned at either side of the differen-

tiator resonance frequency. Then, the pulse phase can be obtained by numerically integrating the instantaneous frequency: $\phi(t) = \int \omega_i(t)dt + \phi_0$, where ϕ_0 is a non relevant constant. A key point of the technique is the requirement of synchronization between the measured intensities $|u(t)|^2$ and $|v(t)|^2$ for the validity of Eq. 8.1. Thus, in previous implementations of PROUD [Li 07, Li 09b], the temporal delay between the input and output of the differentiator was measured and compensated. The proposed implementation avoids the need for time delay compensation, resulting in a significant simplification of the experimental apparatus and procedure. This is achieved by switching the spectral transfer function of the filter in such a way that the differentiator transfer function is used to measure $|v(t)|^2$ and a plain transfer function is used to obtain a signal proportional to $|u(t)|^2$ at the filter output, thus preserving the synchronism.

A schematic of the complete set-up is shown in Fig. 8.2 together with a photograph of its physical implementation. The laser used in the experiments is a commercially available, fiber pigtailed, 2.5 Gb/s, 1540 nm Distributed Feedback (DFB) laser (JDS Uniphase). A polarization controller is used to align the polarization of the GS DFB laser with the fixed linear polarizer. Before entering the interferometer, the signal is amplified by an Erbium Doped Fiber Amplifier (EDFA). The amplifier plays a double role in our experiments: it improves the signal to noise ratio and allows the measurement of the interferometer transfer function by using its Amplified Spontaneous Emission (ASE) as input signal. The output of the interferometer is divided by a 50/50 coupler such that half of the signal is directed to an OSA and half to a fast photodiode and oscilloscope (20 GHz bandwidth).

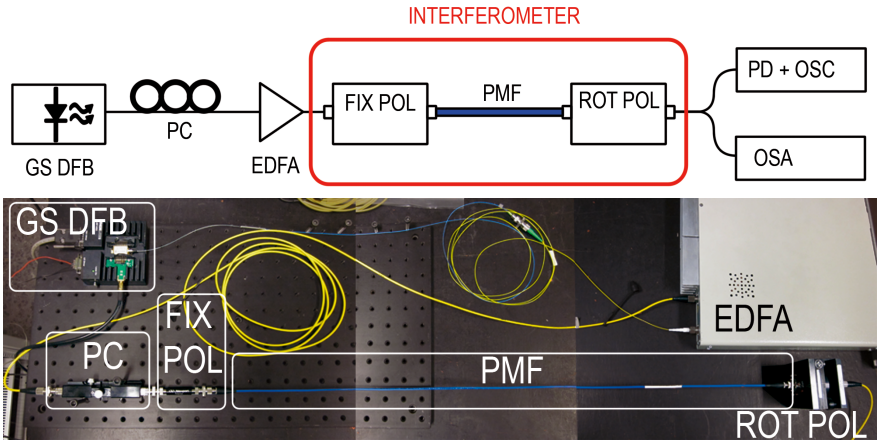

Figure 8.2: Schematic of the set-up: GS DFB laser, polarization controller (PC), EDFA, fixed linear polarizer (FIX POL), Polarization Maintaining Fiber (PMF), rotatable linear polarizer (ROT POL), photodiode (PD), oscilloscope (OSC) and OSA. A photograph of the experimental set-up is also shown.

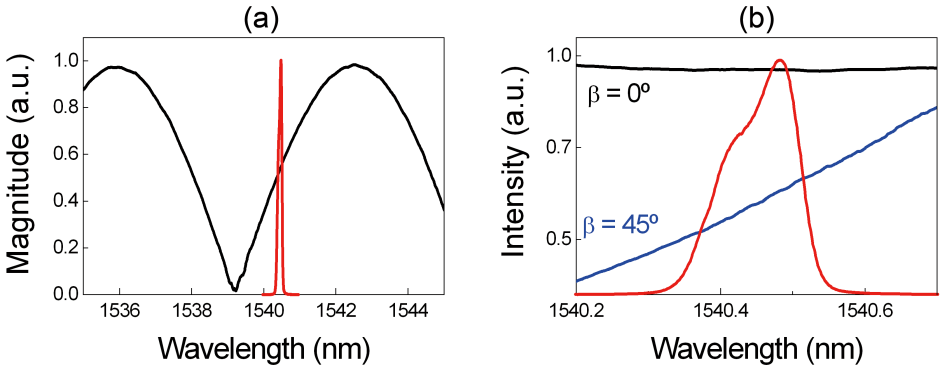

Figure 8.3: (a) Measured magnitude of the interferometer transfer function for $\beta = 45^{\circ}$ (black line) and GS laser spectrum (red line). (b) Measured ASE spectra for $\beta = 0^{\circ}$ (black line) and $\beta = 45^{\circ}$ (blue line) and GS laser spectrum (red line).

The interferometer is based on a birefringent medium and consists of (i) one linear polarizer oriented at 45° with respect to the slow and fast axes of a Polarization Maintaining Fiber (PMF), (ii) the PMF and (iii) a rotatable linear polarizer with variable polarization angle β, measured with respect to the slow axis of the PMF. The two orthogonal components of the light at the exit of the first polarizer travel different optical path lengths in the PMF due to the difference of the effective refractive index of the two axes of the fiber. Thus, the PMF axes act like the two arms of a Mach-Zehnder (MZ) interferometer. The out-coming components along the slow and fast axis of the PMF interfere at the rotatable polarizer with maximum contrast when the polarizer is oriented at 45° with respect to the PMF axes. By rotating the polarizer, the spectral response of the interferometer can be modified, to obtain a plain transfer function when its axis is aligned with the slow or fast axis of the PMF ($\beta = 0^{\circ}$, $\beta = 90^{\circ}$).

Figure 8.3 a) shows the GS laser spectrum, together with the magnitude of the interferometer transfer function as obtained by using the ASE spectrum of the EDFA as input signal and setting the rotatable polarizer with $\beta = 45^{\circ}$. In the described set-up, the PMF length is 90 cm and the measured spectral half period (wavelength spacing between adjacent zeros) of the interferometer is 6.6 nm, corresponding to a temporal delay between the two interferometer arms of 1.2 ps. This value corresponds to a birefringence of $4 \cdot 10^{-4}$, consistent with the specification of the PMF. In the experiments the linear spectral filtering was ensured since the spectral FWHM for the most chirped pulses was 0.16 nm. As it can be observed in Fig. 8.3 a), the condition $|\Delta\omega| > \omega_i(t)$ is fully achieved, and a zero of transmission is not far from to the laser emission wavelength.

The parameters A_D and $\Delta\omega$ of Eq. 8.1 are obtained from the linear fit of the

ratio between the ASE spectra when $\beta = 45^{o}$ (maximum contrast) and $\beta = 0^{o}$ (plain spectrum). Figure 2 b) shows the measured ASE spectrum for $\beta = 0^{o}$ and $\beta = 45^{o}$ and the spectrum of the most chirped pulse in our experiments. The values obtained for A_D and $\Delta\omega$ are 0.78 ps/rad and $1.0{\cdot}10^{12}$ rad/s, respectively.

8.3 Time resolved chirp measurements

The optical pulses were generated with the GS DFB laser through the superposition of a bias current I_{BIAS} and a sinusoidal current with frequency 500 MHz and electrical power 4 dBm. Three values of I_{BIAS} were used, resulting in pulses with different durations and shapes: I_{BIAS} = 13 mA, 16 mA and 20 mA (the laser threshold current is 13.6 mA). Figures 8.4 a), b) and c) show the measured intensities $|u(t)|^2$ and $|v(t)|^2$, and the corresponding instantaneous frequency calculated from Eq. 8.1 for the three pulses. The pulse spectrum was reconstructed from the measured pulse intensity and the recovered phase by means of a discrete Fourier transform algorithm. The measured and reconstructed pulse spectra are shown in Figures 8.4 d), e) and f). The spectral fringes corresponding to the signature of the laser resonance frequency, presented in Chapter 3 and expected in GS lasers, are observed in the reconstructed spectra. The recovered spectra were convoluted with the measured spectral response of the OSA filter (the FWHM is 6.25 GHz), in order to be properly compared with the measured spectra. The three measured pulses show frequency oscillations during the relaxation oscillations at the laser turn-on due to the carrier induced index modulation, as discussed in Chap. 3. By increasing I_{BIAS}, longer pulses and multiple spikes are observed at the output of the laser, producing double and triple peaked pulses.

The pulse obtained with I_{BIAS} = 13 mA, Fig. 8.4 a), has a FWHM duration of 102 ps. Its instantaneous frequency decreases almost linearly along the pulse peak. This negatively chirped character is a consequence of the carrier induced index modulation resulting from the decrease of the carrier density during the first spike of relaxation oscillations. At the maximum pulse intensity, the carrier density crosses its threshold value, and consequently the instantaneous wavelength is that of the laser above threshold (neglecting thermal effects and assuming perfect carrier clamping above threshold). The spectrum of the pulse obtained with I_{BIAS} = 13 mA is shown in Fig. 8.4 d). The pulse spectrum (FWHM $\sim$ 20 GHz) shows an asymmetric profile with a shoulder on the positive frequency side, typical in GS laser pulses [Liu 91, Barr 98]. A very good agreement is obtained when comparing the reconstructed and measured spectra, confirming the validity of the time-resolved

chirp measurements of GS laser pulses.

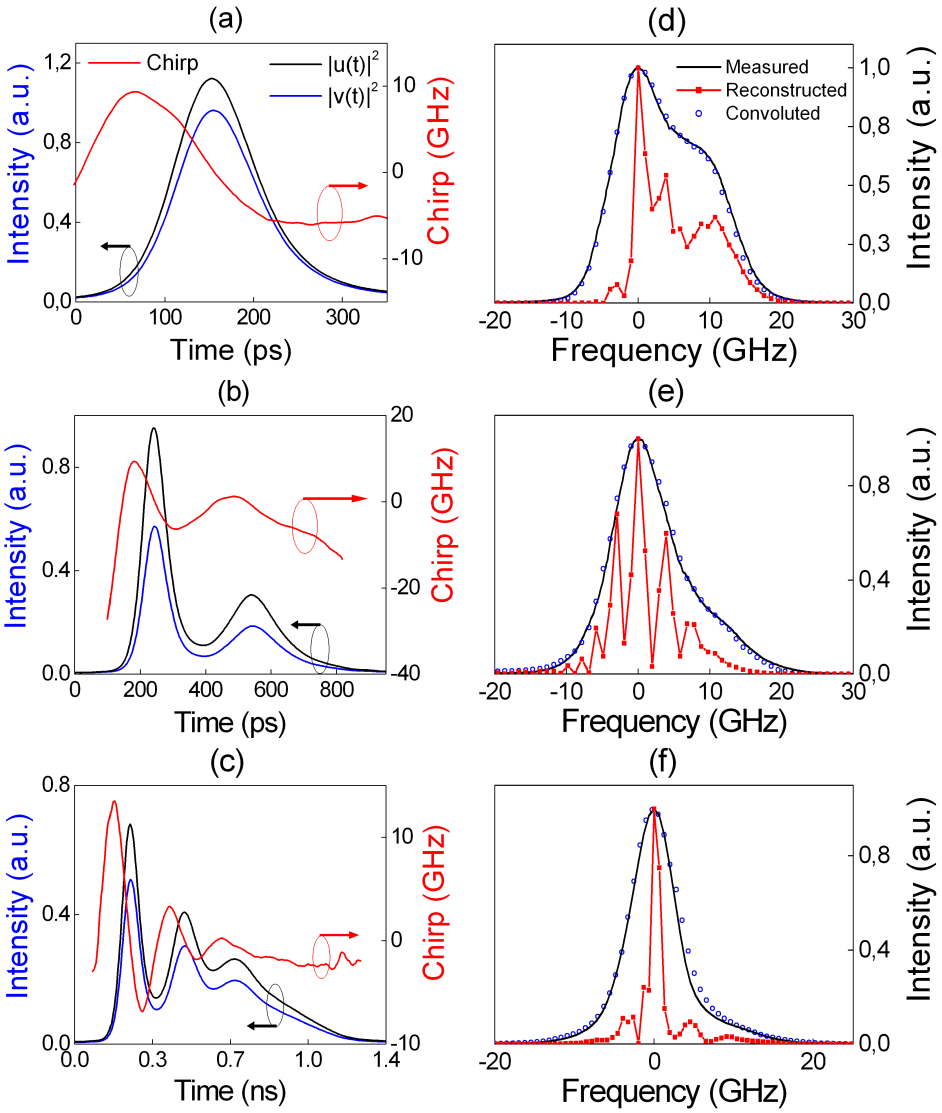

Figure 8.4: Measured pulse intensities $|u(t)|^2$ (left, black lines) and $|v(t)|^2$ (left, blue lines), recovered instantaneous frequency (left, red lines), measured (right, black line), recovered (right, red line) and convoluted spectra (right, blue circles), for I_{BIAS} = 13 mA (top), 16 mA (centre), and 20 mA (bottom).

The pulse in Fig. 8.4 b), obtained for I_{BIAS} = 16 mA, has a total duration of 480 ps (at 13% of the maximum) and shows two intensity peaks with a temporal delay of 300 ps, corresponding to a relaxation oscillation frequency of 3.3 GHz. The recovered spectrum of this pulse has a fringed structure with fringe spacing equal to the inverse of the temporal delay between the two peaks. This fine spectral structure is washed out in the measured and in the recovered convoluted spectra due to the OSA finite resolution, as shown in Fig. 8.4 e).

A triple peaked pulse with total duration of 880 ps (at 13% of the maximum) and

peak spacing of 240 ps is obtained for I_{BIAS} = 20 mA, see Fig. 8.4 c). Increasing I_{BIAS} corresponds to an increase of the relaxation oscillation frequency and thus a reduction of the temporal delay between adjacent pulse spikes. The measured and reconstructed spectra (Fig. 8.4 f) show a more symmetrical profile and smaller spectral width than previous pulses, as a consequence of its longer duration.

8.4 Linewidth enhancement factor measurement

From the pulse intensity and chirp, it's possible to obtain the linewidth enhancement factor (α parameter), considering that the phase-amplitude coupling strength of the laser is expressed through the α parameter. From the analysis of the rate equations reported in [Koch 84], the instantaneous frequency variation $\nu(t)$ can be expressed as a function of the pulse intensity $P(t)$ according to:

$$\nu(t) = \frac{\alpha}{4\pi}\frac{1}{P(t)}\frac{dP(t)}{dt} \tag{8.2}$$

Figure 8.5 (left) shows the simulated intensity and chirp of a GS laser pulse, with typical GS parameters for single peaked pulse generation, obtained with the rate equations model described in Chapter 3. In Fig. 8.5 (right), the chirp is plotted as a function of $\frac{1}{4\pi}\frac{1}{P(t)}\frac{dP(t)}{dt}$, following Eq. 8.2. Neglecting the low intensity points, which are shown for completeness, the value of the α parameter can be calculated with a simple linear regression in the linear region of the graph. The arbitrary value of α = 5, used in the simulation is recovered as the slope of Fig. 8.5 (right).

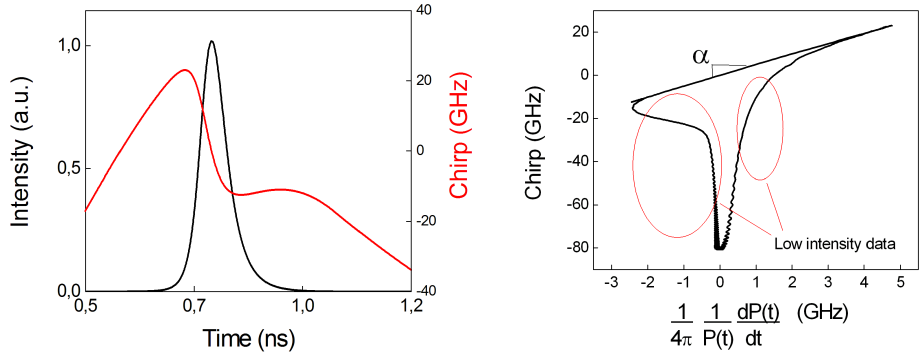

Figure 8.5: Simulation results for the recovery of α parameter from pulse intensity and chirp.

The measured pulse intensity and chirp obtained with I_{BIAS} = 13 mA, shown in Fig. 8.4 a), are used to calculate the linewidth enhancement factor of the DFB laser. The result is plotted in Fig. 8.6, where the linear regression is also shown,

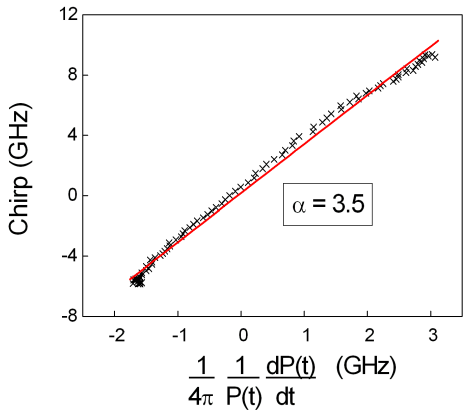

Figure 8.6: Extracted linewidth enhancement factor from the pulse intensity and chirp obtained with $I_{BIAS} = 13$ mA.

obtaining $a = 3.5$, which is a typical value for this type of laser. The low intensity points are omitted for clarity.

The proposed technique for the a parameter measurement is a straight forward extension of the TRC measurement, from which $\nu(t)$ and $P(t)$ are obtained. The main limitation of this method comes from the noise in the pulse intensity measurement, which strongly affects the results in Fig. 8.5 (right), via the derivative of $P(t)$ in Eq. 8.2. This drawback can be overcome by proper design of a numerical high frequency filter, to get rid of the noise component in the intensity measurements, as it has been done for the pulses obtained with our set-up.

8.5 Phase reconstruction with Gerchberg-Saxton Algorithm

At the beginning of this Chapter, the Gerchberg-Saxton algorithm is mentioned and its applicability to the phase retrieval of an optical pulse is presented. This is the case of most optical communication signal, such as the experiments presented, and therefore it is interesting to apply the algorithm and test its efficiency.

The Gerchberg-Saxton algorithm [Gerc 72] is an iterative algorithm for the pulse phase retrieval which uses the temporal and spectral intensities of the pulse. Figure 8.7 shows the conceptual block diagram of the algorithm, which involves four quantities: the temporal and spectral intensities, $P(t)$ and $I_m(\omega)$, respectively, and the temporal and spectral phases, $\phi(t)$ and $\psi(\omega)$, respectively. While the intensities are known, the phases are unknown and its retrieval is the goal of the algorithm. The algorithm consists of an iterative Fourier transformation, from temporal to spectral

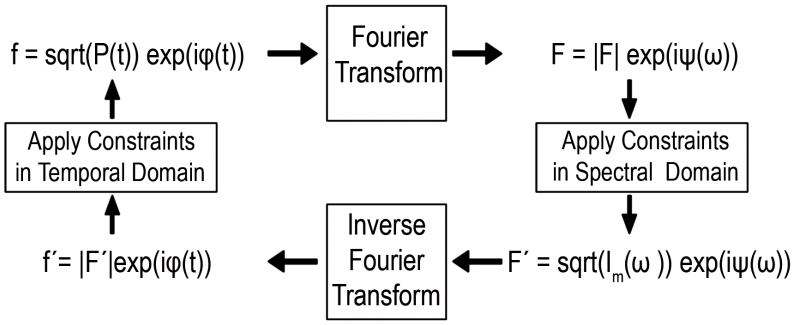

Figure 8.7: The Gerchberg-Saxton algorithm.

domain and backward: at each cycle the phases are left free to change, while the moduli are substituted with the square root of the measured intensities. These are the external constraints that must be imposed for the algorithm to converge.

In practical cases, the pulse spectrum could contain a fine structure, as it happens in GS pulses, that is washed out by the OSA resolution. This is the case of the reconstructed spectra shown in Fig. 8.4 (d),(e),(f) which exhibit the resonance frequency signature discussed in Chapter 3, with spectral fringes spaced about 2 GHz. Considering that the OSA resolution is 6.25 GHz (0.05 nm @ 1550 nm), it is evident how the spectrum fine structure is lost in the measurements.

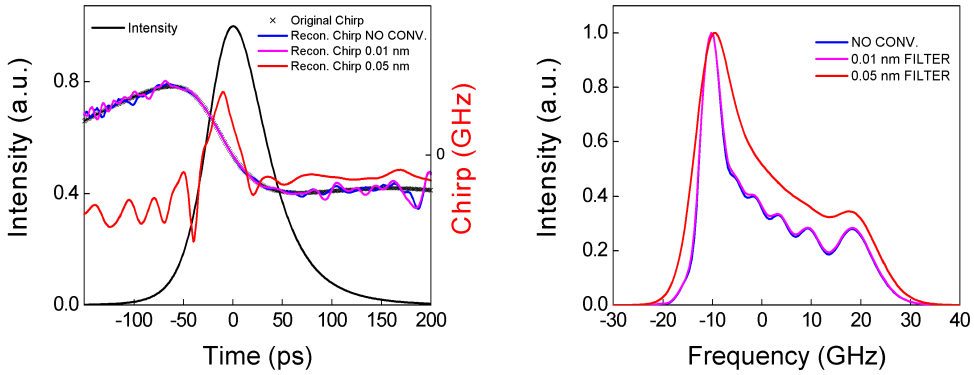

Figure 8.8: Simulated temporal intensity and chirp and reconstructed chirp (right) and convoluted spectrum with different OSA filter bandwidths (left).

The Gerchberg-Saxton algorithm has been implemented and applied to the simulated temporal and spectral pulse intensities obtained from a GS laser. Figure 8.8 shows the effect of the OSA resolution on the reconstructed chirp. Considering the simulated spectrum with no convolution (blue line in Fig. 8.8 right) and convoluted with a narrow 0.01 nm OSA filter, the results from the iterative procedure (blue and magenta lines in Fig. 8.8 left) are very similar to the original pulse chirp (crosses in Fig. 8.8 left), resulting in an efficient reconstruction of the temporal phase. Anyway,

when the OSA filter is set to 0.05 nm, the inefficiency of the procedure in reconstructing the pulse chirp is evident, due to the blurring effect of the filter on the pulse spectrum.

8.6 Accuracy of the proposed technique

The accuracy of the proposed technique for TRC characterization can be estimated from the comparison between the measured and recovered spectra shown in Fig. 8.4 d), e), f). An error parameter is defined as:

$$\epsilon = 100 \cdot \frac{\int |I_m(\omega) - I_r(\omega)| \, d\omega}{\int I_m(\omega) d\omega} \tag{8.3}$$

where $I_m(\omega)$ and $I_r(\omega)$ are the measured and the recovered intensity spectra, respectively, and the integrals extent over the entire pulse spectrum . The values of the error for the three measured pulses in Fig. 8.4 a), b) and c) are 3.9%, 6.3% and 7.1%, respectively. These errors correspond to an uncertainty in the chirp amplitude between 5 and 10 %, as estimated by numerical simulation of the spectra, indicating that the accuracy of the measurement is better than 10%.

This small error indicates that our implementation of PROUD technique is valid for the characterization of pulses generated from GS semiconductor lasers, avoiding the need of a high resolution spectrometer to apply phase reconstructions algorithms. Numerical simulations indicate that a spectral resolution better than 0.01 nm would be required to get similar errors by retrieving the phase from the temporal and spectral intensities. The final resolution of our technique is limited by the signal to noise ratio of the temporal intensities. In our experiments the main source of noise is the timing jitter caused by the stochastic fluctuations of the GS laser turn-on. The TRC results presented here were measured by averaging 150 times the intensity profiles and applying a low pass filter during the data processing to get rid of the high-frequency noise. In comparison with previous implementations of PROUD [Li 07, Li 09b], our technique avoids the need for the compensation of the temporal delay between the input and output pulses.

This implies a reduced set-up and a simplified experimental procedure which only takes a few minutes to perform a complete TRC measurement. The PMF based interferometer has proved to be very stable with ambient temperature fluctuations, due to the fact that the two arms of the interferometer, i.e. the slow and fast axis of the fiber, share the same medium and therefore are affected by the same thermal changes. In comparison with other techniques for the characterization of TRC

[Berg 88, Lave 03, Sato 05, Tamm 97, Vill 08, Debe 98], our procedure is very simple avoiding time consuming sensitive adjustments. In fact, our technique is similar to the discriminator technique proposed in refs. [Berg 88, Lave 03, Sato 05, Tamm 97], which are also based on the measurement of the temporal intensities after filtering the signal with different transfer functions. The main advantage of the PROUD method in comparison with these techniques is that the expression providing the frequency chirp takes into account not only the amplitude of the frequency response of the filter, but also its phase response, which gives rise to the term $\frac{d|u(t)|}{dt}$ in Eq. 8.1. In consequence, it provides a more accurate measurement in the case of low chirped pulses. In addition, our procedure can be implemented making use of standard instrumentation in a photonics laboratory, such as a sampling oscilloscope and an OSA, in addition to common optical components and a low-cost PMF patch-cord. The non-iterative algorithm used in PROUD allows for a very fast determination of the TRC through a simple processing of the measured data.

This technique can be applied to measure pulses of different duration by proper design of the interferometer free spectral range using shorter or longer PMF lengths. The main limitation for the characterization of short pulses (in the range of ps or lower) is the need of a high bandwidth oscilloscope, but this can be overcome by using temporal stretchers, with well known frequency response, to broaden the original pulse [Li 09b]. In addition, the characterization of short pulses at higher data rates will be limited by the degradation of the signal to noise ratio and by the jitter. The proposed implementation of PROUD could be further improved for better performance and alternative applications. A balanced temporal PROUD [Li 09a] can be implemented by replacing the rotatable polarizer in Fig. 8.2 with a polarizing beam splitter, which, when properly aligned with respect to the PMF, would provide two outputs equivalent to the outputs of a conventional MZ interferometer. The temporal difference between the two outputs, measured by means of a balanced photodetector, is proportional to the input intensity and to the frequency chirp. The reduction of jitter and noise achieved with the balanced detection would allow for real-time and single shot TRC measurements. Furthermore, this balanced set-up could be used as demodulator of phase modulated optical signals to recover the instantaneous phase profile, in a similar manner to the balanced PROUD set-up based on a MZ interferometer [Li 09a].

8.7 Conclusions

The implementation of a simple, fiber based set-up for the direct measurement of the TRC in telecommunication optical signals and the linewidth enhancement factor of a semiconductor laser has been proposed and demonstrated. The instantaneous frequency is recovered from the temporal intensity of the pulse after temporal differentiation with a fiber based polarization interferometer, which is implemented with a PMF patch-cord and two linear polarizers. The proposed set-up avoids the temporal delay compensation needed in previously reported implementations of PROUD simplifying the experimental apparatus. As a proof-of-concept the technique has been applied to characterize the TRC of a GS DFB laser emitting at 1540 nm. From the measured intensity and the recovered TRC, the linewidth enhancement factor of the laser has been calculated. The applicability of the Gerchberg-Saxton algorithm is discussed and it is shown that, depending on the laser characteristics and the gain-switching parameters, the required spectral resolution of the measurements can be inadequate. The spectra calculated from the measured intensity and the recovered phase were compared with the measured spectra, indicating that the error in the TRC is lower than 10%. In comparison with other techniques for the complete characterization of optical signals this implementation has clear advantages regarding simplicity and accuracy.

Chapter 9

Conclusions and future work

Conclusions

The conlcusions of this Thesis are summarized as follows:

- An experimental procedure for the characterization and estimation of internal parameters in packaged VCSELs has been developed and it has been applied to 1550 nm Tunnel Junction based VCSELs. The procedure is based on a combination of static and dynamic electrical and optoelectronic measurements. The effect of the TJ on the electrical properties of Long Wavelength VCSELs has been determined. An electrical equivalent circuit has been proposed for the packaged device, including the contribution of electrical parasitics, of the TJ, and the effect of the MQW active region. The latter has been treated considering the interaction between unconfined carriers in the core and confined carriers in the QWs, through the carrier capture/escape model. The effect of the TJ to the device impedance is relevant, as it varies significantly with applied bias, below and above threshold and with frequency: this is a major issue in the design of practical electronic drivers for directly modulated devices. Through the modeling of the MQW active region, the dynamic decay constants of the carriers in the core and in the QWs have been obtained, and it was possible to estimate the recombination coefficients of the InGaAlAs active region. Finally, taking into account the electrical parasitics obtained with the frequency dependent impedance measurements, we have extracted from the modulation response important internal parameters, i.e. differential gain and gain compression factor. The complete set of parameters can be used for modeling the behavior of the device in optical links and for proper design of the electronic driver.

- The pulse properties of a Gain Switched VCSEL emitting at 1550 nm have been investigated, for the first time, as far as we know. The pulses have been characterized in terms of FWHM duration, peak amplitude, timing jitter and Time Bandwidth Product. The dependence of each of these quantities on the GS conditions has been investigated, confirming consolidated results typical of GS lasers. Moreover, the thermal properties of the laser are shown to be fundamental in the limitation of the shortest obtainable pulses with this type of VCSELs. Pulses with different durations, in the range of tens of picoseconds and few milliwatts, can be obtained, with different values of jitter and TBP, depending on the GS conditions. The shortest duration obtained is of 55 ps, at 2 GHz and 3 GHz, whit highly chirped pulses.

- The reduction of the jitter in optically injected GS VCSEL, previously predicted theoretically, has been experimentally demonstrated. The pulse jitter, pulse duration and amplitude have been measured as a function of the injected power and the frequency detuning. Within a range of injection conditions, optical injection can improve the transmission performance of the injected laser, as it produces spectral narrowing and improves the secondary mode suppression ratio. The results indicate that a jitter reduction higher than 70 % in comparison with the free running VCSEL can be obtained at different repetition rates, in agreement with the results of the simulations.

- An OCDMA encoder based on a GS VCSEL emitting at 1550 nm has been designed and implemented. An electrical driving circuit based on a Step Recovery Diode for pulse generation with the GS VCSEL has been developed. The code is obtained with a set of 8 optical delay lines, each of them shifting the GS VCSEL pulse to its temporal position into the code. Our encoder allows the communication of 10 users on the same channel at a bit rate of 20 Mb/s. The proposed encoder presents the advantages of a simple implementation with inexpensive components and it is an efficient solution in those communication environments where a reduced bandwidth for multiple users is required.

- A novel implementation of the PROUD technique has been proposed and its validity and has been demonstrated by measuring the Time Resolved Chirp of pulses generated from a GS DFB laser emitting at 1.55 µm. The novelty of the proposed implementation is that the transfer function of the interferometer can be changed between a plain transfer function and the differentiator transfer function, allowing a reduced set-up and simplified experimental procedure,

with respect to previous realizations of PROUD. The accuracy of our technique is measured by the comparison between the reconstructed and measured pulse spectra. From the intensity and chirp measurements, the α parameter of the DFB laser is extracted, giving a typical value for the considered device. The proposed technique offers a fast and simple method for directly measuring the chirp of an optical signal and the α parameter of semiconductor lasers, making use of ordinary instrumentation in a photonic laboratory.

Future work

- The pulse generated with a GS VCSEL can be compressed, due to their intrinsic chirped nature, by means of two different approaches: by employing a Dispersion Shifted Fiber (DSF) with negative dispersion at 1550 nm or by the design of a adequate Fiber Bragg Grating (FBG). In the latter case, the PROUD technique reported would be helpful for a precise characterization of the pulse TRC.

- Optical injection can be used to control the laser chirp, as it has been demonstrated in similar devices, and in this case it would be interesting to investigate the effect of OI both on the chirp and the jitter. OI can also be extended to case of VCSEL-to-VCSEL injection, that is an interesting solution in practical communication systems, due to the easy integration on the same chip of two VCSELs. It would be also interesting to investigate VCSEL-to-VCSEL OI in non linear regime of injection, such as periodic pulsations in limit cycle and period doubling, for the generation of period adjustable pulse train from two dc devices, thus avoiding the use of fast electronics for high speed pulse generation needed in direct modulation.

- The design of the OCDMA decoder would be relatively easy to obtain by means of a set of complementary optical delay lines for the autocorrelation of the detected signal. This solution has special interest due to the fact that the electronics needed in the decoder would have to satisfy the bit rate of the original signal, 20 Mb/s in the presented system, thus avoiding fast electronics components but still allowing the multi users nature of the OCDMA channel.

- The implementation of PROUD can be upgraded to a real-time, single-shot version with the use of a Polarization Beam Splitter (PBS) in place of the rotatable polarizer and connecting the two orthogonally polarized outputs of the PBS to a balanced photodetector. This corresponds to implement the

previously reported balanced PROUD based on a MZ interferometer, with the advantages of a fiber based birefringent interferometer, such as temperature stability and low cost component as the PMF. A balanced PROUD based on PMF would allow the measurement of the TRC with improved signal to noise ratio at higher data rate than the one reported in this Thesis.

Appendix A

Author's Contributions

List of scientific pubblications

Indexed Peer Reviewed Journals

1. A. Consoli, J. M. Garcia Tijero and I. Esquivias, "Time resolved chirp measurements of gain switched semiconductor laser using a polarization based optical differentiator", Optics Express, 19 (11) 10805-10812 (2011).

2. A. Consoli, I. Esquivias, F. J. L. Hernandez, J. Mulet, and S. Balle, "Characterization of Gain-Switched Pulses From 1.55-µm VCSEL," IEEE Photonics Technology Letters, 22 (11) 772-774 (2010).

International Conferences

1. A. Consoli, J. M. Garcia Tijero, J. Azaña, Y. Park and I. Esquivias "Frequency chirp characterization of a gain-switched semiconductor laser using photonic differentiation based on polarization interferometry" in European Conference on Lasers and Electro-Optics, CLEO Europe 2011, Munich, Germany, 22-26 May (2011).

2. V. Chauhan, P. M. Vaughan, J. Cohen, T. C. Wong, J. Ratner, L. Xu, A. Consoli, and R. Trebino "Using Blind Deconvolution to Simultaneously Retrieve Two Ultrashort Laser Pulses", in Signal Recovery & Synthesis, SRS 2011, Toronto, Canada, July 10-14 (2011).

3. V. Chauhan, J. Cohen, L. Xu, P. Vaughan, A. Consoli, J. Ratner, T. C. Wong and R. Trebino "Double-Blind Frequency-Resolved Optical Gating for Measuring Two Different Pulses Simultaneously" Conference on Lasers and

Electro-Optics, CLEO 2011, paper CtuO4, Baltimore, Maryland, USA 1-6 May (2011).

4. A. Consoli, J. Arias, J. M. Garcia Tijero, F. J. López-Hernández and I. Esquivias "Electrical characterization of long wavelength VCSELs with tunnel junction" in Vertical-Cavity Surface-Emitting Lasers XV, Proceedings of SPIE vol. 7952, 79520C (2011).

5. A. Consoli, V. Chauhan, J. Cohen, L. Xu, P. Vaughan, F. J. López-Hernández and R. Trebino "Retrieving Two Pulses Simultaneously and Robustly Using Double-Blind FROG" in Frontiers in Optics, FIO 2010, paper FThD8, Rochester, New York, USA, 24-28 October (2010).

6. A. Consoli, J. Noriega, A. Valle, L. Pesquera, I. Esquivias, and F. Lopez-Hernandez, "Optical Injection-Induced Timing Jitter Reduction in Gain-Switched Single-Mode Vertical-Cavity Surface-Emitting Lasers," in Semiconductor Lasers and Laser Dynamics IV, Proceedings of SPIE vol. 7720 (2010).

7. A. Consoli, F. J. López-Hernández, P. R. Horche, and C. del Río Campos "Transmission Performance Improvement of Directly Modulated 1.5 µm VCSEL: Simulations and Experiments" in Third International Conference on Advances in Circuits, Electronics and Micro-Electronics, CENICS 2010, Venice, Italy, 18-25 July (2010).

8. A. Consoli, A. Valle, L. Pesquera, I. Esquivias, and F. J. Lopez-Hernandez, "Optical injection-induced timing jitter reduction in gain-switched single-mode 1550 nm-VCSELs" in Conference on Lasers and Electro-Optics, CLEO 09, paper JThE11, Baltimore, Maryland, USA, 31 May - 5 June (2009).

9. A. Consoli, I. Esquivias, F. J. Lopez-Hernandez, S. Balle, and J. Mulet, "Pulse Generation from Gain-Switched Vertical Cavity Surface Emitting Laser at 1.5 µm" in International Conference on Advances in Electronics and Microelectronics, ENICS 08, Valencia, Spain, September 29 - October 4 (2008).

National Conferences

1. A. Consoli, J. M. Garcia Tijero and I. Esquivias "Polarization based optical differentiator for time resolved chirp measurements of gain switched semiconductor lasers" VII Reunión Española de Optoelectrónica, OPTOEL 11, Santander, Spain, 29 June - 01 July (2011).

2. A. Consoli, J. Arias and I. Esquivias "Caracterización Eléctrica de VCSELs de Unión Túnel Emitiendo a 1.55 µm" VII Reunión Española de Optoelectrónica, OPTOEL 11, Santander, Spain, 29 June - 01 July (2011).

3. P. Adamiec, A. Consoli, J. M. Garcia Tijero and I. Esquivias "Simple dynamic model of a two-section tapered laser", VII Reunión Española de Optoelectrónica, OPTOEL 11, Santander, Spain, 29 June - 01 July (2011).

4. A. Consoli, J. M. Noriega, A. Valle, L. Pesquera, I. Esquivias, and F. J. López-Hernández, "Timing jitter reduction in gain-switched single-mode vertical-cavity surface-emitting lasers by optical injection " VI Reunión Española de Optoelectrónica, OPTOEL 09, Malaga, Spain, 15-17 July (2009).

5. A. Consoli, I. Esquivias, and F. J. López-Hernández, "Optical code division multiple access encoder based on gain-switched 1.55 µm vertical cavity surface emitting laser " VI Reunión Española de Optoelectrónica, OPTOEL 09, Malaga, Spain, 15-17 July (2009).

6. A. Consoli, I. Esquivias, and F. J. López-Hernández, "Generación de pulsos opticos a 1.5 µm mediante conmutación de ganancia en láseres de cavidad vertical" in XXIII Simposium Nacional de la Unión Científica Internacional de Radio, URSI 2008, Madrid, Spain, 22-24 September (2008).

Visiting Scholar in Foreigner Research Centers

- February - June 2010. With the Ultra Fast Optics Group at Georgia Institute of Technology, Atlanta, Georgia, USA under the supervision of Prof. Rick Trebino.

Research Projects

- Plan Nacional de I+D+i, TEC2006-13887-C05-01, Proyecto BLANCO "Desarrollo de Técnicas de Banda-Ultra-Ancha Mediante Pulsos Generados por Diodos Láser: Aplicación a las Comunicaciones Ópticas Inalámbricas". Ministerio de Ciencia e Innovación.

- Plan Nacional de I+D+i, TEC2009-14581-C02-01 Proyecto ALAS "Advanced Semiconductor Lasers for All-Optical Signal Processing and Short Pulse Generation". Ministerio de Ciencia e Innovación.

Awards

- Best Paper Award assigned by the International Academy, Research, and Industry Association (IARIA) at Conference on Advances in Circuits, Electronics and Micro-Electronics (CENICS 2010) for the paper "Transmission Performance Improvement of Directly Modulated 1.5 µm VCSEL: Simulations and Experiments".

Appendix B

List of Figures, Tables and Abbreviations

List of Figures

List of Tables

List of Abbreviations

ASE Amplified Spontaneous Emission

DBR Distributed Bragg Reflector

DFB Distributed Feedback

DSF Dispersion Shifted Fiber

EDFA Erbium Doped Fiber Amplifier

EE Edge Emitting

FBG Fiber Bragg Grating

FP Fabry Perot

FWHM Full Width at Half Maximum

GS Gain Switched

LW Long Wavelength

MQW Multi Quantum Well

MR Modulation Response

MZ Mach-Zehnder

OCDMA Optical Code Division Multiple Access

OI Optical Injection

OSA Optical Spectrum Analyzer

P-I-V Power Current Voltage

PBS Polarization Beam Splitter

PMF Polarization Maintaining Fiber

PROUD Phase Reconstruction using Optical Ultrafast Differentiation

QW Quantum Well

RE Rate Equations

SHB Spatial Hole Burning

SMF Single Mode Fiber

SMF Single Mode Fiber

SMSR Side Mode Suppression Ratio

TBP Time Bandwidth Product

TJ Tunnel Junction

TRC Time Resolved Chirp

VCSEL Vertical Cavity Surface Emitting Laser

Bibliography

[Agra 02] G. P. Agrawal. *Fiber-Optic Communication Systems.* John Wiley & Sons, Inc., 2002.

[Aspi 81] G. Aspin, J. Carroll, and R. Plumb. "The effect of cavity length on picosecond pulse generation with highly RF-Modulated modulated AlGaAs double heterostructure lasers". *Applied Physics Letters*, Vol. 39, No. 11, pp. 860–862, 1981.

[Aspi 82] G. J. Aspin and J. E. Carroll. "Gain-Switched Pulse Generation with Semiconductor Lasers". *IEE Proceedings I: Solid State and Electron Devices*, Vol. 129, No. 6, pp. 283–290, 1982.

[Auye 81] J. Auyeung. "Picosecond Optical Pulse Generation at Gigahertz Rates by Direct Modulation of a Semiconductor-Laser". *Applied Physics Letters*, Vol. 38, No. 5, pp. 308–310, 1981.

[Baco 09] A. Bacou, A. Hayat, A. Rissons, V. Iakovlev, A. Syrbu, and J. Mollier. "VCSEL Intrinsic Response Extraction Using T-Matrix Formalism". *IEEE Photonics Technology Letters*, Vol. 21, No. 14, pp. 957–959, 2009.

[Baco 10] A. Bacou, A. Hayat, V. Iakovlev, A. Syrbu, A. Rissons, J.-C. Mollier, and E. Kapon. "Electrical Modeling of Long-Wavelength VCSELs for Intrinsic Parameters Extraction". *IEEE Journal of Quantum Electronics*, Vol. 46, No. 3, pp. 313–322, 2010.

[Barr 98] L. Barry, B. Thomsen, J. Dudley, and J. Harvey. "Characterization of 1.55-mu m pulses from a self-seeded gain-switched Fabry-Perot laser diode using frequency-resolved optical gating". *IEEE Photon. Technol. Lett.*, Vol. 10, No. 7, pp. 935–937, 1998.

[Berg 88] N. S. Bergano. "Wavelength discriminator method for measuring dynamic chirp in DFB lasers". *Electronics Letters*, Vol. 24, No. 20, pp. 1296–1297, 1988.

[Besl 88] P. J. Besl. "Active, optical range imaging sensors". *Machine Vision and Applications*, Vol. 1, No. 2, pp. 127–152, 1988.

[Bimb 84] D. Bimberg, K. Ketterer, H. E. Scholl, and H. P. Vollmer. "Generation of 4 ps Light Pulses from Directly Modulated V-Groove Lasers". *Electronics Letters*, Vol. 20, No. 8, pp. 343–345, 1984.

[Bouc 99] J. Boucart, C. Starck, F. Gaborit, A. Plais, N. Bouche, E. Derouin, L. Goldstein, C. Fortin, D. Carpentier, P. Salet, F. Brillouet, and J. Jacquet. "1-mW CW-RT monolithic VCSEL at 1.55 μm". *IEEE Photonics Technology Letters*, Vol. 11, No. 6, pp. 629–631, 1999.

[Chan 00] C. Chang-Hasnain. "Tunable VCSEL". *IEEE Journal on Selected Topics in Quantum Electronics*, Vol. 6, No. 6, pp. 978–987, 2000.

[Chan 08] C. J. Chang-Hasnain and X. Zhao. "Ultrahigh-speed laser modulation by injection locking". In: *Optical Fiber Telecommunications V, A: Components and Subsystems, Volume 1*, Chap. 6, p. 931, Academic Press Elsevier, 2008.

[Chan 91] C. J. Chang-Hasnain, J. P. Harbison, G. Hasnain, A. C. V. Lehmen, L. T. Florez, and N. G. Stoffel. "Dynamic, polarization, and transverse mode characteristics of vertical cavity surface emitting lasers". *IEEE Journal of Quantum Electronics*, Vol. 27, No. 6, pp. 1402–1409, 1991.

[Chen 07] C. Chen, N. H. Zhu, S. J. Zhang, and Y. Liu. "Characterization of Parasitics in TO-Packaged High-Speed Laser Modules". *IEEE Transactions on Advanced Packaging*, Vol. 30, No. 1, pp. 97–103, 2007.

[Chro 07] L. Chrostowski, B. Faraji, W. Hofmann, M. Amann, S. Wieczorek, and W. Chow. "40 GHz Bandwidth and 64 GHz Resonance Frequency in Injection-Locked 1.55 mum VCSELs". *IEEE Journal of Selected Topics in Quantum Electronics*, Vol. 13, No. 5, pp. 1200–1208, 2007.

[Cold 95] L. A. Coldren and S. W. Corzine. *Diode Lasers and Photonic Integrated Circuits*. John Wiley & Sons, Inc., 1995.

[Cons 08] A. Consoli, I. Esquivias, F. Lopez-Hernandez, S. Balle, and J. Mulet. "Pulse Generation from Gain-Switched Vertical Cavity Surface Emitting Laser at 1.5 μm". In: *International Conference on Advances in Electronics and Micro-electronics, ENICS '08*, pp. 72–77, 2008.

[Cons 09a] A. Consoli, F. J. Lopez-Hernandez, and I. Esquivias. "Optical Code Division Multiple Access Encoder based on gain-switched 1.55 *mu*m Vertical Cavity Surface Emitting Laser". In: *VI Reunión Española de Optoelectrónica, OPTOEL 09*, 2009.

[Cons 09b] A. Consoli, J. Noriega, A. V. L. Pesquera, I. Esquivias, and F. Lopez-Hernandez. "Timing Jitter Reduction in Gain-Switched Single-Mode Vertical-Cavity Surface-Emitting Lasers by Optical Injection". In: *VI Reunión Española de Optoelectrónica, OPTOEL 09*, 2009.

[Cons 09c] A. Consoli, A. V. L. Pesquera, I. Esquivias, and F. Lopez-Hernandez. "Optical injection-induced timing jitter reduction in gain-switched single-mode 1550 nm-VCSELs". In: *Lasers and Electro-Optics, 2009 and 2009 Conference on Quantum electronics and Laser Science Conference. CLEO/QELS 2009. Conference on*, 2009.

[Cons 10a] A. Consoli, I. Esquivias, F. Hernandez, J. Mulet, and S. Balle. "Characterization of Gain-Switched Pulses From 1.55-μm VCSEL". *IEEE Photonics Technology Letters*, Vol. 22, No. 11, pp. 772–774, 2010.

[Cons 10b] A. Consoli, J. Noriega, A. V. L. Pesquera, I. Esquivias, and F. Lopez-Hernandez. "Optical Injection-Induced Timing Jitter Reduction in Gain-Switched Single-Mode Vertical-Cavity Surface-Emitting Lasers". In: *Semiconductor Lasers and Laser Dynamics IV, Proceedings of SPIE*, 2010.

[Cons 11a] A. Consoli, J. Arias, J. M. Tijero, F. J. L. Hernández, and I. Esquivias. "Electrical characterization of long wavelength VCSELs with tunnel junction". In: *Vertical-Cavity Surface-Emitting Lasers XV, Proceedings of SPIE*, 2011.

[Cons 11b] A. Consoli, J. M. Tijero, and I. Esquivias. "Time resolved chirp measurements of gain switched semiconductor laser using a polarization based optical differentiator". *Optics Express*, Vol. 19, No. 11, pp. 10805–10812, 2011.

[Cons 11c] A. Consoli, J. M. G. Tijero, J. Azaña, Y. Park, and I. Esquivias. "Frequency chirp characterization of a gain-switched semiconductor laser using photonic differentiation based on polarization interferometry". In: *Conference on Lasers and Electro-Optics, 2011 CLEO Europe 2011*, 2011.

[Debe 98] J. Debeau, B. Kowalski, and R. Boittin. "Simple method for the complete characterization of an optical pulse". *Optics Letters*, Vol. 23, No. 22, pp. 1784–1786, 1998.

[Dema 70] T. A. Demassa and D. P. Knott. "Prediction of tunnel diode voltage-current characteristics". *Solid-State Electronics*, Vol. 13, No. 2, pp. 131–138, 1970.

[Dorr 02] C. Dorrer and I. Kang. "Simultaneous temporal characterization of telecommunication optical pulses and modulators by use of spectrograms". *Optics Letters*, Vol. 27, No. 15, pp. 1315–1317, 2002.

[Dorr 03] C. Dorrer and I. Kang. "Highly sensitive direct characterization of femtosecond pulses by electro-optic spectral shearing interferometry". *Optics Letters*, Vol. 28, No. 6, pp. 477–479, 2003.

[Elis 05] P. G. Eliseev, P. Adamiec, A. Bercha, F. Dybala, R. Bohdan, and W. A. Trzeciakowski. "Anomalous Differential Resistance Change at the Oscillation Threshold in Quantum-Well Laser Diodes". *IEEE Journal of Quantum Electronics*, Vol. 41, No. 1, pp. 9–14, 2005.

[Elli 83] R. A. Elliott, D. X. Huang, R. K. Defreez, J. M. Hunt, and P. G. Rickman. "Picosecond Optical Pulse Generation by Impulse Train Current Modulation of a Semiconductor-Laser". *Applied Physics Letters*, Vol. 42, No. 12, pp. 1012–1014, 1983.

[Esak 74] L. Esaki. "Long Journey into Tunneling". *Proceedings of the IEEE*, Vol. 62, No. 6, pp. 825–831, 1974.

[Esqu 99] I. Esquivias, S. Weisser, B. Romero, J. Ralston, and J. Rosenzweig. "Carrier dynamics and microwave characteristics of GaAs-based quantum-well lasers". *IEEE Journal of Quantum Electronics*, Vol. 35, No. 4, pp. 635–646, 1999.

[Fien 82] J. R. Fienup. "Phase retrieval algorithms: a comparison". *Applied Optics*, Vol. 21, No. 15, pp. 2758–2769, 1982.

[Gatt 09] A. Gatto, A. Boletti, P. Boffi, and M. Martinelli. "Adjustable-chirp VCSEL-to-VCSEL injection locking for 10-Gb/s transmission at 1.55 μm". *Optics Express*, Vol. 17, No. 24, pp. 21748–21753, 2009.

[Geel 90] R. S. Geels and L. A. Coldren. "Submilliamp threshold vertical-cavity laser diodes". *Applied Physics Letters*, Vol. 57, No. 16, pp. 1605–1607, 1990.

[Gerc 72] R. W. Gerchberg and W. O. Saxton. "A practical algorithm for the determination of the phase from image and diffraction plane pictures". *Optik*, Vol. 35, No. -, pp. 237–246, 1972.

[Ghos 10] S. P. Ghosh and A. K. Chakraborty. *Network Analysis and Synthesis*. Tata McGraw Hill, 2010.

[Gibb 96] P. Gibbon and E. Förster. "Short-pulse laser-plasma interactions". *Plasma Physics and Controlled Fusion*, Vol. 38, No. 6, pp. 769–793, 1996.

[Grab 91] A. Grabmaier, A. Hangleiter, G. Fuchs, J. E. A. Whiteaway, and R. W. Glen. "Low nonlinear gain in InGaAs/InGaAlAs separate confinement multiquantum well lasers". *Applied Physics Letters*, Vol. 59, No. 23, pp. 3024–3026, 1991.

[Grab 98] M. Grabherr, R. Jager, M. Miller, C. Thalmaier, J. Herlein, R. Michalzik, and K. Ebeling. "Bottom-emitting VCSEL's for high-CW optical output power". *IEEE Photonics Technology Letters*, Vol. 10, No. 8, pp. 1061–1063, 1998.

[Guig 07] C. Guignard, P. Anandarajah, A. Clarke, L. Barry, O. Vaudel, and P. Besnard. "Experimental investigation of the impact of optical injection on vital parameters of a gain-switched pulse source". *Optical Communications*, Vol. 277, No. 1, pp. 150–155, 2007.

[Hard 90] C. S. Harder, B. J. V. Zeghbroeck, M. P. Kesler, H. P. Meier, P. Vettiger, D. J. Webb, and P. Wolf. "High-speed GaAs/AlGaAs optoelectronic devices for computer applications". *IBM Journal of Research and Development*, Vol. 34, No. 4, pp. 568–584, 1990.

[HARO] *HAROLD Simulation Software*.

[Hasn 92] G. Hasnain, J. M. Wiesenfeld, T. C. Damen, J. Shah, J. D. Wynn, Y. H. Wang, and A. Y. Cho. "Electrically Gain-Switched Vertical-Cavity Surface-Emitting Lasers". *IEEE Photonics Technology Letters*, Vol. 4, No. 1, pp. 6–9, JAN 1992.

[Haya 09] A. Hayat, A. Bacou, A. Rissons, J.-C. Mollier, V. Iakovlev, A. Sirbu, and E. Kapon. "Long Wavelength VCSEL-by-VCSEL Optical Injection Locking". *IEEE Transactions on Microwave Theory and Techniques*, Vol. 57, No. 7, pp. 1850–1858, 2009.

[Hend 97] R. F. M. Hendriks, M. P. van Exter, J. P. Woerdman, A. van Geelen, L. Weegels, K. H. Gulden, and M. Moser. "Electro-optic birefringence in semiconductor vertical-cavity lasers". *Applied Physics Letters*, Vol. 71, No. 18, pp. 2599–2601, 1997.

[Henr 82] C. H. Henry. "Theory of the Linewidth of Semiconductor Lasers". *IEEE Journal of Quantum Electronics*, Vol. 18, No. 2, pp. 259–264, 1982.

[Hern 09] O. G. Hernández, J. A. M. González, E. P. Valdés, F. J. L. Hernández, and R. P. Jiménez. "Adaptive code-division multiple-access system for communications over indoor wireless optical channels based on random optical codes". *IET Optoelectronics*, Vol. 3, No. 4, pp. 187–196, 2009.

[Hofm 11] W. Hofmann, M. Müller, P. Wolf, A. Mutig, T. Gründl, G. Böhm, D. Bimberg, and M. C. Amann. "40 Gbit/s modulation of 1550 nm VCSEL". *Electronics Letters*, Vol. 47, No. 4, p. 270, 2011.

[Houl 05] T. Houle, J. Yong, C. Marinelli, S. Yu, J. Rorison, and I. White. "Characterization of the temperature sensitivity of gain and recombination mechanisms in 1.3-μm AlGaInAs MQW lasers". *IEEE Journal of Quantum Electronics*, Vol. 41, No. 2, pp. 132–139, 2005.

[Hui 91] R. Hui, A. Dottavi, A. Mecozzi, and P. Spano. "Injection Locking in Distributed Feedback Semiconductor Lasers". *IEEE Journal of Quantum Electronics*, Vol. 27, No. 6, pp. 1688–1695, 1991.

[Hurt 09] A. Hurtado, D. Labukhin, I. D. Henning, and M. J. Adams. "Injection Locking Bandwidth in 1550-nm VCSELs Subject to Parallel and Orthogonal Optical Injection". *IEEE Journal of Selected Topics in Quantum Electronics*, Vol. 15; 15, No. 3, pp. 585–593, 2009.

[Iaco 98] C. Iaconis and I. A. Walmsley. "Spectral phase interferometry for direct electric-field reconstruction of ultrashort optical pulses". *Optics Letters*, Vol. 23, No. 10, pp. 792–794, 1998.

[Jin 00] X. Jin and S. L. Chuang. "Relative intensity noise characteristics of injection-locked semiconductor lasers". *Applied Physics Letters*, Vol. 77, No. 9, pp. 1250–1252, 2000.

[Joyc 75] W. Joyce and R. Dixon. "Thermal resistance of heterostructure lasers". *Journal of Applied Physics*, Vol. 46, No. 2, pp. 855–862, 1975.

[Joyc 78] W. Joyce and R. W. Dixon. "Electrical characterization of heterostructure lasers". *Journal of Applied Physics*, Vol. 49, No. 7, pp. 3719–3728, 1978.

[Kan 92] S. C. Kan and K. Lau. "Intrinsic Equivalent Circuit of Quantum - Well Lasers". *IEEE Photonics Technology Letters*, Vol. 4, No. 6, pp. 528–530, 1992.

[Kari 90] J. R. Karin, L. G. Melcer, R. Nagarajan, J. E. Bowers, S. W. Corzine, P. A. Morton, R. S. Geels, and L. A. Coldren. "Generation of picosecond pulses with a gain-switched GaAs surface-emitting laser". *Applied Physics Letters*, Vol. 57, No. 10, pp. 963–965, 1990.

[Katz 81] J. Katz, S. Margalit, C. Harder, D. Wilt, and A. Yariv. "The intrinsic electrical equivalent circuit of a laser diode". *IEEE Journal of Quantum Electronics*, Vol. 17, No. 1, pp. 4–7, 1981.

[Kawa 06] H. Kawaguchi, T. Mori, Y. Sato, and Y. Yamayoshi. "Optical buffer memory using polarization-bistable vertical-cavity surface-emitting lasers". *Japanese Journal of Applied Physics*, Vol. 45, No. 33-36, pp. L894–L897, 2006.

[Koba 80] S. Kobayashi and T. Kimura. "Coherence on injection phase-locked AlGaAs semiconductor laser". *Electronics Letters*, Vol. 16, No. 17, pp. 668–670, 1980.

[Koch 84] T. L. Koch and J. E. Bowers. "Nature of wavelength chirping in directly modulated semiconductor lasers". *Ele*, Vol. 20, No. 25, pp. 1038–1040, 1984.

[Koiz 09] K. Koizumi, M. Yoshida, and M. Nakazawa. "10-GHz 11.5-ps Pulse Generation From a Single-Mode Gain-Switched InGaAs VCSEL at 1.1 *mu*m". *IEEE Photonics Technology Letters*, Vol. 21, No. 22, pp. 1704–1706, 2009.

[Koya 06] F. Koyama. "Recent Advances of VCSEL Photonics". *Journal of Lightwave Technology*, Vol. 24, No. 12, pp. 4502–4513, 2006.

[Lang 82] R. Lang. "Injection locking properties of a semiconductor laser". *IEEE Journal of Quantum Electronics*, Vol. 18, No. 6, pp. 976–983, 1982.

[Lau 88] K. Y. Lau. "Gain switching of semiconductor injection lasers". *Applied Physics Letters*, Vol. 52, No. 4, pp. 257–259, JAN 25 1988.

[Lave 03] C. Laverdiere, A. Fekecs, and M. Tetu. "A new method for measuring time-resolved frequency chirp of high bit rate sources". *IEEE Photonics Technology Letters*, Vol. 15, No. 3, pp. 446–448, 2003.

[Lee 89] Y. Lee, J. Jewell, A. Scherer, S. McCall, J. Harbison, and L. Florez. "Room-temperature continuous-wave vertical-cavity single-quantum-well microlaser diodes". *Electronics Letters*, Vol. 25, No. 20, pp. 1377–1378, 1989.

[Li 07] F. Li, Y. Park, and J. Azaña. "Complete temporal pulse characterization based on phase reconstruction using optical ultrafast differentiation (PROUD)". *Optics Letters*, Vol. 32, No. 22, pp. 3364–3366, 2007.

[Li 09a] F. Li, Y. Park, and J. Azaña. "Single-shot real-time frequency chirp characterization of telecommunication optical signals based on balanced temporal optical differentiation". *Optics Express*, Vol. 34, No. 18, pp. 2742–2744, 2009.

[Li 09b] F. Li, Y. Park, and J. Azana. "Linear Characterization of Optical Pulses With Durations Ranging From the Picosecond to the Nanosecond Regime Using Ultrafast Photonic Differentiation". *Journal of Lightwave Technology*, Vol. 27, No. 21, pp. 4623–4633, 2009.

[Lin 80] C. Lin, P. L. Liu, T. C. Damen, D. J. Eilenberger, and R. L. Hartman. "Simple Picosecond Pulse Generation Scheme for Injection-Lasers". *Electronics Letters*, Vol. 16, No. 15, pp. 600–602, 1980.

[Lin 84a] C. Lin and F. Mengel. "Reduction of frequency chirping and dynamic linewidth in high-speed directly modulated semiconductor lasers by injection locking". *Electronics Letters*, Vol. 20, No. 25, pp. 1073–1075, 1984.

[Lin 84b] C. L. Lin, C. A. Burrus, G. Eisenstein, R. S. Tucker, P. Besomi, and R. J. Nelson. "11.2 Ghz Picosecond Optical Pulse Generation in Gain-Switched Short-Cavity Ingaasp Injection-Lasers by High-Frequency Direct Modulation". *Electronics Letters*, Vol. 20, No. 6, pp. 238–240, 1984.

[Lin 85] C. Lin and J. E. Bowers. "Measurement of 1.3 and 1.5 *mu*m Gain-Switched Semiconductor Laser Pulses with a Picosecond IR Streak Camera and a High-Speed InGaAs PIN Photodiode". *Electronics Letters*, Vol. 21, No. 25-26, pp. 1200–1202, 1985.

[Lin 91] J. Lin, J. K. Gamelin, S. Wang, M. Hong, and J. P. Mannaerts. "Short pulse generation by electrical gain switching of vertical cavity surface emitting laser". *Electronics Letters*, Vol. 27, No. 21, pp. 1956–1958, 1991.

[Liu 01] G. Liu and S. L. Chuang. "High-Speed Modulation of Long-Wavelength In1-x$Ga_xAs_yP_($1 − y) and In$_($1 − x − y)Ga_xAl_yAs Strained Quantum-Well Lasers". *IEEE Journal of Quantum Electronics*, Vol. 37, No. 10, pp. 1283–1291, 2001.

[Liu 81] P. L. Liu, C. Lin, I. P. Kaminow, and J. J. Hsieh. "Picosecond Pulse Generation from InGaAsP Lasers at 1.25 and 1.3 μm by Electrical Pulse Pumping". *IEEE Journal of Quantum Electronics*, Vol. 17, No. 5, pp. 671–674, 1981.

[Liu 89] H. F. Liu, M. Fukazawa, Y. Kawai, and T. Kamiya. "Gain-Switched Picosecond Pulse (Less-than 10 ps) Generation from 1.3 *mu*m InGaAsP Laser-Diodes". *IEEE Journal of Quantum Electronics*, Vol. 25, No. 6, pp. 1417–1425, JUN 1989.

[Liu 91] H. Liu, Y. Ogawa, and S. Oshiba. "Generation of an extremely short single mode pulse (2 ps) by fiber compression of a gain-switched pulse from a 1.3 μm distribuited feedback laser diode". *Applied Physics Letters*, Vol. 59, No. 11, p. 1284, 09/09 1991.

[Liu 97] J. M. Liu, H. F. Chen, X. J. Meng, and T. B. Simpson. "Modulation bandwidth, noise, and stability of a semiconductor laser subject to

strong injection locking". *IEEE Photonics Technology Letters*, Vol. 9, No. 10, pp. 1325–1327, 1997.

[Mann 81] J. S. Manning. "Thermal impedance of diode lasers - Comparison of experimental methods and a theoretical model". *Journal of Applied Physics*, Vol. 52, No. 5, pp. 3179–3184, 1981.

[Mart 09] J. A. Martinez-Gonzalez, E. Poves, and F. J. Lopez-Hernandez. "Random optical codes used in optical networks". *Communications of the Institution of Engineering and Technology*, Vol. 3, No. 8, pp. 1392–1401, 2009.

[Mats 98] Y. Matsui, H. Murai, S. Arahira, Y. Ogawa, and A. Suzuki. "Enhanced Modulation Bandwidth for Strain-Compensated InGaAlAs-InGaAsP MQW Lasers". *IEEE Journal of Quantum Electronics*, Vol. 34, No. 10, pp. 1970–1978, 1998.

[Medi 11] M. F. G. Medina, B. R. Guillama, O. González, J. A. M. González, E. Poves, and F. J. L. Hernández. "Experimental optical code-division multiple access system for visible light communications". In: *IEEE Wireless Telecommunications Symposium*, 2011.

[Meht 06] M. Mehta, D. Feezell, D. A. Buell, A. W. Jackson, L. A. Coldren, and J. E. Bowers. "Electrical Design Optimization of Single-Mode Tunnel-Junction-Based Long-Wavelength VCSELs". *IEEE Journal of Quantum Electronics*, Vol. 42, No. 7, pp. 675–682, 2006.

[Meln 65] I. Melngailis. "Longitudinal injection-plasma laser of InSb". *Applied Physics Letters*, Vol. 6, No. 3, pp. 59–60, 1965.

[Mend 06] W. Mendenhall and T. Sincich. *Statistics for Engineering and the Sciences*. Prentice-Hall, 2006.

[Minc 99] J. Minch, S. Park, T. Keating, and S. Chuang. "Theory and experiment of In1-xGaxAsyP1-y and In1-x-yGaxAlyAs long-wavelength strained quantum-well lasers". *IEEE Journal of Quantum Electronics*, Vol. 35, No. 5, pp. 771–782, 1999.

[Momm 96] C. Momma, B. N. Chichkov, S. Nolte, F. von Alvenslebe, A. Tiinnermann, H. Welling, and B. Wellegehausen. "Short-pulse laser ablation of solid targets". *Optics Communications*, Vol. 129, No. 1, pp. 134–142, 1996.

[Mori 79] M. Morishita, T. Ohmi, and J. Nishizawa. "Impedance Characteristics Of Double-Hetero Structure Laser-Diodes". *Solid-State Electronics*, Vol. 22, No. 11, pp. 951–962, 1979.

[Mote 82] Y. Motegi, H. Soda, and K. Iga. "Surface-emitting GaInAsP/InP injection laser with short cavity length". *Electronics Letters*, Vol. 18, No. 11, pp. 461–463, 1982.

[Mull 09] M. Muller, W. Hofmann, G. Böhm, and M.-C. Amann. "Short-cavity long-wavelength VCSELs with modulation bandwidths in excess of 15 GHz". *IEEE Photonics Technology Letters*, Vol. 21, No. 21, pp. 1615–1617, 2009.

[Naka 07] M. Nakazawa, H. Hasegawa, and Y. Oikawa. "10-GHz 8.7-ps pulse generation from a single-mode gain-switched AlGaAsVCSEL at 850 nm". *IEEE Photonics Technology Letters*, Vol. 19, No. 16, pp. 1251–1253, JUL-AUG 2007.

[Naka 90] M. Nakazawa, K. Suzuki, and E. Yamada. "Femtosecond Optical Pulse Generation using a Distributed-Feedback Laser Diode". *Electronics Letters*, Vol. 26, No. 24, pp. 2038–2040, NOV 22 1990.

[Nori 08] J. M. Noriega, A. Valle, and L. Pesquera. "Timing jitter reduction in gain-switched VCSELs induced by external optical injection". *Optical and Quantum Electronics*, Vol. 40, No. 2, pp. 119–129, 2008.

[Ohts 05] J. Ohtsubo. *Semiconductor Lasers. Stability, instability and chaos.* Springer, 2005.

[Olss 85] N. A. Olsson, H. Temkin, R. A. Logan, L. F. Johnson, G. J. Dolan, J. P. van der Ziel, and J. C. Campbell. "Chirp-free transmission over 82.5 km of single mode fibers at 2 Gbit/s with injection locked DFB semiconductor lasers". *Journal of Lightwave Technology*, Vol. 3, No. 1, pp. 63–66, 1985.

[Pack 84] H. Packard. "Pulse and waveform generation with Step Recovery Diodes". Tech. Rep., Hewlett Packard, 1984.

[Paol 76] T. L. Paoli and P. A. Barnes. "Saturation of Junction Voltage in Stripe-Geometry (AlGa)As Double-Heterostructure Junction Lasers". *Applied Physics Letters*, Vol. 28, No. 12, pp. 714–716, 1976.

[Park 06] M. Park, O. Kwon, W. Han, K. Lee, S. Park, and B. Yoo. "All-monolithic 1.55 mu m InAlGaAs/InP vertical cavity surface emitting lasers grown by metal organic chemical vapor deposition". *Japanese Journal of Applied Physics*, Vol. 45, No. 1-3, p. L8, 2006.

[Paul 88] P. Paulus, R. Langenhorst, and D. Jager. "Generation and Optimum Control of Picosecond Optical Pulses from Gain-Switched Semiconductor-Lasers". *IEEE Journal of Quantum Electronics*, Vol. 24, No. 8, pp. 1519–1523, AUG 1988.

[Pepe 93a] P. Pepeljugoski, J. Lin, J. Gamelin, M. Hong, and K. Y. Lau. "Ultralow timing jitter in electrically gain-switched vertical cavity surface emitting lasers". *Applied Physics Letters*, Vol. 62, No. 14, pp. 1588–1590, 1993.

[Pepe 93b] P. K. Pepeljugoski, D. M. Cutrer, and K. Lau. "Parametric dependence of timing jitter in gain-switched semiconductor lasers". *Applied Physics Letters*, Vol. 63, No. 26, p. 3556, 12/27 1993.

[Pepe 94] P. Pepeljugoski, D. Cutter, and K. Lau. "3.4ps wide compressed optical pulses from electrically gain-switched vertical cavity surface emitting laser". *Electronics Letters*, Vol. 30, No. 6, pp. 491–492, 1994.

[Pruc 06] P. Prucnal. *Optical Code Division Multiple Access: Fundamentals and Applications*. Taylor and Francis, 2006.

[Pruc 86] P. R. Prucnal, M. A. Santoro, and T. R. Fan. "Spread Spectrum Fiber-optic Local Area Network Using Optical Processing". *Journal of Lightwave Technology*, Vol. 4, No. 5, pp. 547–554, 1986.

[Rayc 09] L. Raycan Co. "Private Communication". 2009.

[Rome 00] B. Romero, J. Arias, I. Esquivias, and M. Cada. "Simple model for calculating the ratio of the carrier capture and escape times in quantum-well lasers". *Applied Physics Letters*, Vol. 76, No. 12, pp. 1504–1506, MAR 20 2000.

[Sato 05] K. Sato, S. Kuwahara, and Y. Miyamoto. "Chirp characteristics of 40-gb/s directly Modulated distributed-feedback laser diodes". *Journal of Lightwave Technology*, Vol. 23, No. 11, pp. 3790–3797, 2005.

[Scot 94] J. Scott, B. Thibeault, D. Young, L. Coldren, and F. Peters. "High efficiency submilliamp vertical cavity lasers with intracavity contacts". *IEEE Photonics Technology Letters*, Vol. 6, No. 6, pp. 678–680, 1994.

[Shim 95] H. Shimizu, T. Fukushima, K. Nishikata, Y. Hirayama, and M. Irikawa. "1.5 μm wavelength compressively strained GaInAs/AlGaInAs multiquantum-well lasers grown by molecular-beam epitaxy with high differential gain and low threshold current density". *Applied Physics Letters*, Vol. 67, No. 4, pp. 449–451, 1995.

[Shin 02] J. H. Shin, B. S. Yoo, W. S. Han, O. K. Kwon, Y. G. Ju, and J. H. Lee. "CW operation and threshold characteristics of all-monolithic InAlGaAs 1.55 μm VCSELs grown by MOCV". *IEEE Photonics Technology Letters*, Vol. 14, No. 8, pp. 1031–1033, 2002.

[Shte 95] G. Shtengel, D. Ackerman, P. Morton, E. Flynn, and M. Hybertsen. "Impedance-corrected carrier lifetime measurements in semiconductor lasers". *Applied Physics Letters*, Vol. 67, No. 11, pp. 1506–1508, 1995.

[Simp 95] T. B. Simpson, J. M. Liu, and A. Gavrielides. "Bandwidth enhancement and broadband noise reduction in injection-locked semiconductor lasers". *IEEE Photonics Technology Letters*, Vol. 7, No. 7, pp. 709–711, 1995.

[Slav 06] R. Slavík, Y. Park, M. Kulishov, R. Morandotti, and J. Azaña. "Ultrafast all-optical differentiators". *Optics Express*, Vol. 14, No. 22, pp. 10699–10707, 2006.

[Soda 79] H. Soda, K. Iga, C. Kitahara, and Y. Suematsu. "GaInAsP-InP Surface Emitting Injection-Lasers". *Japanese Journal of Applied Physics*, Vol. 18, No. 12, p. 2329, 1979.

[Soda 83] H. Soda, Y. Motegi, and K. Iga. "GaInAsP/InP surface emitting injection lasers with short cavity length". *IEEE Journal of Quantum Electronics*, Vol. 19, No. 6, pp. 1035–1041, 1983.

[Ster 89] D. Stern, W.-Z. Lin, C. A. Puliafiro, and J. G. Fujimoto. "Femtosecond Optical Ranging of Corneal Incision Depth". *Investigative Ophthalmology & Visual Science*, Vol. 30, No. 1, pp. 99–104, 1989.

[Stri 00] R. C. Strijbos, L. M. Augustin, and T. G. van de Roer. "Current crowding in oxide-confined intracavity-contacted VCSELs". In: *Proceedings Symposium IEEE/LEOS Benelux Chapter*, 2000.

[Sun 03] D. Sun, W. Fan, P. Kner, J. Boucart, T. Kageyama, R. Pathak, D. Zhang, and W. Yuen. "Sub-mA threshold 1.5 μm VCSELs with

epitaxial and dielectric DBR mirrors". *IEEE Photonics Technology Letters*, Vol. 15, No. 12, pp. 1677–1679, 2003.

[Sze 81] S. M. Sze. *Physics of Semiconductor Devices.* John Wiley & Sons, Inc., 1981.

[Taka 87] A. Takada, T. Sugie, and M. Saruwatari. "High-speed picosecond optical pulse compression from gain-switched 1.3-μm distributed feedback-laser diode (DFB-LD) through highly dispersive single-mode fiber". *Journal of Lightwave Technology*, Vol. 5, No. 10, pp. 1525–1533, 1987.

[Tamm 97] S. Tammela, H. Ludvigsen, T. Kajava, and M. Kaivola. "Time-Resolved Frequency Chirp Measurement Using a Silicon-Wafer Etalon". *IEEE Photonics Technology Letters*, Vol. 9, No. 4, pp. 475–477, 1997.

[Treb 00] R. Trebino. *Frequency-Resolved Optical Gating: The Measurement of Ultrashort Laser Pulses.* Kluwer Academic Publishers, 2000.

[Tuck 83] R. Tucker and D. Pope. "Microwave circuit models of semiconductor injection lasers". *IEEE Transactions on Microwave Theory and Techniques*, Vol. 31, No. 3, pp. 289–294, 1983.

[Vall 95] A. Valle, J. Sarma, and K. A. Shore. "Spatial hole burning effects on the dynamics of vertical cavity surface emitting lasers". *IEEE Journal of Quantum Electronics*, Vol. 31, No. 8, pp. 1423–1431, 1995.

[Vall 98] A. Valle. "Selection and modulation of high-order transverse modes in VCSELs". *IEEE Journal of Quantum Electronics*, Vol. 34, No. 10, pp. 1924–1932, 1998.

[Vasi 00] P. P. Vasil'ev, I. H. White, and J. Gowar. "Fast phenomena in semiconductor lasers". *Reports on Progress in Physics*, Vol. 63, No. 12, pp. 1997–2042, DEC 2000.

[Vill 08] A. Villafranca, J. Lasobras, R. Escorihuela, R. Alonso, and I. Garcés. "Time-Resolved Chirp Measurements Using Complex Spectrum Analysis Based on Stimulated Brillouin Scattering". In: *Optical Fiber Communication Conference and Exposition and The National Fiber Optic Engineers Conference, (Optical Society of America, 2008)*, 2008.

[Vu 08] K. T. Vu, A. Malinowski, M. A. F. Roelens, M. Ibsen, P. Petropoulos, and D. J. Richardson. "Full Characterization of Low-Power Picosecond Pulses From a Gain-Switched Diode Laser Using Electrooptic

Modulation-Based Linear FROG". *IEEE Photonics Technology Letters*, Vol. 20, No. 7, pp. 505–507, 2008.

[Walm 09] I. A. Walmsley and C. Dorrer. "Characterization of ultrashort electromagnetic pulses". *Advances in Optics and Photonics*, Vol. 1, No. 2, pp. 308–437, 2009.

[Weis 94a] S. Weisser, I. Esquivias, P. J. Tasker, J. D. Ralston, B. Romero, and J. Rosenzweig. "Impedance characteristics of quantum-well lasers". *IEEE Photonics Technology Letters*, Vol. 6, No. 12, pp. 1421–1423, 1994.

[Weis 94b] S. Weisser, I. Esquivias, P. J. Tasker, J. D. Ralston, and J. Rosenzweig. "Impedance, modulation response, and equivalent circuit of ultra-high-speed In0.35Ga0.65As/GaAs MQW lasers with p-doping". *IEEE Photonics Technology Letters*, Vol. 6, No. 7, pp. 782–785, 1994.

[Whit 85] I. H. White, D. Gallagher, and M. O. andD. Bowley. "Direct Streak-Camera Observation of Picosecond Gain-Switched Optical Pulses from a 1.5 *mu*m Semiconductor Laser". *Electronics Letters*, Vol. 21, No. 5, pp. 197–199, 1985.

[Wies 93] J. M. Wiesenfield, G. Hasnain, J. S. Perino, J. D. Wynn, R. E. Leibenguth, Y.-H. Wang, and A. Cho. "Gain-switched GaAs Vertical-cavity surface-emitting lasers". *IEEE Journal of Quantum Electronics*, Vol. 29, No. 6, pp. 1996–2005, 1993.

[Yang 09] C. Yang. *1.55 mum AlGaInAs strained MQW laser diodes.* PhD thesis, Dept. of Electrical and Computer Engineering, University of New Mexico, 2009.

[Yu 03] S. F. Yu. *Analysis and Design of Vertical Cavity Surface Emitting Lasers.* Wiley-Interscience;, 2003.

[Yue 04] A. Yue, K. Shen, R. Wang, and J. Shi. "Low threshold current 1.3 μm GaInNAs VCSELs grown by MOVPE". *IEEE Photonics Technology Letters*, Vol. 16; 16, No. 3, pp. 717–719, 2004.

[Ywas 82] K. Ywashita and K. Nakagawa. "Suppression of mode partition noise by laser diode light injection". *IEEE Transactions on Microwave Theory and Techniques*, Vol. 30, No. 10, pp. 1657–1662, 1982.

[Zhao 07] X. Zhao, D. Parekh, E. K. Lau, H. K. Sung, M. C. Wu, W. Hofmann, M. C. Amman, and C. J. Chang-Hasnain. "Novel cascaded injection-locked 1.55 μm VCSELs with 66 GHz modulation bandwidth". *Optics Express*, Vol. 15, No. 22, p. 14810, 2007.

[Zhu 10] N. H. Zhu, G. Z. Xu, W. Hofmann, W. Chen, G. Böhm, Y. Liu, X. Wang, L. Xie, and M. C. Amann. "Small-Signal Equivalent-Circuit Model and Characterization of 1.55-*mu*m Buried Tunnel Junction Vertical-Cavity Surface-Emitting Lasers". *IEEE Transactions on Microwave Theory and Techniques*, Vol. 58, No. 5, pp. 1283–1289, 2010.